INTERNATIONAL ATOMIC ENERGY AGENCY
UNITED NATIONS EDUCATIONAL, SCIENTIFIC AND CULTURAL ORGANIZATION
INTERNATIONAL CENTRE FOR THEORETICAL PHYSICS
I.C.T.P., P.O. BOX 586, 34100 TRIESTE, ITALY, CABLE CENTRATOM TRIESTE

UNITED NATIONS INDUSTRIAL DEVELOPMENT ORGANIZATION

INTERNATIONAL CENTRE FOR SCIENCE AND HIGH TECHNOLOGY

SMR.550 - 4

SPRING COLLEGE IN MATERIALS SCIENCE ON

"NUCLEATION, GROWTH AND SEGREGATION IN MATERIALS SCIENCE AND ENGINEERING"

(6 May - 7 June 1991)

BACKGROUND MATERIAL

for lectures on

"SOLIDIFICATION"

H. MÜLLER-KRUMBHAAR
Institut für Festkörperforschung
Institut 3 - Theorie III
Forschungszentrum Jülich GmbH
Postfach 1914
D-5170 Jülich
Germany

---

from "Phase transformations in Materials",
P. Haasen, ed. VCH-Verlag, Weinheim 1991, Germany

10 Solidification

Heiner Müller-Krumbhaar

Institut für Festkörperforschung der KFA, Jülich, Federal Republic of Germany

Wilfried Kurz

Département des Matériaux, EPFL, Lausanne, Switzerland

List of Symbols and Abbreviations 554
10.1 **Introduction** 557
10.2 **Basic Concepts in First-Order Phase Transitions** 559
10.2.1 Nucleation 559
10.2.2 Interface Propagation 561
10.2.3 Growth of Simple Crystal Forms 563
10.2.4 Mullins-Sekerka Instability 565
10.3 **Basic Experimental Techniques** 567
10.3.1 Free Growth 568
10.3.2 Directional Growth 570
10.4 **Free Dendritic Growth** 572
10.4.1 The Needle Crystal Solution 573
10.4.2 Side-Branching Dendrites 577
10.4.3 Experimental Results on Free Dendritic Growth 583
10.5 **Directional Solidification** 588
10.5.1 Thermodynamics of Two-Component Systems 588
10.5.2 Scaled Model Equations 592
10.5.3 Cellular Growth 594
10.5.4 Directional Dendritic Growth 598
10.5.5 The Selection Problem of Primary Cell-Spacing 602
10.5.6 Experimental Results on Directional Dendritic Growth 606
10.5.7 Extensions 616
10.6 **Eutectic Growth** 618
10.6.1 Basic Concepts 618
10.6.2 Experimental Results on Eutectic Growth 622
10.7 **Summary and Outlook** 628
10.8 **References** 629

List of Symbols and Abbreviations

a	distance
A	area
A	amplitude
$\hat{A}$	differential operator
a_1, a_K	constants
b	arbitrary parameter
$\hat{B}$	selfadjoint differential operator
ΔC	miscibility gap
C, C'	constants
C_E	eutectic concentration
C_L, C_S, C_x, etc.	concentration
c_p	specific heat at constant pressure
d	atomistic length, capillary length
D	diffusion constant
d_0	capillary length
D_i	transport coefficients, diffusion constants
D_T	thermal diffusion coefficient
$E_1(P)$	exponential integral
erfc	error function complement
F	Helmholtz free energy
f	scaling function
g	Gibbs free energy density
ΔG	change in Gibbs free energy
$\hat{G}$	free energy per surface element
$G(\{\xi_i\})$	free energy
G_T	constant temperature gradient
J	probability current
K	curvature
k	segregation coefficient, wave number
k_B	Boltzmann constant
L	natural scale
l	external length, diffusion length
l	thickness of layer, diffusion length
L_m	latent heat of melting
m_α, m_β	liquidus or solidus slope
N_i	particle number of species i
P	pressure, Peclet number
$\mathcal{P}$	principal value
$P(\{\xi_i\})$	probability of configuration
q	wave number, inverse length
Q_{min}	minimal work
r	radius of nucleus, radial distance
$R(S)$	local radius of curvature at point S

R_0	radius of curvature
r_c	critical radius
S	position on the interface, entropy
ΔS	change in entropy
T	temperature
t	time
Δt	change in time
T_0	reference temperature
T_E	eutectic temperature
T_I	interface temperature
T_m	melting temperature
u	dimensionless temperature field or concentration field
U	energy
V	speed
V_a	maximal speed, absolute stability
V_c	critical velocity
v_R	growth rate
w	probability of fluctuation
X_i, X_j	extensive variables
Y_i, Y_j	intensive variables
Z	partition function
z	space coordinate
β	interface kinetics
β_4	4-fold anisotropy of the kinetic coefficient
γ	surface tension or surface free energy
Γ	ratio of S–L interface energy to specific melting entropy
Γ_2	Green's function integral
Δ	supercooling (negative temperature field u at infinity)
δ	local concentration gap, surface tension anisotropy
ε	relative strength of anisotropy of capillary length
$\zeta(x, t)$	deviation of the interface
η	coordinate
ϑ	angle of orientation relative to the crystallographic axes
Θ	function of (x, t)
$\varkappa(s)$	mobility
λ	interface spacing, wavelength
$\Lambda(\sigma, \varepsilon)$	solvability function
λ_2	wavelength of side branch
λ_f	wavelength of the fastest mode
λ_s	stability length
μ	chemical potential
ν_0	effective kinetic prefactor
ξ	variable
ξ_i	position vectors

$\Delta\zeta$	small normal displacement
ϱ	Ivantsov radius
σ	scaling-function
τ	variable
Ω	atomic volume, atomic area
DLA	diffusion limited aggregation
DS	directional solidification
f	faceted
l.h.s.	left-hand-side
nf	non faceted
PVA	pivalic acid
r.h.s.	right-hand-side
SCN	succinonitrate
WKB	WKB-technique for singular perturbations

10.1 Introduction

This chapter on solidification discusses the basic mechanisms of the liquid-solid phase transformation. In particular, we address the phenomena of cellular and dendritic patterns formed by the interface between liquid and solid, as the interface, or solidification front, advances into the liquid during the solidification process.

The atomistic processes of the liquid-solid transformation are stil not well understood. Therefore, we will remain on a phenomenological level of description. The processes on very large scales, such as casting or welding, depend significantly on the experimental equipment and are discussed elsewhere in this series (see, for example, Volume 15, Chapters 1 to 3).

We will restrict our attention accordingly to phenomena occurring on some important intermediate length scales. It turns out that there is a natural scale L of the order of microns (or up to millimeters) which gives a measure for the microcrystalline structures formed during the solidification process. In its simplest form this natural length is the geometric mean $L \sim \sqrt{d\,l}$ of a microscopic intrinsic length d defined by typical material properties and an external length l defined by the macroscopic arrangement of the experimental equipment. The intrinsic correlation lengths in liquids and solids near the freezing point are rather short, of the order of atomic size, or several Ångströms, because solidification is a phase transition of first order. The experimental equipment in contrast gives external length scales in the range of centimeters to meters such that one consequently arrives at the mentioned scale of microns.

Assuming for the moment that only two lengths are important, why should one expect L to be given by the geometric mean rather than, for example, the arithmetic mean? An intuitive argument goes as follows: The patterns formed at the solid-liquid interface and in both adjacent phases during the solidification process result from the competition of two "forces", one being stabilizing for homogeneous structures, the other being destabilizing. The stabilizing force here clearly must be associated with the intrinsic atomistic length d, since we have argued that it is related to the length of correlation or coherence inside the material or at the interface. In contrast, we must associate the external length l with a destabilizing force. Again this is a quite natural assumption, as the phase transformation or destabilization of the nutrient phase is induced by the experimental environment.

It is now obvious that the result of such a competition of "forces" should be expressed by the *product* $d\,l$ of the two representative quantities rather than by the sum, since the latter would change the relative importance of the two lengths when their values become very different.

Admittedly, these arguments look a little overstressed considering the many parameters controlling the details of a solidification process. Note, however, that nothing has been said so far about the precise relation of d, l, and L to any specific process nor have we defined the proportionality factor. In principle, d and l could also enter with different exponents but fortunately things are usually not that complicated right from the start.

Being still courageous enough to make one more step on this slightly unsafe ground, we may finally assume that the external length scale l is related (destabilizing force!) to the speed V of the solidification, which gives a length when combined with a diffusion constant D for heat or matter as $l \sim D/V$. From this we immedi-

ately obtain a relation between the speed of phase change V and the length scale L of the resulting pattern:

$$V L^2 \approx \text{constant} \qquad (10\text{-}1)$$

Surprisingly enough, we have arrived at about the most celebrated equation for processes of dendritic, directional, and eutectic solidification without even defining any of these processes! Two remarks, therefore, may be in order here. First, detailed studies of the different solidification schemes in recent years have attempted to extract the common and universal aspects of these processes. Such common features indicate a common basis of rather general nature, as outlined above. Second, we have of course ignored most of the specific aspects of each individual process. In directional solidification, for example, a band of possible wavelengths for stationary patterns are found and up to now it is not yet clear if and how a specific wavelength from that band is finally selected. The assumption of just two independent length scales in many cases is also a rather gross simplification of the actual situation. We will therefore leave this line of general arguments and look at some concrete models which are believed to capture at least some essentials for the fascinating patterns produced during solidification.

Some remarkable progress has been achieved in the theoretical treatment of these phenomena during the last ten years. In the list of references, we have concentrated our attention on recent developments since there are some good reviews on older work (for example, Langer, 1980a; Kurz and Fisher, 1984, 1989).

An experimentalist may finally wonder why we have expressed most of the equations in a nondimensionally scaled form rather than writing all material parameters down explicitly at each step. One reason is that the equations then appear much simpler than if one attempted to carry along all prefactors. The second and more important reason is that the scaled form allows for a much simpler comparison of experiments for different sets of parameters which usually appear only in some combinations in the equations, thereby leading to cancellations and compensations.

In Section 10.2, a quick summary of the ingredients for a theory is given, starting at nucleation, then deriving boundary conditions for a propagating interface between two phases, and finally discussing some general aspects of the diffusion equation with a propagating boundary. This is followed by an introduction to basic experimental techniques in Section 10.3. In Section 10.4, the case of a simple solid growing in a supercooled melt is discussed in some detail, leading to the present understanding of dendritic growth. In Section 10.5 the technically important process of directional solidification is presented. The evolution of cellular patterns above a critical growth rate can in principle be understood without the knowledge of dendritic growth. Actually, the parameter range for simple sinusoidal cells is very narrow so that one usually operates in the range of deep cells or even dendrites, which suggests our sequence of presentation. Finally, these concepts are extended in Section 10.6 to alloys with a eutectic phase diagram and the resulting complex phenomena. As this field currently is in rapid theoretical development, our discussion here necessarily is somewhat preliminary. The chapter is closed by a summary with complementary remarks.

10.2 Basic Concepts in First-Order Phase Transitions

The different possible phases of a material existing in thermodynamic equilibrium must be discriminated by some quantity in order to formulate a theory. Such quantities are called "order parameters" and should correspond to extensive thermodynamic variables. The difference between a solid and a liquid is defined by the shear modulus, which changes discontinuously at the phase transition. This definition describes the difference in long-range orientational correlations between two distant pairs of neighboring atoms. Normally, one uses instead the more restrictive concept of translational order as expressed through two-point correlation functions, or Bragg peaks, in scattering experiments.

Although these different order-parameter concepts pose a number of subtle questions, particularly in two dimensions where fluctuations are very important, we will simply assume in this chapter that there is some quantity which discriminates between a solid and a liquid in a unique way. Such an order parameter may be the density, for example, which usually changes during melting, or the composition in a two-component system. We would like to stress, however, that these are just auxiliary quantities which change as a consequence of the solid-liquid transition but which are not the fundamental order parameters in the sense of symmetry arguments. For a more general discussion see Chapter 3 (Binder) and literature on order disorder transitions (Brazovsky, 1975; Nelson, 1983).

First-order transitions are characterized by a discontinuous change of the order parameter. All intrinsic length scales are short, typically of the size of a few atomic diameters. We may therefore assume local thermal equilibria with locally well defined thermodynamic quantities like temperature, etc., and smooth variations in these quantities over large distances. Interfaces in such systems will represent singularities or discontinuities in some of the quantities, such as the order parameter or the associated chemical potential, but they will still leave the temperature as a continuous function of the position in space.

10.2.1 Nucleation

A particular consequence of the well-defined local equilibrium is the existence of well-defined metastable states, corresponding to a local, but not global, minimum of the free energy. But so far we have neglected thermal fluctuations. The probability for a fluctuation (or deviation from the average state) of a large closed system is

$$w \sim \exp(\Delta S) \qquad (10\text{-}2)$$

where ΔS is the change in entropy of the system due to the fluctuation (see, e.g., Landau and Lifshitz, 1970). Defining $Q_{\min}$ as the minimal work necessary to create this change of thermodynamic quantities, we obtain

$$\Delta S = Q_{\min}/T_0 \qquad (10\text{-}3)$$

with T_0 being the average temperature of the system. Note that this holds even for large fluctuations, as long as the change of extensive quantities in the fluctuation region is small compared to the respective quantities in the total system.

Considering this system as a metastable liquid within which a fluctuation has formed a small solid region, and assuming, furthermore, that the liquid is only slightly metastable, one arrives at the well-known result (Landau and Lifshitz, 1970) in 3 dimensions for a one component system:

$$Q_{\min} = -\frac{4\pi r^3}{3\Omega}\left[\mu_L(P) - \mu_S(P)\right] + 4\pi r^2 \cdot \gamma \qquad (10\text{-}4)$$

which together with Eqs. (10.2) and (10-3) gives the probability for the reversible formation of a spherical solid nucleus of radius r within a slightly supercooled liquid. Here Ω is the atomic volume, P the pressure, $\mu_L > \mu_S$ the chemical potentials of liquid and solid in a homogeneous system, and γ the (here isotropic) surface tension, or surface free energy.

A few remarks should be made here. When deriving Eq. (10-4), one uses the concept of small deviations from equilibrium, while Eqs. (10-2) and (10-3) are more generally valid (Landau and Lifshitz, 1970). In the estimation of the range of validity of Eq. (10-4), it turns out, however, that it should be applicable to even very large supercoolings for most liquids, since the thermal transport is either independent of, or faster than, the kinetics of nucleus formation (Ohno et al., 1990). The range of validity of Eq. (10-4) is then typically limited by the approach to the "spinodal" region, where metastable states become unstable, even when fluctuations are ignored (see Binder, Chapter 7).

Assuming, therefore, that we are still in the range of well-defined metastable states, we may write Eqs. (10-2) and (10-3) as

$$w = \nu_0 \exp(-\Delta G/T_0) \tag{10-5}$$

identifying the change in Gibbs free energy ΔG by Eq. (10-4), with an undetermined prefactor ν_0. Here we do not discriminate between surface tension and surface free energy, despite the fact that the first is a tensorial quantity, and the latter only scalar (although it may be anisotropic, which is ignored here). A difference between surface tension and surface free energy arises when the system does not equilibrate between surface and bulk so that, for example, the number of atoms in the surface layer is conserved. Throughout this chapter, we will assume perfect local equilibration in this respect, and we may then ignore the difference.

The extremal value of Eqs. (10-4) and (10-5) with respect to the variation of r gives the critical radius

$$r_c = \frac{2\gamma}{\Delta\mu}\,\Omega \quad \text{(3-dim)} \tag{10-6a}$$

$$= \frac{\gamma}{\Delta\mu}\,\Omega \quad \text{(2-dim)} \tag{10-6b}$$

so that for $r < r_c$, the nucleus tends to shrink, while for $r > r_c$ it tends to grow and at $r = r_c$ it is in an unstable equilibrium.

The same thermal fluctuations causing such a nucleus to appear also produce deviations from the average spherical shape. This leads to power-law corrections in the prefactor of Eq. (10-5) or logarithmic corrections in the exponent (Voronkov, 1983; Langer, 1971).

So far these considerations have dealt with static aspects only. Since the fluctuations vary locally with time, Eq. (10-5) may be interpreted as the rate at which such fluctuation occurs, and, consequently, with $r = r_c$ one obtains the rate for the formation of a critical nucleus which, after appearance, is assumed to grow until the new phase fills the whole system. This is the classical nucleation theory. A very elegant formulation was given by analytic continuation into the complex plane (Langer, 1971). Further additions include the definition of the prefactor in Eq. (10-5) and a more detailed analysis of the kinetics near $r = r_c$ (Zettlemoyer, 1969, 1976).

Considering the many uncertainties entering from additional sources such as the range of atomic potentials and the change of atomic interaction in the surface, we will ignore all these effects by absorbing them into the effective kinetic prefactor ν_0 in Eq. (10-5), to be determined experimentally.

10.2.2 Interface Propagation

An interface between two regions in space of different order parameters (solid vs. liquid) will be treated in this chapter as a *jump discontinuity* and as an object of infinitesimal thickness. In this section we derive a local equation of motion for the interface, which will serve as a boundary condition in the remaining part of the chapter.

For simplicity, consider a one-dimensional interface in a two-dimensional system. Ignoring the atomic structure, assume that the interface is a smooth continuous line. Marking points at equal distances a on this line, we may then define velocities of the points in normal direction as

$$V_i = \frac{\Delta\xi_i}{\Delta t} \tag{10-7}$$

where $\Delta\xi_i$ is the small normal displacement of point i. If we assume these points to be kept at fixed positions ξ_i for the moment, a (restricted) free energy $G(\{\xi_i\})$ may be assigned to this restricted interface. The probability for this configuration is

$$P(\{\xi_i\}) = Z^{-1} \exp(-G/T) \tag{10-8}$$

with temperature T in units of k_B and Z the partition function. Since the total probability is conserved, we obtain the continuity equation

$$\frac{\partial P}{\partial t} + \mathrm{div}_{(i)}(J) = 0 \tag{10-9}$$

with $J = \{J_i\}$ as the probability current in i-space

$$J_i = V_i P - D_i \frac{\partial P}{\partial \xi_i} \tag{10-10}$$

and the divergence taken in the same abstract space. The first term in Eq. (10-10) is a drift, the second term, the constitutive relation with transport coefficients D_i and the derivative is taken normal to the interface. We now assume local equilibrium to exist on length scales a (i.e., $i \to i \pm 1$) such that the probability current is zero

$$V_i P = D_i \frac{\partial P}{\partial \xi_i} \tag{10-11}$$

and with Eqs. (10-7) and (10-8), we immediately arrive at

$$\frac{\partial \xi_i}{\partial t} = -\frac{D_i}{T} \frac{\partial G(\{\xi_i\})}{\partial \xi_i} \tag{10-12}$$

Taking the continuum limit $a \to 0$, one obtains the final form

$$\frac{\partial \xi(S)}{\partial t} = -\varkappa(S) \frac{\delta \tilde{G}}{\delta \xi(S)} \tag{10-13}$$

This is the time-dependent Ginzburg-Landau equation (Burkhardt et al., 1977). Here S denotes a position on the interface, $\partial\xi(S)$ is the normal displacement, $\delta/\delta\xi(S)$ the variational derivative, and $\varkappa(S)$ the "mobility", which may depend on position and orientation. $\tilde{G}$ is the free energy per surface element.

We will now make some explicit assumptions about G in order to arrive at an explicit equation of motion. Let $\hat{n}_S$ be the normal direction on the interface, $\gamma(\hat{n}_S)$ the interface free energy, ϑ the angle of orientation relative to the crystallographic axes, $R(S)$ the local radius of curvature at point S on the interface, and $A_{L,S}$ the areas covered by liquid or solid. The Gibbs free energy of the total solid-liquid system with interface is

$$G_{\mathrm{tot}} = \int_S \mathrm{d}S\,\gamma + \int_{\mathrm{Liquid}} \mathrm{d}A_L\, g_L(x) + \int_{\mathrm{Solid}} \mathrm{d}A_S\, g_S(x) \tag{10-14}$$

from which the variational derivative in Eq. (10-13) is formally obtained by

$$\delta G_{\mathrm{tot}} = \int_S \mathrm{d}S \left[\frac{\delta \tilde{G}}{\delta \xi}\right] \delta\xi(S) \tag{10-15}$$

where $\delta\xi(S)$ is a small arbitrary displacement of the interface in normal direction. Explicitly this is written as

$$\delta G_{tot} = \int_S \{\gamma\, \delta(\mathrm{d}S) + \mathrm{d}S\, \delta\gamma\} - \int_S \mathrm{d}S\, \delta\xi(S)\,[g_L(S) - g_S(S)] \tag{10-16}$$

with free energy densities g given here per atomic "volume" (or area) Ω. As usual, one has to extract terms $\delta\xi$ out of the terms $\delta(\mathrm{d}S)$ and $\delta\gamma$. Assuming γ to depend only on local orientation,

$$\delta\gamma(\vartheta) = \frac{\mathrm{d}\gamma}{\mathrm{d}\vartheta}\,\delta\vartheta \tag{10-17}$$

and with

$$\delta\vartheta = \frac{\mathrm{d}}{\mathrm{d}S}\,\delta\xi; \quad \frac{\mathrm{d}\vartheta}{\mathrm{d}S} = \frac{\mathrm{d}\vartheta}{\mathrm{d}S}\,\frac{\mathrm{d}}{\mathrm{d}\vartheta}; \quad \frac{\mathrm{d}}{\mathrm{d}S}\,\vartheta = -\frac{1}{R} \tag{10-18}$$

one obtains

$$\delta\gamma(\vartheta) = -\frac{\mathrm{d}\gamma}{\mathrm{d}\vartheta}\,\frac{1}{R}\,\frac{\mathrm{d}}{\mathrm{d}\vartheta}\,\delta\xi \tag{10-19}$$

The other term simply gives

$$\delta(\mathrm{d}S) = \frac{1}{R}\,\mathrm{d}S\,\delta\xi \tag{10-20}$$

Incorporating Eqs. (10-19) and (10-20) into Eq. (10-16) and integrating Eq. (10-19) by parts, one obtains through comparison with Eq. (10-15)

$$\frac{\partial\xi}{\partial t} \equiv V_\perp = \varkappa(\vartheta)\left\{\Delta g(S) - \frac{1}{R}\left(\gamma + \frac{\mathrm{d}^2\gamma}{\mathrm{d}\vartheta^2}\right)\right\} \tag{10-21}$$

as an explicit local equation for the advancement of an interface in 2 dimensions with normal velocity $V_\perp$, anisotropic kinetic coefficient $\varkappa(\vartheta)$, surface free energy $\gamma(\vartheta)$, and jump $\Delta g = g_L - g_S$ of free energy density at position S along the interface (Burkhardt et al., 1977). The Gibbs free energy density g hereby corresponds to an infinite solid or liquid without influences from curvature terms. For a single-component system, $\mu = g\Omega$, where μ is the chemical potential of the respective phase. The generalization to 3 dimensions adds another curvature term into Eq. (10-21), which then corresponds to two curvatures and angles in the two principal directions (For isotropic γ, the curvature $1/R$ is simply changed into $2/R$).

Two useful observations can be made already at this stage. There is a solution with $V_\perp = 0$ if the term $\{\ldots\}$ in Eq. (10-21) is zero. For finite radius of curvature R, this corresponds precisely to the critical nucleus, Eq. (10-6b), but now with anisotropic $\gamma(\vartheta)$. This equation therefore determines the shape of the critical nucleus in agreement with the *Wulff construction* (Wulff, 1901). Second, for very large mobility $\varkappa(\vartheta)$ the deviation from equilibrium $\{\ldots\}$ may be very small in order to produce a desired normal velocity $V_\perp$. We will use this simplification of equilibrium at the interface

$$\Delta g \cong \frac{1}{R}\,(\gamma + \gamma''), \quad \text{2-dim.} \tag{10-22}$$

wherever possible, but we shall comment on the changes due to finite $\varkappa(\vartheta)$. The double-prime means derivatives as in Eq. (10-21). In many cases this seems to be justified by experimental conditions. On the other hand, very little is known quantitatively about $\varkappa(\vartheta)$. A last point to be mentioned here is our assumption that the interfaces are not facetted at equilibrium. If they are facetted, as crystals typically are at low temperatures in equilibrium with their vapor, the situation is considerably more complicated and not yet completely understood (Kashuba and Pokrovsky, 1990).

It is now generally believed that facetted surfaces undergo a kinetic roughening transition even at small driving forces, so that a rough surface is present under growth conditions. The concept outlined above

then generally applies in an effective fashion. Actually, facets may persist over experimentally relevant length scales, which are not covered by this analysis in the kinetic region. A summary of recent theoretical developments can be found in the article by Krug and Spohn (1990).

To complete this section on the basic theoretical ingredients, we will now discuss the influence of diffusive transport of heat or matter on the propagation of a solid-liquid interface (see also Langer, 1980a).

10.2.3 Growth of Simple Crystal Forms

a) *Flat interface*

The simplest model for a solidifying system consists of two halfspaces filled with the liquid and solid of a one-component material of invariant density and separated by a flat interface. The interface is approximately in equilibrium Eq. (10-22) at melting temperature T_m but advancing at a speed V in the positive z-direction into the liquid. During this freezing process, latent heat L_m has to be transported into the supercooled liquid, the solid remaining at T_m.

The equation of motion is then the thermal diffusion equation

$$\frac{\partial}{\partial t}\,T(x,t) = D_T\,\nabla^2\,T(x,t) \tag{10-23}$$

with thermal diffusion coefficient D_T and appropriate boundary conditions. At infinity in the supercooled liquid the temperature $T_\infty < T_m$ is prescribed, and T_m is the temperature at the interface. It is now very convenient to replace the temperature field T by a dimensionless u through the transformation

$$u(x,t) = \frac{T(x,t) - T_m}{(L_m/c_p)} \tag{10-24}$$

where c_p is the specific heat of the liquid at constant pressure. If, instead of temperature or heat, a second chemical component is diffusing, a similar transformation to the same dimensionless equations can be made. This is described in Section 10.5.2. We would like to stress the importance of such a scaled representation as it allows one to compare at a glance experimental situations with different sets of parameters.

In this dimensionless form, the equation of motion is

$$\frac{\partial}{\partial t}\,u = D_T\,\nabla^2\,u \tag{10-25}$$

and the boundary conditions are

$$u = u_\infty < 0 \quad \text{for } z \to \infty \tag{10-26a}$$

$$u = 0 \quad \text{at interface} \tag{10-26b}$$

So far we have not specified how the interface motion is coupled to the equation of motion. Obviously, the latent heat L_m generated during this freezing process at a rate proportional to V has to be carried away through the diffusion field. This requires a continuity equation at the interface

$$V = -D_T\,\hat{n}\cdot\nabla u \tag{10-27}$$

and since in the model here only the z-axis is important

$$V = -D_T\,\frac{\partial}{\partial z}\,u(z,t) \quad \text{at interface} \tag{10-28}$$

The growth rate is therefore proportional to the gradient of the diffusion field at the interface in the liquid. As the interface is moving, we conveniently make a coordinate transformation from $\{z,t\}$ for $\{z',t'\}$ into a frame of reference moving along with the interface at $z' = 0$:

$$z' = z - \int_0^t V(\tau)\,\mathrm{d}\tau, \qquad t' = t \tag{10-29}$$

Performing that transformation, we obtain the following for the diffusion equation

(after having again dropped the primes for convenience):

$$\frac{1}{D_T}\frac{\partial u}{\partial t} = \nabla^2 u + \frac{2}{l}\frac{\partial u}{\partial z} \qquad (10\text{-}30)$$

which defines a diffusion length

$$l \equiv 2D_T/V \qquad (10\text{-}31)$$

The interface is now always at $z = 0$ which makes the boundary condition Eq. (10-26b) and the continuity Eq. (10-28) definite.

We can obtain a stationary solution by combining Eq. (10-30) with Eqs. (10-26) and (10-28) when $\partial u/\partial t = 0$:

$$u = \exp\left(-\frac{2z}{l}\right) - 1; \quad z \geqq 0 \qquad (10\text{-}32)$$

This equation is consistent with the assumption that $u = 0$ ($T = T_m$) everywhere in the solid.

This equation describes the diffusion field ahead of the interface. It varies exponentially from its value at the interface toward the value far inside the liquid, so that the diffusion field has a typical "thickness" of l.

Note that we have not used Eq. (10-26a) as a boundary condition at infinity, but find from Eq. (10-32) that $u = -1$ implies the socalled "unit supercooling", which corresponds to

$$T(z = \infty) = T_m - (L_m/c_p) \qquad (10\text{-}33)$$

This basically says that the difference in melting enthalpy L_m between liquid and solid must be compensated by a temperature difference in order to globally conserve the energy of the system during this stationary process. In other words, if Eq. (10-33) is not fulfilled by Eq. (10-26a), the process cannot run with a stationary profile of the thermal field, Eq. (10-32). On the other hand, a particular value of the growth rate V (or l) is not specified, but seems to be arbitrary. This degeneracy is practically eliminated by other effects such as interface kinetics (Collins and Levine, 1985) or the density difference between solid and liquid (Caroli et al., 1984), so that in practice a well-defined velocity will be selected.

b) *Growth of a sphere*

The influence of the surface tension γ when it is incorporated through Eq. (10-21) is most easily understood by looking at a spherical crystal. This will not lead to stationary growth. In order to make the analysis simple, we will invoke the socalled "quasistationary approximation", by setting the left hand side in Eq. (10-25) equal to zero. The physical meaning is that the diffusion field adjusts itself quickly to a change in the boundary structure which, however, is still evolving in time because the continuity equation is velocity dependent. Of course, this approximation reproduces the stationary solutions precisely (if they exist), and in addition, it exactly identifies the instability of a stationary solution as long as it is not of the Hopf type (i.e., the critical eigenvalue is not complex). It is generally assumed that the approximation is good as long as the diffusion length is large compared with other lengths of the evolving pattern.

In a spherical coordinate system, the equation of motion then becomes

$$\frac{1}{D_T}\frac{\partial u}{\partial t} = 0 = \left\{\frac{\partial^2}{\partial r^2} + \frac{2}{r}\frac{\partial}{\partial r}\right\} u \qquad (10\text{-}34)$$

as a simple Laplace equation.

The interface is at radius $R_0(t)$ and is advancing with time. The continuity equation requires

$$v_R \equiv \frac{dR_0}{dt} = -D_T \left.\frac{\partial u}{\partial r}\right|_{r=R_0(t)} \qquad (10\text{-}35)$$

Concerning the boundary condition, we note that for a simple substance the difference in slopes of the chemical potentials for solid and liquid at the melting point (Landau and Lifshitz, 1970) is L_m/T_m, giving

$$\Delta\mu = -L_m(T - T_m)/T_m \qquad (10\text{-}36)$$

With Eqs. (10-21) and (10-24), the boundary condition in the case of isotropic γ becomes

$$u(\text{interface}) = -d_0 K - \beta V \qquad (10\text{-}37)$$

with curvature

$$K = \begin{cases} 2/R, & \text{3-dim} \\ 1/R, & \text{2-dim} \end{cases} \qquad (10\text{-}38)$$

capillary length

$$d_0 = \gamma T_m c_p / L_m^2 \qquad (10\text{-}39)$$

and interface kinetics

$$\beta = \alpha^{-1} T_m c_p / L_m^2 \qquad (10\text{-}40)$$

The generalization to nonisotropic γ follows from Eq. (10-21) and comments.

Note that in Eq. (10-37) both curvature and nonequilibrium occur at the boundary as opposed to the simple case in Eq. (10-26b), shown above. At infinity we finally impose

$$u_\infty = u(r, t) = -\Delta \qquad (10\text{-}41)$$

as the now arbitrary dimensionless supercooling. This equation together with Eq. (10-24) is the definition for Δ.

The solution to Eq. (10-34) with Eqs. (10-35), (10-37), and (10-41) in the liquid is then simply

$$u(r) = -\Delta + \frac{R_0}{r}\left(1 - \frac{2d_0}{R_0}\right)\Big/\left(1 + \frac{\beta D_T}{R_0}\right) \qquad (10\text{-}42)$$

where we used $K = 2/r$ as the curvature of the spherical surface in three dimensions.

The growth rate, accordingly, is

$$v_R = \frac{dR_0}{dt} = \frac{D_T}{R_0}\left(1 - \frac{2d_0}{R_0}\right)\Big/\left(1 + \frac{\beta D_T}{R_0}\right) \qquad (10\text{-}43)$$

and it is found that for large radii $R_0(t)$ the growth rate is proportional to the supercooling Δ:

$$V_R \approx \frac{D_T}{R_0}\Delta\left(1 - \beta\frac{D_T}{R_0} + \ldots\right) \qquad (10\text{-}44)$$

It can also be seen that the kinetic coefficient β becomes less important in the limit of large radii and correspondingly small growth rates. This in many cases justifies our previous equilibrium approximation, Eq. (10-22).

We have not discussed here the solidification of a binary mixture. As the details of the phase diagram will become important later, we will postpone this topic to the section on directional solidification. We would like to mention, however, that the representation of the diffusion field in dimensionless form, found in Eq. (10-24), has the virtue that several results can be carried over directly from the thermal case to compositional diffusion, although there are some subtleties in the boundary conditions which make the latter more difficult to analyze.

10.2.4 Mullins-Sekerka Instability

We now combine the considerations of the previous Sections 10.2.3 a) and b) to study the question of whether an originally flat interface will remain flat during the growth process. The results indicate that a flat interface moving into a supercooled melt will become rippled (Mullins and Sekerka, 1963, 1964).

The basic equations are almost exactly the same as in the previous section a) Eqs. (10-30), (10-27), (10-26a), but instead of the boundary condition Eq. (10-26b), we now have to consider deviations from a flat interface as we move parallel to the interface in the x-direction. This is provided by Eq. (10-37) as the boundary condition, where we set $\beta = 0$ for simplicity.

Denoting the deviation of the interface from $z = 0$ as $\zeta(x,t)$, we designate the curvature for small amplitudes simply as $K = -\partial^2\zeta/\partial x^2$, where, in agreement with Eq. (10-38), the sign of K allows for the curvature to be positive for a solid protrusion into liquid. We follow here the notation of Langer (1980a).

In a quasistationary approximation, for the sake of simplicity we set the l.h.s. in Eq. (10-30) equal to zero, which of course allows for the stationary solution, Eq. (10-32). It is not difficult to treat the fully time-dependent problem here, but the modifications do not change the results substantially. We shall now perturb that solution by making a small sinusoidal perturbation of the flat interface:

$$\zeta(x,t) = \hat{\zeta}_k \cdot \exp(ikx + \Omega_k t) \qquad (10\text{-}45)$$

Similarly, a perturbation of the diffusion field is made in the liquid and in the solid

$$u(x,z,t) = \exp\left(-\frac{2z}{l}\right) - 1 + \hat{u}_k \exp(ikx - qz + \Omega_k t); \qquad (10\text{-}46)$$

$$u'(x,z,t) = \hat{u}'_k \exp(ikx + q'z + \Omega_k t)$$

where the unprimed form is for the liquid, and the primed values are for the solid. Inserting Eq. (10-46) into Eq. (10-30) with $\partial u/\partial t = 0$, we obtain

$$\begin{aligned} -2q/l + q^2 - k^2 &= 0 \\ 2q'/l' + q'^2 - k^2 &= 0 \end{aligned} \qquad (10\text{-}47)$$

Replacing z in Eq. (10-46) by $\zeta(x,t)$ from Eq. (10-45), we can insert this into the boundary condition Eq. (10-37) for $\beta = 0$ to obtain

$$\hat{u}'_k = -2\hat{\zeta}_k/l + \hat{u}_k = -d_0 k^2 \hat{\zeta}_k \qquad (10\text{-}48)$$

where we have linearized the $\exp(\ldots)$ with respect to ζ. Instead of the velocity in Eq. (10-27), we must now use $V_\zeta = 2D/l + \partial\zeta/\partial t$. With this equation and the same linearization as before

$$\Omega_k \hat{\zeta}_k = -D(2/l)^2 \hat{\zeta}_k + D\,q\,\hat{u}_k + D'\,q'\,\hat{u}'_k \qquad (10\text{-}49)$$

is obtained for the conservation law, Eq. (10-27), (and for small values of ζ, practically Eq. (10-28)). Eliminating $\hat{u}_k$ here using Eq. (10-48) and eliminating q using Eq. (10-47) in the limit $kl \gg 1$ or $k \approx q \approx q'$, we obtain

$$\begin{aligned} \Omega_k &= V \cdot (q - 2/l) - (D\,q + D'\,q')\,d_0 k^2 \\ &\approx kV[1 - \tfrac{1}{2}(1 + D'/D)\,l\,d_0 k^2] \end{aligned} \qquad (10\text{-}50)$$

This formula describes the basic mechanism of diffusion-controlled pattern formation in crystal growth. Although, in general, diffusion tends to favor homogeneous structures, in the present case it works in the opposite direction! This is easy to understand; the foremost points of a sinusoidal deformation of the interface can dissipate the latent heat of freezing by a larger space angle into the liquid than the points inside the bays. The latter points will therefore be slowed down. The tip points will be accelerated in comparison with the average rate of advancement.

The formula therefore consists of a destabilizing part leading to positive Ω_k and a stabilizing part controlled by the capillarity d_0. The stabilization is most efficient at large k values or short wavelengths; at longer wavelengths, the destabilization due to diffusion into the supercooled liquid dominates.

The dividing line is marked by the combination of $d_0 l$, which is most conveniently expressed as

$$\lambda_S = 2\pi/k_S = 2\pi\sqrt{d_0 l} \qquad (10\text{-}51)$$

assuming $D = D'$. This will be denoted as the "stability length", which gives a measure of the typical lengths for diffusion-generated ripples on the interface, since the fastest-growing mode has a wavelength $\lambda_f = \sqrt{3}\,\lambda_S$. This is the first explicit example for the fundamental scaling relation Eq. (10-1) mentioned in the introduction to this chapter.

10.3 Basic Experimental Techniques

Before discussing the various growth models, a short overview of selected recent experiments that contributed to our present understanding will be given.

An exhaustive treatment of the subject is not intended here; only some of the characteristic technique will be described. No specific reference will be given to the many solidification processes available. The main emphasis will be on growth of crystals, because direct evidence on nucleation mechanisms is not yet available. The reader interested in nucleation experiments is referred to a review by Perepezko et al. (1987).

There are two essentially different situations of solidification, or, more generally, of phase transformation (Fig. 10-1):

i) free (undercooled or equiaxed) growth,

ii) constrained (columnar of directional) growth.

In the first case (Fig. 10-1a), the melt undercools, before transforming into a crystal, until nucleation sets in. The crucible which contains the melt must be less effectively catalytic to crystallization than the heterogeneous particles in the melt. The crystals then grow with an interface temperature above the temperature of the surrounding undercooled liquid. Heat is carried into the liquid. The temperature gradient at the solid-liquid interface in the liquid is therefore negative and approximately zero in the solid owing to the initially small crystal size relative to the thermal boundary layer.

In the second case of constrained growth (Fig. 10-1b), the temperature gradient is positive in both liquid and solid, and the first solid is either formed in contact with the chill mold or is already present, as in surface treatment by lasers, for example, where growth occurs epitaxially after remelting. In case i), nucleation is essential in controlling the microstructure (the grain size), while in case ii), nucleation is of minor importance.

Typical technical processes with respect to these two classes of solidification are as follows:

i) casting into low conductivity molds (ceramics), producing small temperature gradients, or additing inoculating agents or stirring the melt, thereby producing many heterogeneous or homogeneous nuclei;

ii) processes with high heat flux imposed through strong cooling of the solid such as

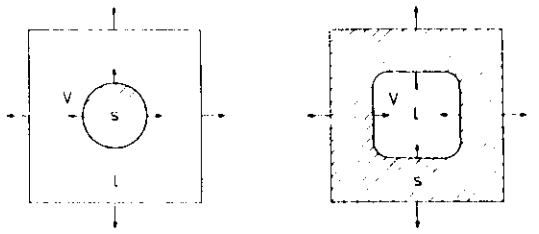

a) Free (or undercooled or equiaxed) growth

b) Directional (or constrained or columnar) growth

Figure 10-1. Growth in (a) undercooled melt (free growth) and (b) superheated melt (directional growth). The arrows on the outside of the mold represent the heat flux, and the arrows at the solid-liquid interface, the growth direction.

continuous casting, welding, laser treatment, or through heating of the melt and cooling of the solid, such as in single crystal growth or *Bridgman type* directional solidification experiments. (See also Vol. 15, Chap. E.)

In free growth, the undercooling ΔT of the melt is given and controls the growth rate V and the scale (spacing λ or tip radius R) of the forming microstructure. In directional growth, the rate of advance of the isotherms is imposed by heat flux leading to an imposed growth rate. This, in turn, controls the interface temperature (undercooling) and the microstructural scales. These three variables (temperature, growth rate, and microstructural size) have to be measured experimentally for a quantitative comparison of theory and experiment. A number of material parameters of the alloy system have to be known, such as the solid-liquid interfacial energy, the diffusion coefficient, the stable and metastable phase diagram, etc.

The experimental techniques are divided into two classes: those which produce relatively small growth rates and those which aim for high solidification rates. The corresponding experimental setup is quite different, and some of its important elements will be described below.

10.3.1 Free Growth

Small growth rates

In free growth, the undercooling ΔT or the temperature of the melt $T_0 = (T_m - \Delta T)$ is imposed on the system, and the growth rate V and the microstructural scale are the dependent variables. For small undercoolings, and therefore small growth rates, all three variables can be measured precisely if the substance is transparent. The crystallization of nontransparent metals, however, is the major issue in solidification studies relevant for technical applications.

Instead of investigating the crystallization of metallic systems directly, suitable model substances have to be found. These are generally organic "plastic crysals" which, like metals, have simple crystal structures and small melting entropies (Jackson, 1958). One of the substances which behaves very similarly to metals and is also well characterized in its properties is succinonitrile (SCN) (Huang and Glicksman, 1981). Substantial results with this material have been obtained by Glicksman et al. Their careful experimental approach has not only produced the most precise measurements known at that time but has also stimulated new ideas about possible mechanisms of structure formation through the discrepancy found between the observations and the predictions of previous theories.

Fig. 10-2 shows the experimental setup developed by Glicksman et al. (1976) to study free dendritic solidification. After zone melting the material is introduced in the growth chamber (C), which is then slowly undercooled with the heaters (A) and (B) in order to avoid premature crystallization. By careful adjustment of heater (A), growth starts there, and a crystal grows through the orifice in chamber (C). From then on, the dendrite can grow freely into the undercooled liquid and its shape, size, and growth rate, depending on supercooling, is measured with the aid of photographs. In order to choose a proper projection plane of observation, the whole equipment can be translated, rotated, and tilted at (D). A series of similar experiments have been performed at low temperatures with rare gases (Bilgram et al., 1989).

In this kind of experiment, it is important to avoid thermal or solutal convection as this transport mechanism will change the results and make them difficult to compare with diffusional theory. Glicksman et al. (1988) have shown the effect of thermally driven convection on the growth morphology of pure SCN dendrites. Fig. 10-3 clearly shows a strong deviation of the growth rate at undercoolings smaller then 1 K, where convection is believed to accelerate dendrite growth. Here V_0 is the dendrite tip rate of pure diffusion controlled growth.

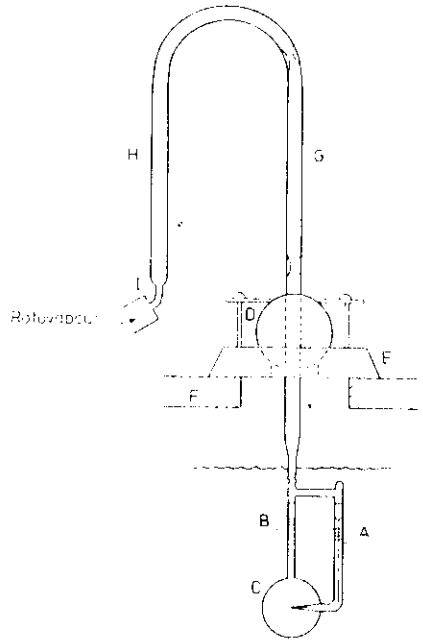

Figure 10-2. Equipment for free growth of organic dendrites (Glicksman et al., 1976). A and B control heaters; C growth chamber; D tilting and rotating device; F tank cover; G and H zone-refining tubes.

Another type of slow dendrite growth in undercooled media has been analyzed by Trivedi and Laorchan (1988). These authors made interesting in situ observations during the crystallization of glasses. Even if the driving forces in these systems may be very large, growth is heavily restricted due to slow diffusion and attachment kinetics.

Large growth rates

In order to explore solidification behavior under very large driving forces, Willnecker et al. (1989) have measured dendrite growth rates in highly undercooled Ni and Cu–Ni alloys. Nucleation is avoided by levitation melting in an ultrahigh vacuum environment. Undercooling of more than 300 K leading to growth rates of up to 70 m/s have been reached. Such large undercoolings have been obtained by several authors before, but growth rates have not been measured. Interesting results in Ni–Sn alloys have also been obtained by high speed cinematography of highly undercooled samples. These results were produced by Wu et al. (1987) by encapsulating the melt in glass. They tried to measure tip radii from the photograph. In that case, however, only the thermal images of the

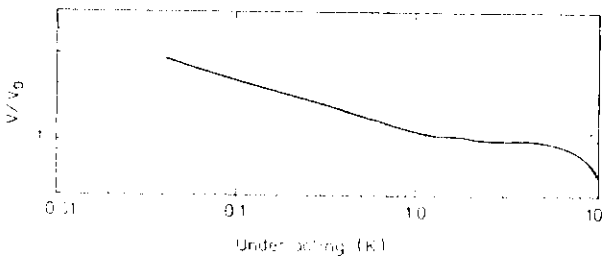

Figure 10-3. Ratio of measured growth rate V to predicted rate from diffusion theory, V_0, as a function of undercooling (Glicksman et al., 1988).

dendrites could be seen, their tips being controlled by solute diffusion. The radii from the thermal images are therefore believed to be much larger then the real radii.

10.3.2 Directional Growth

Small growth rates

Understanding of solidification improved in the 1950s when the need for better semiconductor materials stimulated research using directional growth techniques such as zone melting and Bridgman growth. Later, directional casting became an important topic of research for the production of single crystal turbine blades. Fig. 10-4 shows the essentials of two techniques: Bridgman type and *chill plate* directional solidification. The first of these processes (Fig. 10-4 a) has the advantage of being able to produce a constant growth rate and constant temperature gradient over considerable length and to allow for a certain uncoupling of these two most important variables. It was this latter advantage which, in the beginning of solidification research, gave deep insight into the mechanisms of growth. With one growth rate, but varying temperature gradient (or vice versa), plane-front, cellular, or dendritic morphologies could be grown, and their evolution studied. Important concepts (constitutional undercooling, cell growth, etc.) have been developed with the aid of observations made with the Bridgman type of equipment. The experiments by Hunt et al. (e.g., Burden and Hunt, 1974) deserve special attention, as the quality of the measurements has been pushed to high standards.

Furthermore, most of the work on *directional eutectics* and their growth mechanisms has been performed with the aid of this technique. In eutectic solidification, the microstructure after transformation is the same size (interphase spacing λ) as that found at the growing interface and thus allows for direct conclusions to be drawn concerning the growth process. This important variable can therefore be easily determined in nontransparent metals. This, however, is not possible with the corresponding quantity of the dendrite, the tip radius R, as discussed earlier.

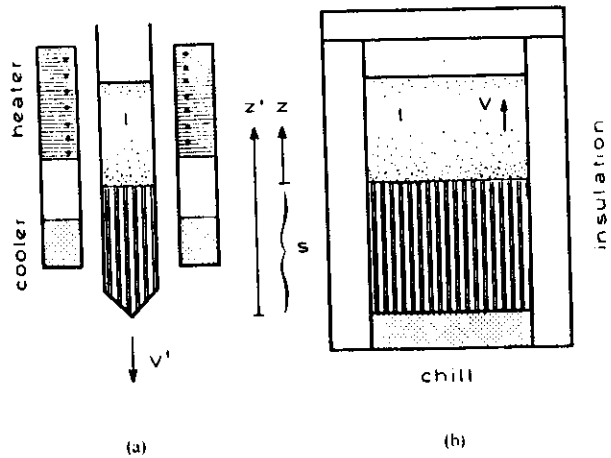

Figure 10-4. Basic methods of directional solidification, (a) Bridgman type furnace and (b) directional casting.

One disadvantage of the Bridgman experiment is the need for a small diameter due to heat flux constraints. This is avoided in the process shown in Fig. 10-4 b (*directional casting*), for which, however, a separation of the variables V and G is not possible. Therefore, this method is less interesting for scientific purposes.

For in situ observation of microstructure formation, one can also use plastic crystals in an experimental arrangement which resembles a two dimensional Bridgman apparatus, as shown in Fig. 10-5. Two glass slides which contain the organic analogue are moved over a heating and cooling device producing a constant temperature gradient G_T. This can be controlled to certain limits by the temperature difference

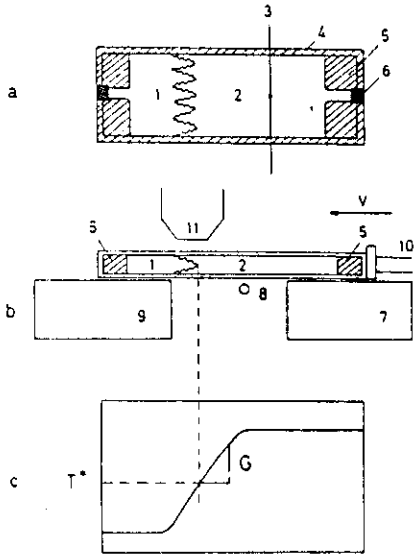

Figure 10-5. Schematic diagram of growth cell (a, b) for observation of directional solidification of transparent substances under microscope (Esaka and Kurz, 1985). 1 solid; 2 liquid; 3 thermocouple; 4 cell; 5 low melting glass; 6 araldite seal; 7 and 8 heaters; 9 cooler; 10 drive mechanism; 11 microscope. In (c) the temperature distribution in the growth cell is shown.

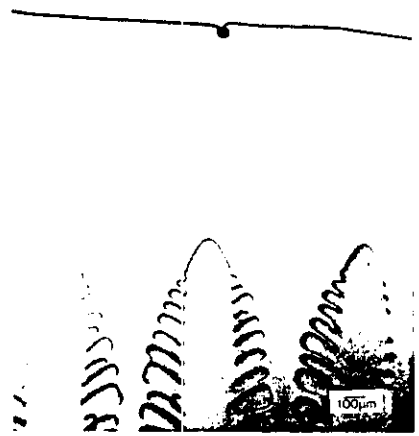

Figure 10-6. Array of dendrites approaching a fine thermocouple for measurement of the tip temperature and temperature gradient. Diameter of the bead, approximately 50 µm (Esaka and Kurz, 1985).

and distance between heater and cooler. A thin thermocouple incorporated into the alloy allows for measurement of interface temperature (Fig. 10-6) and temperature gradient in liquid and solid (Esaka and Kurz, 1985; Somboonsuk and Trivedi, 1985; Trivedi and Somboonsuk, 1985; Trivedi and Kurz, 1986).

Large growth rates

There have been attempts to push the growth rate in Bridgman type experiments. The first to reach rates of the order of several mm/s were Livingston et al. (1970). The best way to reach much higher rates is through laser resolidification using a stable high-powered laser. In this case, a small melt pool with very steep temperature gradients is created (for a remelted layer of 100 mm thickness, the temperature gradi-

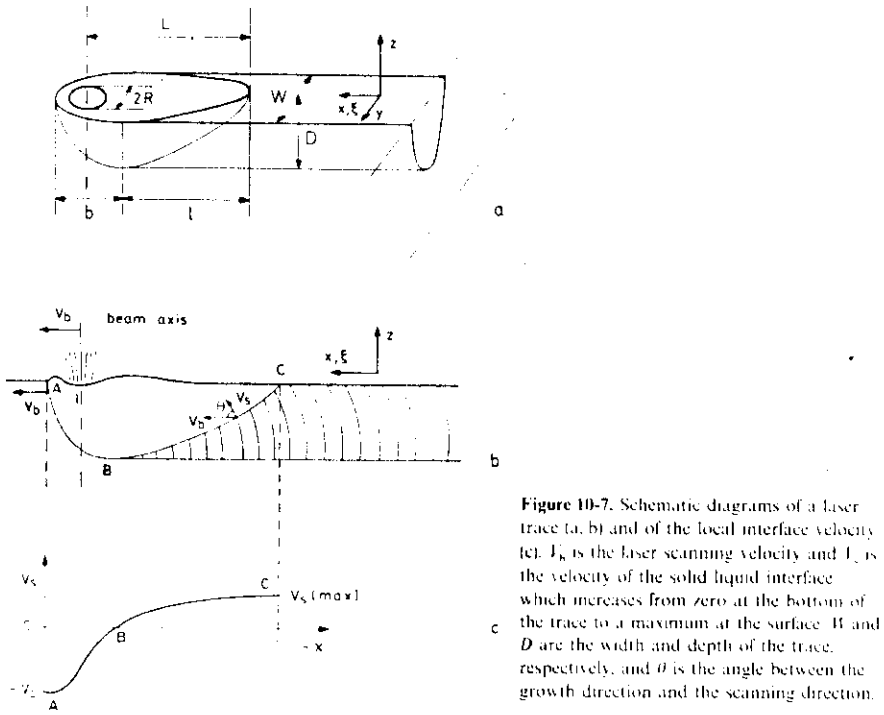

Figure 10-7. Schematic diagrams of a laser trace (a, b) and of the local interface velocity (c). V_b is the laser scanning velocity and V_s is the velocity of the solid liquid interface which increases from zero at the bottom of the trace to a maximum at the surface. W and D are the width and depth of the trace, respectively, and θ is the angle between the growth direction and the scanning direction.

ent G_l is of the order of 5000 K/mm). The microstructure is then constrained to follow closely the heat flow which is perpendicular to the isotherms (Fig. 10-7). Therefore, knowing the angle θ between the direction of growth and the direction and rate of movement of the laser beam allows for the growth rate to be obtained locally, even in the electron microscope (Zimmermann et al., 1989). Note that the growth rate increases from zero at the interface with the substrate up to a maximum at the surface. The only unknown which would be extremely difficult to measure is the interface temperature.

Consequently, in the case of rapid directional growth one can determine the post-solidification microstructure and its growth rate as well as the bath temperature and the growth rate in rapid undercooled growth. In both cases, the measurement of the interface temperature is not possible for the time being and must be evaluated through theory alone.

10.4 Free Dendritic Growth

The most popular example of dendritically (= tree-like) growing crystals is given by snowflakes. The six primary arms on each snowflake look rather similar but there is an enormous variety of forms between different snowflakes (Nakaya, 1954). According to our present knowledge, the similarity of arms on the same snowflake is an indication for similar growth conditions over the arms of a snowflake, the variation of structure along each arm being an indication for a time-variation of external growth conditions.

In order to formulate a theory, some specific assumptions about these environmental conditions must be made. Unfortunately, the growth of a snowflake is an extremely complicated process, involving strongly anisotropic surface tension and kinetics and the transport of heat, water vapor, and even impurities. Therefore, at first we will drastically simplify the model assumptions. In the same spirit, a number of precise experiments has been performed to identify quantitatively the most important ingredients for this mechanism.

In its simplest form, dendritic growth requires only a supercooled one-component liquid with a solid nucleus inside, so that the heat released at the solid-liquid interface during growth is transported away into the liquid. This is precisely the condition given in Section 10.2.3 concerning a sphere growing into the supercooled, and therefore metastable, liquid. A relatively straightforward stability analysis (Mullins and Sekerka, 1963, 1964; Langer, 1980a) shows that the solid tends to deviate from spherical form as soon as its radius R has become bigger than seven times the critical radius $R_c = 2d_0/\Delta$. A time-dependent analysis was also made recently (Yokoyama and Kuroda, 1988). During the further evolution, these deformations evolve into essentially independent arms, the primary dendrites.

The growth of such dendrites is a very widespread phenomenon, as will become clearer in Section 10.5 on directional solidification. There are also close relations to processes called diffusion-limited aggregation (DLA) (for a review see Meakin, 1988; for relation to crystal growth, see Uwaha and Saito, 1990; Xiao et al., 1988). For these processes, some specific assumptions are made about the incorporation of atoms into the advancing interface which are not easily carried over into the motion of surface tension, etc. Another line of closely related problems concerns the viscous flow of two immiscible liquids (Saffmann and Taylor, 1958; Brener et al., 1988; Dombre and Hakim, 1987; Kessler and Levine, 1986c). We will briefly refer to this in Section 10.5.

10.4.1 The Needle Crystal Solution

In this subsection, we will look at an isolated, needle-shaped crystal growing under stationary conditions into a supercooled melt. A stationary condition, of course, only holds in a frame of reference moving at velocity V in the positive z-direction. For a one-component crystal, the latent heat of freezing must be diffused away into the liquid.

The process is therefore governed by the heat-diffusion Eq. (10-25)

$$0 = \nabla^2 u + \frac{2}{l}\frac{\partial u}{\partial z} \qquad (10\text{-}52)$$

where we have used a dimensionless form, Eq. (10-30), for a stationary pattern together with the definition of the diffusion length, Eq. (10-31). If the diffusion constants in the crystal and the liquid are different, we would have to use two diffusion lengths. The continuity Eq. (10-27) at the interface is for normal velocity

$$V_n = -D_L \hat{n} \cdot \nabla u_L + D_L \cdot \hat{n} \nabla u_S \qquad (10\text{-}53)$$

where the subscripts L and S denote gradients taken on the liquid side and on the solid side of the interface. This is known as the "two-sided" model (Langer and Turski,

1977) and, because of identical diffusion constants, as the "symmetrical" model. The generalization to different diffusion constants is simple.

The boundary condition at the interface is

$$u_i = -d_0 K - \beta V \tag{10-54}$$

and at infinity

$$u_\infty = -\Delta \tag{10-55}$$

as introduced before in Eqs. (10-37) and (10-41), respectively. Note that a constant like Δ may be added on the right hand side of both equations without changing the results apart from this additive constant in the u-field, as frequently appears in the literature. The definition of Δ follows easily from Eqs. (10-24) and (10-41).

In general, the capillary length d_0 and the kinetic coefficient β are anisotropic because of the anisotropy of the crystalline lattice, but they are not directly related (Burkhardt et al., 1977). For the moment, we will assume $\beta = 0$, i.e., the interface kinetics should be infinitely fast. Even then, the curvature K in Eq. (10-54) is a complicated function of the interface profile. The simplest approximation for the moment, therefore, is to ignore both terms on the r.h.s. of the boundary condition, which corresponds to setting the surface tension to zero. The boundary condition is then simply a constant (=0 in our notation).

A second-order partial differential equation such as the diffusion equation can be decomposed in the typical orthogonal coordinate systems, and one therefore obtains a closed form solution for the problem with a boundary of parabolic shape: a rotational paraboloid in three dimensions and a simple parabola in two dimensions. This is the famous "Ivantsov" solution (Ivantsov, 1947).

The straightforward way to look at this problem is as a coordinate transformation from the cartesian $\{x, z\}$ frame, where z is the growth direction, to the parabolic coordinates $\{\xi, \eta\}$:

$$\xi = (r - z)/\varrho; \quad \eta = (r + z)/\varrho$$

where r is the radial distance $\sqrt{x^2 + z^2}$ from the origin, and ϱ is a constant. After transforming the differential operators in Eqs. (10-52) and (10-53) to $\{\xi, \eta\}$ (Langer and Müller-Krumbhaar, 1977, 1978), it can be seen immediately that $\eta(\xi) = \eta_S = 1$ for the interface is a solution to the problem confirming the parabolic shape of the interface, with ϱ being the radius of curvature at the tip.

This *Ivantsov radius*, ϱ, is now related to the supercooling Δ and the diffusion length l by the relation

$$\Delta = \begin{cases} P\, e^P E_1(P) & \text{3-dim} \quad (10\text{-}56\,a) \\ \sqrt{\pi P}\, e^P \operatorname{erfc}(\sqrt{P}) & \text{2-dim} \quad (10\text{-}56\,b) \end{cases}$$

which for small $\Delta \ll 1$ gives

$$\Delta \approx \begin{cases} P(-\ln P - 0.5772\ldots) & \text{3-dim} \\ \sqrt{\pi P} & \text{2-dim} \end{cases}$$

and for $\Delta \to 1$ asymptotically

$$\Delta \approx \begin{cases} 1 - 1/P & \text{3-dim} \\ 1 - 1/2P & \text{2-dim} \end{cases}$$

where the dimensionless *Peclet number* P is defined as the relation

$$P = \varrho/l = \varrho V/2D \tag{10-57}$$

between tip radius and growth rate. $E_1(P)$ is the exponential integral

$$E_1(P) = \int_P^\infty \frac{e^{-t}}{t}\, dt \tag{10-58}$$

and erfc is the complement of the error function.

Eq. (10-56) may be interpreted as an expression of supercooling in terms of the Peclet number. This explanation is important because the following considerations of surface tension give only very small corrections to the shape of the needle crystal. Therefore, Eq. (10-56) will be essential valid also with nonzero surface tension at typical experimental undercoolings of $\Delta \cong 10^{-1}$. An important consequence is that the scaling results derived below then become independent of the dimensionality (2 or 3), if the supercooling is expressed through the Peclet number.

The basic result of Eqs. (10-57) and (10-48) is that the growth rate of this parabolic needle is inversely proportional to the tip radius, but no specific velocity is selected. For experimental comparison, one makes a fit of the tip shape to a parabola. The tip radius of that parabola is then compared with the Ivantsov radius ϱ. The actual tip radius will be different from the Ivantsov radius of the fit parabola, because of surface-tension effects. Before we consider surface tension explicitly we now give an integral formulation for the problem using *Green's functions*, which has proven to be more convenient for analytical and numerical calculations (Nash and Glicksman, 1974).

The value of a temperature field $u(x, t)$ in space and time is obtained by multiplying the Green's function of the diffusion equation with the distribution for sources and sinks for heat and integrating the product over all space and time. In our case, this explicitly gives

$$u(x,z,t) = \int_{-\infty}^{t} dt' \int dx'\, G(x - x', z - \zeta(x,t') + V(t - t'); t - t') \left\{ V + \frac{\partial \zeta}{\partial t'} \right\} \tag{10-59}$$

(Langer, 1987 b), with the Green's function

$$G(x,z,t) = \frac{1}{(4\pi D t)^{3/2}} \exp\left(-\frac{|x|^2 + z^2}{4Dt} \right) \tag{10-60}$$

for diffusion in an infinite three-dimensional medium (symmetrical case). ζ is the z coordinate of the interface. The source term $\{\ldots\}$ in this equation is obviously the interface in the frame of reference moving at velocity V in the z-direction. This equation already contains the conservation law or the continuity equation at the interface. Furthermore, it is valid everywhere in space and, in particular, at the interface $z = \zeta(x, t)$, where the l.h.s. of Eq. (10-59) is then set equal to Eq. (10-54). Here u is assumed to vanish at infinity, so Δ must be added on the l.h.s.

In the two-dimensional case and for stationary conditions this can be rewritten as

$$\Delta - \frac{d_0}{\varrho} K\{\zeta\} = P I_2\{P, x, \zeta(x)\} \tag{10-61}$$

(Langer, 1987 b) with

$$I_2\{P, x, \zeta(x)\} = \frac{1}{2\pi} \int_0^\infty \frac{dy}{y} \int_{-\infty}^{+\infty} dx' \cdot \exp\left\{ -\frac{P}{2y} [(x - x')^2 + (\zeta(x) - \zeta(x') + y)^2] \right\} \tag{10-62}$$

In addition, it was shown (Pelce and Pomeau, 1986) that with the parabolic Ivantsov solution

$$\zeta(x) \to \zeta_{IV} = -\tfrac{1}{2} x^2 \tag{10-63}$$

one can obtain

$$P I_2\{P, x, \zeta_{IV}(x)\} = \Delta$$

which is independent of x, with Δ coming from Eq. (10-56 b). Note that from Eq. (10-59) to (10-61) we have replaced x by $x\varrho$ etc., which mirrors the scaling form of Eq. (10-57).

We are now ready to consider a nonzero capillary length d_0 Eq. (10-39), which we generalize to be anisotropic:

$$d_0 \to d = d_0(1 - \varepsilon \cos 4\vartheta) \tag{10-64}$$

where ϑ is the angle between the interface-normal and the z axis (2-dim, 4-fold an-

isotropy), and $\varepsilon > 0$ is the relative strength of that anisotropy. This form arises from the assumption

$$\gamma = \gamma_0(1 + \delta \cos 4\vartheta) \tag{10-65}$$

for anisotropic surface tension, which gives through Eq. (10-22) $\varepsilon = 15\delta$. Note that it is the stiffness γ'' which dominates the behavior, not γ directly. Along the Ivantsov parabola, the angle ϑ is related to x:

$$d = d_0\, A(x): \quad A(x) = 1 - \varepsilon + \frac{8\varepsilon x^2}{(1+x^2)^2} \tag{10-66}$$

and the deviation from $\zeta_{\mathrm{IV}}(x)$ can be expressed as

$$-\frac{d}{\varrho P} K\{\zeta\} = I_2\{P, x, \zeta\} - I_2\{P, x, \zeta_{\mathrm{IV}}\} \tag{10-67}$$

For convenience we combine some parameters into a dimensionless quantity σ:

$$\sigma = \frac{2D d_0}{\varrho^2 V} = \frac{d_0}{2D P^2}\, V \tag{10-68}$$

so that the l.h.s. of Eq. (10-67) becomes

$$-\frac{d}{\varrho P} K = -\sigma A K \tag{10-69}$$

the curvature as usual being

$$K\{\zeta\} = -\frac{\partial^2 \zeta/\partial x^2}{[1 + (\partial \zeta/\partial x)^2]^{3/2}} \tag{10-70}$$

It should be clear at this point that the parameter σ in Eq. (10-68) plays an important role, because it multiplies the highest derivative in Eqs. (10-61) and (10-67). More specifically, one can expect that the resulting structure $\zeta(x)$ of the interface depends on the material properties and experimental conditions only through this parameter σ (within the model assumptions) which becomes a function of P and ε

$$\sigma = \sigma(P, \varepsilon) \tag{10-71}$$

The importance of the parameter σ was recognized in an earlier stability analysis (Langer and Müller-Krumbhaar, 1978, 1980) of the isotropic case. It turned out later, however, that the anisotropy is essential in determining the precise value of σ. This is insofar crucial as $\varepsilon \to 0$ implies $\sigma \to 0$, i.e., no stationary needle solutions exist without anisotropy.

We will now briefly describe the analysis of Eq. (10-67). The details of this singular perturbation theory are somewhat involved, and we therefore have to omit them here. The basic method was formulated by Kruskal and Segur (1985), and the first scaling relations for dendritic growth were obtained for the boundary-layer model (Ben Jacob et al., 1983, 1984). A good introduction to the mathematical aspects can be found in the lectures by Langer (1987b), on which the following presentation is based. The most mathematically sound (nonlinear) solution seems to have been given by Ben Amar and Pomeau (1986). For convenience, we have sketched a slightly earlier linearized version here, while the nonlinear treatment leads to basically the same result.

Looking for a solution to Eq. (10-67) in linear approximation, one starts by expanding to first-order in

$$\zeta_1(x) = \zeta(x) - \zeta_{\mathrm{IV}}(x) \tag{10-72}$$

In the limit of the small Peclet number, and with the substitution

$$\zeta_1(x) = (1 + x^2)^{3/4} Z(x) \tag{10-73}$$

is given

$$(\hat{\mathsf{B}} + \hat{\mathsf{A}}) \cdot Z(x) = \sigma (1 + x^2)^{3/4} \tag{10-74}$$

where $\hat{\mathsf{B}}$ is a selfadjoint differential operator

$$\hat{\mathsf{B}} = \sigma \frac{d^2}{dx^2} + \frac{(1+x^2)^{1/2}}{A(x)} + 0(\sigma) \tag{10-75}$$

and

$$\hat{\mathsf{A}} \cdot Z(x) = \frac{(1+x^2)^{3/4}}{2\pi\, A(x)} \cdot \mathscr{P} \int_{-\infty}^{+\infty} \mathrm{d}x' \frac{(x+x')(1+x'^2)^{3/4}}{(x-x')\left[1 + \frac{1}{4}(x+x')^2\right]} \cdot Z(x') \tag{10-76}$$

with $\mathscr{P}$ denoting the principal value.

The integral kernel in Eq. (10-76) is antisymmetric apart from a prefactor $A(x)^{-1}$. An analytic solution to Eq. (10-74) has not yet been found. A necessary condition to be fulfilled by the present inhomogeneity is that it should be orthogonal to the null-eigenvectors $\tilde{Z}(x)$ of the adjoint homogeneous problem:

$$(\hat{\mathsf{B}} + \hat{\mathsf{A}}^{\dagger}) \cdot \tilde{Z}(x) = 0 \tag{10-77}$$

such that

$$A(\sigma, \varepsilon) = \int_{-\infty}^{+\infty} \mathrm{d}x \frac{\tilde{Z}(x)}{(1+x^2)^{3/4}} = 0 \tag{10-78}$$

In fact, this is already a sufficient condition for the solvability of the inhomogeneous equation, but it is not very simple.

A solution for $\tilde{Z}(x)$ can be found by a WKB-technique, for which we refer to the literature (Kessler et al., 1987, 1988; Langer, 1987b; Caroli et al., 1986a, b). The result for the solvability condition, Eqs. (10-71) and (10-78), is that the parameter σ should depend on anisotropy ε as

$$\sigma \approx \sigma_0 \varepsilon^{7/4} \tag{10-79}$$

in the limit $P \to 0$, $\varepsilon \to 0$, with some constant prefactor σ_0 of order unity.

Eq. (10-79) is the solution for the needle-shaped crystal with capillary anisotropy $\varepsilon > 0$, together with Eq. (10-68). Note again that ε is the anisotropy of capillary length, which differs by a factor from surface-tension anisotropy Eq. (10-65). Formally, there is not just one solution but infinitely many, corresponding to slow, fat needles which are dynamically unstable. Only the fastest of these needle solutions appears to be stable against tip-splitting fluctuations and may thus represent an 'observable' needle crystal, as expressed by Eq. (10-79). For practical comparison, experimental data is best compared with numerical solutions of Eq. (10-61), because the applicability of Eq. (10-79) seems to be restricted to very small values of ε (Meiron, 1986; Ben Amar and Moussallam, 1987; Misbah, 1987). This will be discussed further in the next section. Finally, one notable point is that we have only considered the two-dimensional case here, but the solvability condition in three dimensions (Caroli et al., 1986b; Barbieri et al., 1987; Kessler and Levine, 1986d) produces exactly the same scaling result for axisymmetric dendrites.

10.4.2 Side-Branching Dendrites

This section gives a summary of the present understanding of dendritic growth. It is centered around numerical simulations of isolated side-branching dendrites in a one-component system where heat diffusion is the relevant dynamical process. Alternatively, it also describes dendritic growth from a two-component system at essentially constant temperature. In the latter case, one should also discuss the phase diagram which will be covered later in the section on directional solidification. For many typical cases of growth from a dilute solution, however, the information contained in this section should be sufficient.

We start with the definition of the model as resulting from the set of Eqs. (10-52) to (10-55). The dynamics come from the conservation law, Eq. (10-53), at the interface. As in the previous section, one uses here the form of dimensionless units which were introduced in Section 10.2.3 for the case of heat diffusion. The case of chemical dif-

fusion (temperature then being assumed constant $= T_0$) can be treated by the same equations. The normalization is described in Section 10.5.2. For convenience, we will simply summarize here the basic formulas for both cases.

In contrast to Eqs. (10-37) and (10-54), we will now normalize the following equation to obtain $u = 0$ at infinity, which results from adding the constant Δ to the field-variable u in all equations. Then, the diffusion field becomes

$$u = \begin{cases} (T - T_\infty)/(L_m c_p^{-1}) \\ \text{thermal diffusion} \\ (\mu - \mu_\infty)/(\Delta C\, \partial\mu/\partial C) \\ \text{chemical diffusion} \end{cases} \tag{10-80}$$

where μ is the chemical potential difference between solute and solvent and ΔC ($0 \le \Delta C \le 1$) is the miscibility gap at the operating temperature T_0.

The dimensionless supercooling is given as

$$\Delta = \begin{cases} (T_m - T_\infty)/(L_m c_p^{-1}) & \text{thermal} \\ (\mu_{eq} - \mu_\infty)/(\Delta C\, \partial\mu/\partial C) & \text{chemical} \end{cases} \tag{10-81}$$

The capillary length is then

$$d = [\gamma(\vartheta) + \gamma''(\vartheta)] \cdot \begin{cases} T_m c_p L_m^{-2} & \text{thermal} \\ \Delta C^{-2} (\partial\mu/\partial C)^{-1} & \text{chemical} \end{cases} \tag{10-82}$$

The quantity $\partial\mu/\partial C$ is not easily measured, but for small $\Delta C \ll 1$ of a dilute solution, it can be related to the slope of the liquidus line dT/dC at $T_0 = T_m$ by

$$\frac{\partial\mu}{\partial C} \approx \frac{L_m}{T_m \Delta C} \left| \frac{dT}{dC} \right| \tag{10-83}$$

(Mullins and Sekerka, 1963, 1964; Langer, 1980a). Note that the chemical capillary length can be several orders of magnitude larger than the thermal length.

The boundary condition, Eq. (10-54), then simply changes to

$$u_i = \Delta - d\kappa - \beta V \tag{10-84}$$

where now the anisotropic capillary length d was used. The kinetic coefficient also may depend on concentration (Caroli et al., 1988), which we ignore here. Far away from the interface in the liquid, the boundary condition becomes

$$u_\infty = 0 \tag{10-85}$$

For the chemical case, we may practically ignore diffusion in the solid.

The diffusion Eq. (10-52) and the conservation law, Eq. (10-53), remain unchanged, and the diffusion length is defined as before as $l = 2D_T/V$, with V being the average velocity of the growing dendrite.

There are, of course, important differences between two and three dimensions, as a three-dimensional needle crystal is not necessarily rotationally symmetric around its axis. Snow crystals, for example, show large anisotropies in directions orthogonal to the growth direction of the primary dendritic needle (Yokoyama and Kuroda, 1988). In the immediate neighborhood of the tip, however, the deviation from this rational symmetry is often small. Therefore, one may work with this two-dimensional model by using an "effective" capillary length. The scaling relations given below are expected to be insensitive to this apart from a constant prefactor of order unity in the $\sigma(\varepsilon)$-relation (Kessler and Levine, 1986b, d; Langer, 1987a).

The numerical simulations were performed for a two-dimensional crystal-liquid interface. In Fig. 10-8, we show a typical dendrite with side-branches resulting from the time-dependent calculations (Saito et al., 1987, 1988) (compare with the experimental result by Glicksman et al. (1976) in Fig. 10-9). The profile is symmetric around the axis by definition of the calculation. An approximately parabolic tip has been formed from which side-branches begin to grow further down the shaft (only

Figure 10-8. Free dendrite in stationary growth computed in quasistationary approximation for the two-dimensional case. Capillary anisotropy was $\varepsilon = 0.1$ (Saito et al., 1988). The parameter-dependence of the growth rate, tip-radius and sidebranch-spacing is consistent with analytical scaling results from solvability theory of the needle crystal.

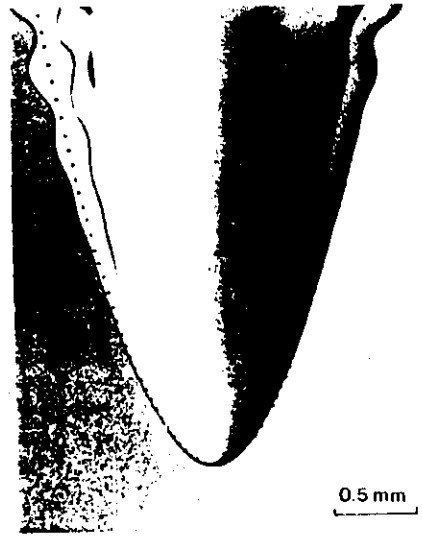

Figure 10-9. Dendrite tip in pure succinonitrile (SCN) at small undercoolings and inscribed parabola for measuring the tip radius (Huang and Glicksman, 1981).

the early stage of side-branch formation was considered). They have a typical distance which, however, is not strictly regular.

As a first result, the scaling relation, Eq. (10-68), was checked using the Peclet number from Eq. (10-56b). Experimentally, this requires the anisotropic capillary length and the supercooling to be varied independently. In Fig. 10-10, the scaled numerical results are shown as dots (and broken line) for two different supercoolings and compared with the results (full lines) for the stationary needle crystal. The upper line corresponds to the model with diffusion in the liquid only (Misbah, 1987) as used in the numerical simulation here. The lower line corresponds to the symmetrical model with equal diffusion in liquid and solid (Ben Amar and Moussallam, 1987). Appar-

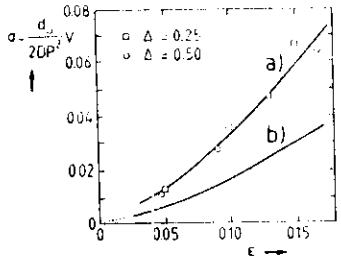

Figure 10-10. Scaling parameter $\sigma(\varepsilon)$ for free dendritic growth depending on capillary anisotropy ε and for two-dimensionless supercoolings Δ. Average capillary length is d_0, diffusion constant D, and Peclet number P. Comparison of numerical results (circles and squares, Fig. 10-8, one-sided model) with solvability results: (a) one-sided model (Misbah, 1987), (b) two-sided model (Ben Amar and Moussallam, 1987). The agreement is excellent, the independence upon supercooling is seen to work at least up to $\Delta = 0.5$.

ently, the two results look the same, apart from a factor of approximately two in σ. The extrapolated simulation results (broken line) lie in between but follow the scaling form both with respect to a variation of supercooling Δ and anisotropy ε. Note that in unscaled form (i.e., multiplying with P^2) the data for the two supercoolings would differ by about two orders of magnitude!

From an experimental point of view, it is better to use Fig. 10-10 rather than Eq. (10-79) for comparison, as the range of validity of Eq. (10-79) seems to be restricted to rather small values of ε. For unknown material parameters such as diffusion constant, capillary length, and anisotropy, one still can check the scaling relation of the growth rate V through the Peclet number, Eq. (10-56) depending on supercooling. Eq. (10-68) should then give a constant, although arbitrary, value of σ. This scaling result has already been confirmed experimentally in the 1970s, when the full theory did not yet exist (Langer and Müller-Krumbhaar, 1978, 1980). At that time, it was assumed ("marginal stability" hypothesis) that a universal value of $\sigma \approx 0.03$ was determined by a dynamic mechanism independent of anisotropy. The results for the needle crystal together with these numerical simulations now show that σ depends on anisotropy ε as shown in Fig. 10-10. Experimental tests on the ε-dependence (Section 10.4.3) are still rather sparse and do not quite fit that picture for reasons not well understood.

So far we have only looked at the relation between growth rate, anisotropy, and supercooling. We will now consider the size of the dendrite which is approximately parabolic, and which can probably be characterized by the radius of curvature at its tip.

This is a subtle point, as the tip radius cannot easily be directly measured. As an alternative, one can try to fit a parabola to the observed dendrite in the tip region. The tip radius of that fitted parabola should be interpreted as the Ivantsov radius ϱ which turns out to be slightly larger than the true tip radius R of the dendrite. The deviation of R from ϱ does not depend on supercooling Δ but depends on anisotropy ε. This is shown in Fig. 10-11, where a comparison is made between the dynamic numerical simulations (Saito et al., 1988) with the needle crystal solution in the limit of small Peclet number (Ben Amar and Moussallam, 1987). It can be seen that there is excellent agreement and that the actual tip radius R becomes smaller than the Ivantsov radius ϱ at increasing ε.

We now can relate the growth rate V and the tip radius R or the Ivantsov radius ϱ in order to check the scaling form Eq. (10-68) involving the radius rather than the Peclet number. The Ivantsov parabola and its radius ϱ basically originate from a global conservation law for the quantity (heat) released at the interface, while the tip radius R is a local geometric quantity. In practical experiments, by fitting a parabola

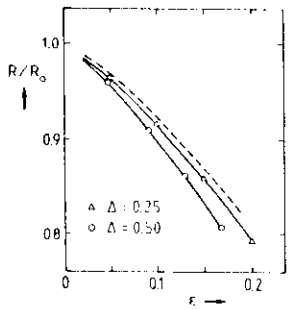

Figure 10-11. Tip-radius of free dendrite over Ivantsov-radius plotted versus anisotropy as a function of dimensionless supercooling. The numerical results (see also Fig. 10-8, 10-10) are consistent with the predictions from the needle solution (Ben Amar and Moussallam, 1987).

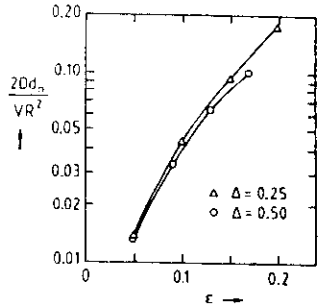

Figure 10-12. Numerical scaling result confirming $VR^2 = \text{const.}$ for free dendritic growth independent of supercooling Δ, depending on anisotropy ε only (Saito et al., 1988).

to the tip, one can interpolate between these two numbers, the result depending on how far down the shaft the fitting parabola is used. Using the actual radius R rather than the Ivantsov radius ϱ, perfect scaling can be seen in Fig. 10-12 with respect to supercooling Δ, even up to the very large value of $\Delta = 0.5$. Since for smaller supercoolings, $\Delta \leqq 0.1$, the difference between ϱ and R becomes negligible as shown in Fig. 10-11, one may safely use Eq. (10-68) as

$$VR^2 \approx V\varrho^2 = \frac{2Dd_0}{\sigma(\varepsilon)} = \text{constant} \qquad (10\text{-}86)$$

independent of supercooling Δ, to interpret experiments and to make predictions. The term "constant" here means that the product VR^2 depends on material parameters only. This is precisely the relation, Eq. (10-1), derived from qualitative considerations in the introduction of the article. This relation has been confirmed by the analysis of many experiments (Huang and Glicksman, 1981).

The final point to be discussed here concerns the side branches and their origin, spacing, and amplitudes. This issue is theoretically not completely settled, for all available analytical approximations cannot correctly handle the long-wavelength limit of side-branch perturbations. Moreover, the subject is somewhat technically involved. Therefore, we will only summarize the main arguments below and refer to the above-mentioned numerical simulations (Saito et al., 1988) for comparison with experiments.

An important quantity which characterizes the stability of flat moving interface ripples is the so-called stability length

$$\lambda_S = 2\pi \sqrt{l d_0} \qquad (10\text{-}87)$$

where d_0 is the capillary length, and l the diffusion length. Perturbations of wavelengths λ longer than λ_S will grow, while shorter wavelengths will decay with time. This quantity characterizes the competition between the destabilizing diffusion field through l against the stabilizing surface tension through d_0. A derivation of this Mullins-Sekerka instability was given in Section 10.2.4.

It is natural to assume, that this length scale is related to the formation of side-branches. A direct guess for the typical wavelength λ_2 of the side-branches is

$$\lambda_2 \gtrsim \lambda_S = 2\pi \sqrt{l d_0} = 2\pi\varrho\sqrt{\sigma} \qquad (10\text{-}88)$$

The remarkable result of the numerical simulation is shown in Fig. 10-13. Apparently, the ratio λ_2/λ_S is a constant of approximately 2.5, which is independent of supersaturation and anisotropy. This seems to be in quite good agreement with experiments (Glicksman et al., 1976; Dougherty et al., 1987; Honjo et al., 1985; Huang and Glicksman, 1981).

The experimental comparison was made, in fact, with an older theoretical concept (Langer and Müller-Krumbhaar, 1978), which did not correctly consider anisotropy. By accident, however, the experimental anisotropy of the material suc-

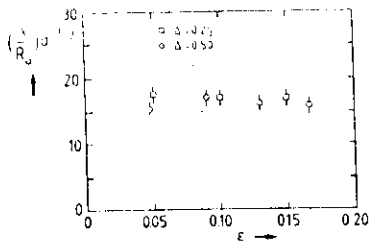

Figure 10-13. Scaled sidebranch-spacing $\lambda = \lambda_2$, normalized with Ivantsov-radius R_0 and $\sigma(\alpha)^{1/2}$, plotted versus capillary anisotropy for two supercoolings. No dependence on ε or Δ is found as expected (Saito et al., 1988).

cinonitrile (Huang and Glicksman, 1981) $\varepsilon \approx 0.1$ gave the same σ-value as the theoretical concept, and since ε cannot be varied easily, there was no discrepancy.

To summarize these results, it appears that the scaling relation, Eq. (10-88), shown in Fig. 10-13 from the numerical solution of the model in two dimensions is in agreement with the experimental results.

We will now give a somewhat qualitative explanation of the mechanism of side-branch formation as far as this can be deduced from the theoretical approaches. A linear stability analysis (Langer and Müller-Krumbhaar, 1978, 1980; Kessler and Levine, 1986a; Barber et al., 1987; Barbieri et al., 1987; Bensimon et al., 1987; Caroli et al., 1987; Kessler et al., 1987; Pelce and Clavin, 1987) indicates that the relevant modes for side-branch formation in the frame of reference moving with the tip consist of an almost periodic sinusoidal wave travelling from the tip down the shaft such that they are essentially stationary in the laboratory frame of reference (Langer and Müller-Krumbhaar, 1982; Deissler, 1987). The amplitude of these waves is not constant in space, but first grows exponentially in the tip region (Barbieri et al., 1987; Caroli et al., 1987). The exponential increase of that envelope in the tip region depends on the "wavelength" of the oscillatory part (Bouissou et al., 1990).

In contrast to the earlier analysis by Langer and Müller-Krumbhaar, all these modes are most likely stable, so that without a triggering source of noise, they would decay, and a smooth needle crystal would result. Some driving force in the form of noise due to thermal or hydrodynamic fluctuations is needed to generate side-branches, but apparently this is usually present. Estimates of the strength of these fluctuations (Langer and Müller-Krumbhaar, 1982; Barbieri et al., 1987; Langer, 1987a) are still somewhat speculative.

Given such a small noise at the tip, the exponentially increasing envelope over the side-branches into the direction of the tail then amplifies that noise so that the side-branches become visible. This happens over a range of about two to ten side-branch spacings. The actual selected wavelength of the side-branches in that tip region (assuming a white noise, triggering all modes equivalently), according to these considerations, is defined by the mode with the largest amplitude at a distance of about one "wavelength" away from the tip. This is the product of the average amplitude due to noise at the tip and the amplification factor from the envelope. Recent experiments (Bouissou et al., 1990) have qualitatively confirmed this frequency-dependent amplification but give a selected wavelength which is larger than theoretically proposed (Barbieri et al., 1987; Caroli et al., 1987). The reason for this discrepancy may be the different dimensionality (2d in theory, 3d in experiments) or, more likely, that the theory up to now may underestimate the long-wavelength side branch modes. We have to leave that point to further considerations.

We now summarize the presently established findings for free dendritic growth with respect to their *experimental significance*. A discussion of additional effects such as facetting will be given in Section 10.5.7 in the context of directional solidification.

For a given material with fixed D, d_0, and ε, the growth rate V depends upon supercooling Δ through Eq. (10-68), and with Peclet number P taken from Eq. (10-56). The dimensionless parameter σ is given in Fig. 10-10. This is demonstrated for various materials in Fig. 10-14. The size or tip radius of the dendrite is related to its velocity by Eq. (10-86) and can be taken from Fig. 10-12. The typical wavelength of the side-branches then is given by Eq. (10-88) and can be taken from Fig. 10-13. This gives all the basic information which should be valid in the tip region.

The fact that dendrites are really three-dimensional objects while the calculations were basically performed for two-dimensional models should not be a serious drawback, as long as the three-dimensional dendrites are approximately cylindrical in the immediate neighborhood of the tip.

We have so far ignored the influence of the kinetic coefficient β in Eq. (10-84). This omission is not likely to be very important for small growth rates, but for high growth rates, as in directional solidification, β should be taken into account. We will return to this point in Section 10.5.

10.4.3 Experimental Results on Free Dendritic Growth

The answer to the question of whether dendritic growth is diffusion controlled or controlled by anisotropic attachment kinetics, was sought by Papapetrou (1935), who was probably the first to make systematic in situ experiments on free dendritic growth. He examined dendritic crystals of transparent salts (KCl, NaCl, NH_4Br, $Pb(NO_3)_2$, and others) under microscope in aqueous solutions and proposed that the tip region should be close to a paraboloid of rotational symmetry.

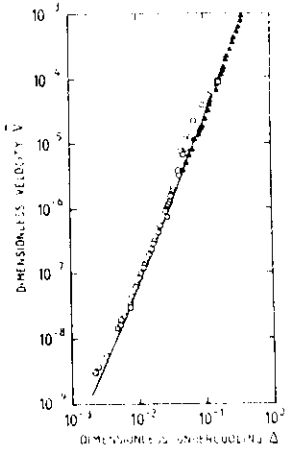

Figure 10-14. Dimensionless growth rate $\bar{V} = Vd_0/2D$ versus dimensionless undercooling Δ. The scaling quantity for the full curve (Langer and Müller-Krumbhaar, 1977, 1978) was taken as $\sigma = 0.025$ (coincidentally in agreement with the anisotropy of succinonitrile). For references to the experimental points see (Langer, 1980a). Excellent agreement between theory (solid line) and experiment is found.

Many years later, the extensive and systematic experiments by Glicksman and his co-workers made an essential contribution to our understanding of dendritic growth in pure undercooled melts (Glicksman et al., 1976; Huang and Glicksman, 1981). This research was initially concerned mainly with highly purified succinonitrile (SCN). It has been extended to cyclohexanol (Singh and Glicksman, 1989), water (Fujioka, 1978; Tirmizi and Gill, 1989), rare gases (Bilgram et al., 1989), and to other pure substances with a crystal an-

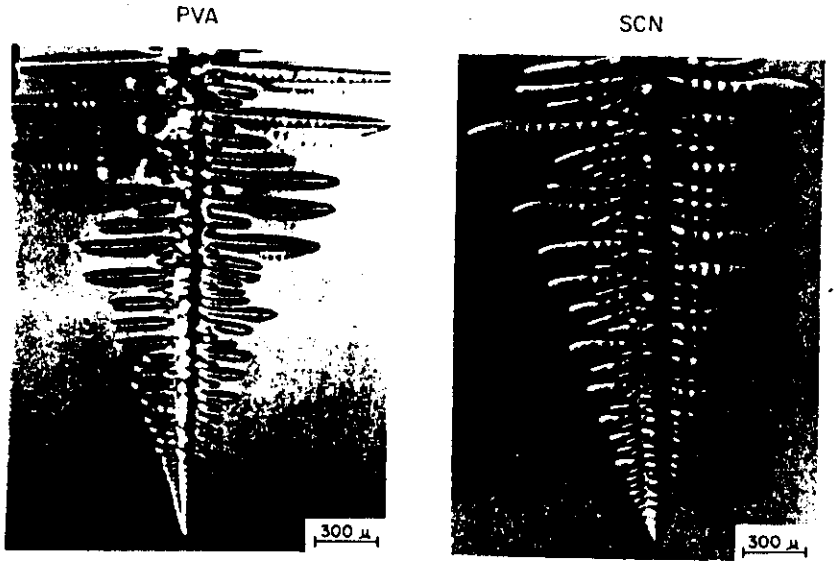

(a) (b)

Figure 10-15. Dendrite morphologies of two transparent materials with small melting entropies and cubic crystal structures (plastic crystals); (a) pivalic acid (PVA) and (b) succinonitrile (SCN) (Glicksman and Singh, 1989).

isotropy different from SCN such as pivalic acid (PVA) (Glicksman and Singh, 1989). Work on free growth of alloys includes NH_4Cl H_2O (Kahlweit, 1970; Chan et al., 1978), NH_4Br–H_2O (Dougherty and Gollub, 1988), SCN with acetone and argon (Glicksman et al., 1988; Chopra et al., 1988), PVA-Ethanol (Dougherty, 1990), and others.

The specific merit of the work of Glicksman et al. was that the systems for which they characterized all the properties, including surface energy, diffusion coefficient, phase diagram etc., have been examined. This led to the clear evidence in the mid 1970s that the theory of that time (using extremum arguments for the operating point of the tip) was not able to describe the results quantitatively.

At the same time, Müller-Krumbhaar and Langer worked on precisely the same problem and proposed a theory based on the stability of the growing dendrite tip called marginal stability criterion (Langer and Müller-Krumbhaar, 1977, 1978). Most of the existing experimental data could be fit using this criterion. Despite the fact that this theory incorrectly ignored the important role of anisotropy (as we know now), it inspired a number of new experiments and also attracted the interest of other physicists.

As has been said before, today's theory is consistent with the older approximate theory if one allows for a $\sigma(\varepsilon)$ value which varies with the anisotropy of the capillary length. The corresponding central equation for dendritic growth (Eq. (2) in Kurz and Trivedi, 1990) should therefore still apply.

Pure substances (thermal dendrites)

Fig. 10-15 shows dendrites of two different transparent materials with cubic crystal structure, face-centered cubic PVA, and body-centered cubic SCN (Glicksman and Singh, 1989). Qualitatively, both dendrites look similar, but their branching behavior shows some important differences. The unperturbed tip of PVA is longer with a sharper delineation of the crystallographic orientations. Glicksman and Singh (1989) found that PVA has a tenfold larger surface energy anisotropy than SCN (see Table 10-1). The tip radii and growth rates as a function of undercooling for both substances scale well when using the values 0.22 and 0.195 for σ respectively (Fig. 10-16). According to solvability theory, the great difference in the anisotropy constant ε should make a larger difference in $\sigma(\varepsilon)$ (compare with Fig. 10-10). The reason for this discrepancy is not known, and we have to leave this point to future research.

The secondary branch formation which starts in SCN at a distance of three tip radii behind the tip is delayed up to about seven radii in PVA. This is quite consistent with the recent calculations discussed in Section 10.5.4. The ratio of initial secondary arm spacing λ_2 over tip radius R is also indicated in Table 10-1.

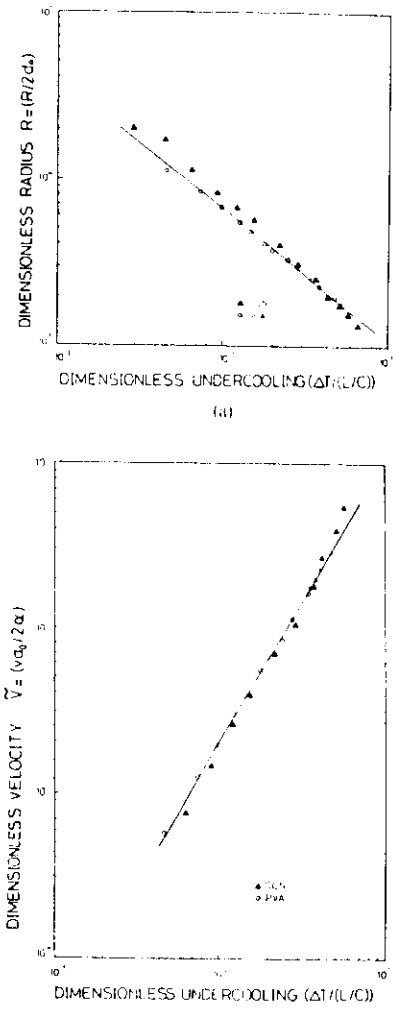

Figure 10-16. Effect of undercooling on (a) tip radius and (b) growth rate of the two organic materials shown in Fig. 10-15 ($\alpha = D$). The experimental results superimpose as they are plotted with respect to dimensionless parameters (Glicksman and Singh, 1989).

Table 10-1. Experimentally determined dendrite tip quantities.

System	Growth type	σ^*	$R^2 V$ [μm^3/s]	$\lambda_2 R$	α	Reference
Thermal dendrites	*Pure*					
Succinonitrile (SCN)	Free	0.0195		3	0.005	Huang and Glicksman, 1981
Pivalic acid (PVA)	Free	0.022		7	0.05	Glicksman and Singh, 1986, 1989
Cyclohexanol	Free	0.027				Singh and Glicksman, 1989
Solutal dendrites	*Alloy*					
NH_4Br - 49 wt.% H_2O	Free	0.081 ± 0.02	18 ± 3	5.2	0.016 ± 0.004	Dougherty and Gollub, 1988
SCN - 1.3 wt.% ACE	Directional	0.032*	1300	2.1 ± 0.2		Esaka and Kurz, 1985
SCN - 4 wt.% ACE	Directional	0.037*	441 ± 30	2.2 ± 0.3		Somboonsuk et al., 1984
CBr_4 - 7.9 wt.% C_2Cl_6	Directional	0.044*	978 ± 8	3.18		Seetharaman et al., 1989
C_2Cl_6 - 89.5 wt.% CBr_4	Directional	0.038*	124 ± 13	3.47		Seetharaman et al., 1989
Thermal and solutal dendrites	*Alloy*					
SCN-ACE	Free	See reference				Chopra et al., 1988
SCN-argon	Free	See reference				Chopra et al., 1988
PVA - 1 wt.% ethanol	Free	0.05 ± 0.02		6 ± 1	0.006 ± 0.002	Dougherty, 1990
PVA - 2.4 vol.% ethanol	Free	0.032 ± 0.006	35	6.8		Bouissou et al., 1989

* Due to differences in the definitions of σ^* these values, as given in the corresponding literature, are smaller by a factor 2 with respect to the values used by Dougherty and Gollub (1988) and defined in this paper. The values given here have been obtained by multiplying the original data by a factor of 2 in order to compare with the same (one-sided) model. (See also Fig. 10-10.)

Free alloy growth
(thermal and solutal dendrites)

In the free dendritic growth of alloys, an interesting observation has been made by various authors. For constant undercooling, the growth rate first increases when small amounts of a second substance are added to a pure material, then reaches a maximum, and finally drops and converges with the pure solutal case. Early experiments in this area by Fujioka and Lindemeyer were first successfully analyzed by Langer (1980c). Fig. 10-17 shows some results on SCN-ACE alloys from Chopra et al. (1988). The increase in V is accompanied by a decrease in the tip radius, which sharpens due to the effect of solute. The experimental findings can be compared to two models: Karma and Langer (1984) (broken line) and Lipton et al. (1987) (full line). Both models provide at least qualitatively good predictions of the observed behavior. In their more recent calculations, Ben Amar and Pelce (1989) concluded that the simple model by Lipton et al. (1987) is consistent with their more rigorous approach.

Table 10-1 gives a summary of representative results of in situ experiments concerning the dendrite tip.

Large undercoolings

Interesting experiments have also been performed with pure and alloyed systems under large driving forces, which reach values of more than half a unit undercooling (for example by Wu et al., 1987; Willnecker et al., 1989). In Fig. 10-18, some of those are reproduced together with predictions from theory (with $\sigma(a) = 0.025$) and including interface attachment kinetics (Trivedi et al., 1987). Up to undercoolings of 200 K, there is reasonable agreement between experiment and theory (interrupted line). At higher undercoolings, other phenomena which are not yet well understood take over.

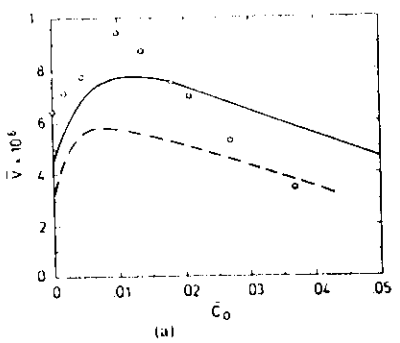

Figure 10-17. Effect of dimensionless composition at constant undercooling of 0.5 K (2.4% of unit undercooling) on (a) dimensionless growth rate and (b) on dimensionless tip radius for free dendritic growth in SCN-acetone alloys (Lipton et al., 1987). Points: experiments (Chopra et al., 1988); solid line: LGK model (Lipton et al., 1987); interrupted line: Karma and Langer (1984) model.

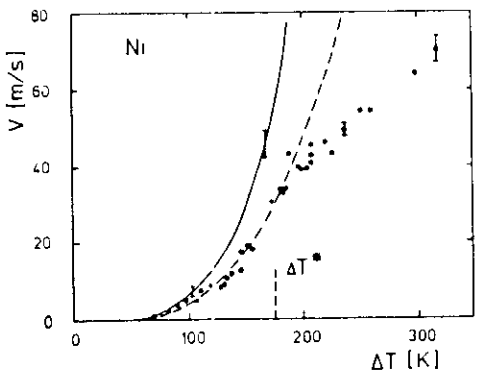

Figure 10-18. Growth rate of free dendrites in highly undercooled nickel (Willnecker et al., 1989). Points: experiments; solid and interrupted line: LKT model (Lipton et al., 1987), without and with attachment kinetics, respectively.

10.5 Directional Solidification

Directional solidification is the most frequent way in which a material changes its state from solid to liquid. The necessary removal of the latent heat of freezing usually occurs in a direction prescribed by the location of heat sinks: For a freezing lake, it is the cold atmosphere above it, in casting iron in a foundry, it is the cold sand mold, into which the heat flow is directed.

At first, it may seem surprising to think that anything interesting should happen at the solid-liquid interface during this process. In contrast to the situation described earlier in Sections 10.4 and 10.2.4, the solid in a casting process is cold and the liquid is hot, so that one would expect the interface to be stable against perturbations.

However, so far we have just considered the solidification of a one-component material, while in reality a mixture of materials is almost always present, even if one of the components may be rather dilute. If, therefore, we assume that material diffusion is the rate-determining (slow) mechanism, while heat diffusion is much faster, the origin of a destabilization of the flat interface can be easily understood on a qualitative basis. We may consider one of the two components of the liquid as an "impurity", which, instead of being fully incorporated into the solid, is rejected at the interface. Such excess impurities have to be diffused away into the liquid in much the same way as latent heat has to be carried away in the case of a pure material as a rate-determining mechanism. Accordingly, precisely the same destabilization and subsequent formation of ripples and dendrites should occur.

Based on these qualitative arguments one can expect the following modification of the Mullins-Sekerka instability (Section 10.2.4) to occur in the present situation of directional solidification. The diffusion of material together with capillary effects produces a spectrum for the growth rates or the decay rates similar to Eq. (10-50), while the temperature field acts as a stabilizer, independent of the curvature of the interface, when a constant term (independent of V) inside the brackets of Eq. (10-50) is subtracted. At small speeds of solidification, the flat interface is stable; above a critical speed, it becomes unstable against the formation of ripples, cells, and dendrites.

In the next section, a few thermodynamic questions related to interface properties in two-component systems are considered, before describing patterns in directional solidification.

10.5.1 Thermodynamics of Two-Component Systems

There is a vast amount of literature available on the thermodynamics of solidification and on multi-component systems (for example Callen, 1960; Baker and Cahn, 1971). Despite this fact, to further the clarity of presentation, we would like to at least sketch the tools which may be used to generalize some approximations which will be made in the next sections.

The fundamental law of thermodynamics defines entropy as a total differential in relation to energy and work:

$$\mathrm{d}U = T\,\mathrm{d}S - P\,\mathrm{d}V + \sum_i \mu_i\,\mathrm{d}N_i \qquad (10\text{-}89)$$

with energy U, entropy S, volume V, pressure P, particle numbers N_i for each species and chemical potential μ_i. The energy is a homogeneous function of the extensive variables

$$U(bS, bV, bN_i, \ldots) = bU(S, V, N_i, \ldots) \qquad (10\text{-}90)$$

with an arbitrary scale parameter $b > 0$.

With the differentiation rule $\mathrm{d}(XY) = X\,\mathrm{d}Y + Y\,\mathrm{d}X$, other thermodynamic potentials $\tilde{U}$ are obtained from U by Legendre transforms

$$\tilde{U} = U - \sum_j X_j Y_j \qquad (10\text{-}91)$$

where X_j are some extensive variables, and Y_j the corresponding intensive variables. The Helmholtz free energy F, accordingly, is

$$F(T, V, N_i, \ldots) = U - TS;$$
$$\mathrm{d}F = -S\,\mathrm{d}T - P\,\mathrm{d}V + \sum_i \mu_i\,\mathrm{d}N_i \qquad (10\text{-}92)$$

and the often used Gibbs free energy G is

$$G(T, P, N_i, \ldots) = U - TS + PV = \sum_i \mu_i N_i;$$
$$\mathrm{d}G = -S\,\mathrm{d}T + V\,\mathrm{d}P + \sum_i \mu_i\,\mathrm{d}N_i \qquad (10\text{-}93)$$

At atmospheric pressure in metallurgical applications, the differences between F and G often can even be neglected, but generally the Gibbs free energy, Eq. (10-93), is most frequently used. It follows immediately that the chemical potentials μ_i are defined as

$$\left(\frac{\partial G}{\partial N_i}\right)_{T,P} = \mu_i \qquad (10\text{-}94)$$

The thermodynamic equilibrium for a system is defined by the minimum of the respective thermodynamic potential with respect to all unconstrained internal parameters of the system. If the system consists of two subsystems α and β in contact with each other, then in thermal equilibrium the temperatures, pressures, and the chemical potentials for each particle type i must be equal:

$$T_\alpha = T_\beta,\ P_\alpha = P_\beta,\ \mu_{i,\alpha} = \mu_{i,\beta} \qquad (10\text{-}95)$$

For the case under consideration we have a solid phase α (with assumed low concentration of B atoms) and a liquid phase β (with higher concentration of B atoms). For simplicity, we further assume that the atomic volumes of both species are the same and unchanged under the solid-liquid transformation.

For a system with a curved interface between a solid and a liquid of different compositions, the chemical potentials can be calculated as follows. Assuming that N_A particles of solvent and N_B particles of solute are given, there will be an unknown number of N_S particles in the solid and N_L particles in the liquid, whose composition is still undetermined. Define the number n as the number of B particles in the solid. Keeping N_S and n initially fixed, the Gibbs potential is obtained as

$$G(N_A, N_B, N_S, n) = N_S\,g_S(C_S) + N_L\,g_L(C_L) + 4\pi R^2\gamma \qquad (10\text{-}96)$$

where γ is the surface-free-energy density, R is the radius of the solid sphere $N_S = \frac{4}{3}\pi R^3$ (unit atomic volume), and g_S and g_L are free-energy densities for homogeneous solids or liquids at concentrations C_S and C_L. Removing the constraints on N_S and n, we obtain thermodynamic equilibrium by minimizing G with respect to N_S and n, so that $G = G(N_A, N_B)$. Together with the chemical potentials from Eq. (10-94), this gives

$$\mu - \mu_0 = -\frac{\gamma}{(C_L^0 - C_S^0)}K \qquad (10\text{-}97)$$

with curvature $K = 2/R$ and $\mu = \mu_B - \mu_A$ being the difference in chemical potentials between solute and solvent. The values μ_0, C_L^0, C_S^0 correspond to equilibrium at $\gamma = 0$ as a reference, around which $g(C)$ was linearized. Here γ was assumed to be independent of curvature and concentrations, but this can easily be incorporated (for effects of surface segregation, for example).

This equation is the boundary condition for the chemical potential on the surface of a solid sphere of surface tension γ coexisting with a surrounding liquid of higher

concentration C_L of B atoms. From a practical point of view, the formulation in terms of chemical potentials does not look very convenient, as they are not directly measurable. From a theoretical point of view, this has advantages, as the chemical potential is the generalized force controlling matter flow and phase changes. In particular, the spatial continuity of chemical potentials together with continuous temperature and pressure guarantees local thermal equilibrium, which we will assume to hold in most of the following discussions.

We now come to the discussion of a typical phase diagram for a two-component system (Fig. 10-19). The vertical axis denotes the temperature, the horizontal axis, the relative concentration of "solute" in a "solvent", or, more generally, B atoms relative to A atoms.

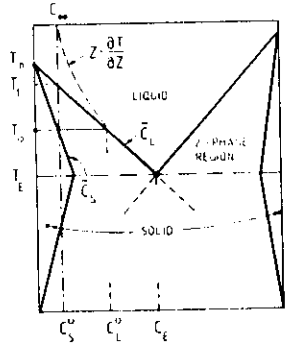

Figure 10-19. Typical solid-liquid phase diagram for a two-component system with the possibility of eutectic growth. $\tilde{C}_L$, $\tilde{C}_S$ are the liquidus and solidus lines with a solid-liquid two-phase region in between. For a relatively low concentration C_∞ of solute in the liquid, a single solid phase at the same composition $C_S^0 = C_\infty$ can show stationary growth. In directional solidification, a positive temperature gradient $\partial T/\partial z$ is assumed to be given perpendicular to the solid-liquid interface and to advance in $+z$-direction. The advancing interface chooses its position to be at temperature T_0, the concentration in the liquid at the interface is then at C_L^0. Ahead of the interface ($z = 0$), the concentration profile $C(z)$ decays towards C_∞ at $z = \infty$ (dashed curve). As long as $C(z) > \tilde{C}_L(T(z))$ with $T(z) = T_0 + z\partial T/\partial z$, a flat interface remains stable.

At high temperatures, $T > T_0$, the system is liquid, regardless of concentration. Assuming a concentration C_∞ to be given initially, we lower the temperature until T_1. At this temperature, we first hit the liquidus line $\tilde{C}_L(T)$, and the system begins to solidify, producing a solid of very low concentration marked by the solidus line $\tilde{C}_S(T)$. When the temperature is slowly lowered, solidification becomes complete at T_0. At lower temperatures, the whole system becomes solid.

The region between $\tilde{C}_S(T)$ and $\tilde{C}_L(T)$ is the two-phase region: If we prepare a system at a concentration between C_S^0 and C_L^0 at high temperatures and then quickly quench it to T_0, the system starts to separate into a solid phase of concentration C_S^0 and a liquid phase of C_L^0. In practice, this is a very slow process, with lengths varying with time t approximately as $t^{1/3}$ (Lifshitz and Slyozov, 1961; Wagner, 1961; Kawasaki, 1990).

In the case of directional solidification, a thermal gradient in the system defines a direction such that the liquid is hot and the solid is cold. A flat interface may then be present at a position in space at temperature T_0. For equilibrium between solid and liquid at that temperature, the concentration in the solid must be at $C_S^0 = C_\infty$, and in the liquid at $C_L^0 = \tilde{C}_L(T_0)$. We now assume that the liquid at infinity has concentration C_∞. Clearly there must be a decrease in concentration as one proceeds from the interface into the liquid. In order to maintain such an inhomogeneous concentration, the interface must move toward the liquid.

In other words, when the liquid of composition C_L^0 freezes, the solid will only have a concentration C_S^0. The difference in concentrations

$$\Delta C = C_L^0 - C_S^0 \tag{10-98}$$

is not incorporated but is pushed forward by the advancing interface and must be carried away through diffusion into the liquid. This is equivalent to the latent heat generated by a pure freezing solid, discussed in Section 10.2.3. Therefore, we expect a spatial concentration profile ahead of the interface which decays exponentially from C_L^0 at the interface to C_∞ far away from the interface. But why should it decay to C_∞ (or: why should the interface choose a temperature position, such that $C_S^0 = C_\infty$)?

The answer is quite simple, and again was given in similar form in Section 10.2.3, Eq. (10-33) for the pure thermal case: If C_S^0 were not identical to C_∞, then during the solidification process there would be either a total increase (or decrease) of concentration – which clearly is impossible – or at least the concentration profile could not be stationary.

This is a rather strict condition, which we can reformulate as follows: If we impose a fixed temperature gradient $\partial T/\partial z$ and move this at fixed speed V_0 over a system of concentration C_∞ at infinity in the liquid (toward the liquid in the positive z-direction), then the interface will choose a position such that its temperature is at T_0, the concentration in the solid will be C_S^0 (averaged parallel to the interface), and the liquid concentration at a flat interface will be at C_L^0. This follows from global conservation of matter together with the imposed stationary solidification rate.

As a final point, we even can derive a condition for the stability of the interface. The concentration profile in the liquid will decay exponentially with distance z away from the interface as

$$C_L(z) = (C_L^0 - C_\infty)\, e^{-z/l} + C_\infty \tag{10-99}$$

by analogy to Eq. (10-32). Since we assume the temperature gradient

$$G_T = \partial T/\partial z > 0 \tag{10-100}$$

to be fixed, the temperature varies linearly with distance z from the interface. This may be written by $G_T = (T - T_0)/z$ as

$$C_L(T) = (C_L^0 - C_\infty)\, e^{-z(T - T_0)/(lG_T)} + C_\infty \tag{10-101}$$

and incorporated into Fig. 10-19 as a dash-dotted line. Note that the diffusion length l is again defined as $l = 2D/V_0$, with D being the diffusion constant of solute atoms in the solvent, and V_0 the interface velocity imposed by the advancement rate of the temperature gradient.

From Eq. (10-101), it is obvious that the dashed-dotted concentration line in Fig. 10-19 converges very quickly to C_∞ for large solidification speeds V_0. As long as that concentration line is fully in the liquid region of the phase diagram, nothing specific happens. But if the dash-dotted line partly goes through the two-phase region between $\tilde{C}_S(T)$ and $\tilde{C}_L(T)$, the liquid in front of the interface is supercooled! This bears the possibility of an instability of the solid-liquid interface, which is completely analogous to the discussion in Section 10.2.4.

A sufficient condition for stability of the interface in directional solidification is therefore

$$\Delta C \frac{V}{DG_T} < \left| \frac{d\tilde{C}_L}{dT} \right| \tag{10-102}$$

so that the dash-dotted curve remains outside the two-phase region (Mullins and Sekerka, 1963; Langer, 1980a). Here we have assumed that material diffusion in the solid can be ignored. As it turns out, in practical situations, violation of this condition typically means "instability" of the interface, so that cellular or dendritic pat-

terns are formed. The reason for this latter conclusion is that the effect of stabilization due to capillarity (or surface tension) is rather weak for typical experiments at threshold.

In summary, in this section we have derived both the boundary condition – in terms of chemical potential – for a curved interface and a basic criterion for interface stability during directional solidification.

10.5.2 Scaled Model Equations

A theoretical analysis of practical situations of directional solidification suffers – among other problems – from the many relevant parameters entering the description. The usual way to proceed in such cases is to scale out as many parameters as possible, writing the problem in dimensionless variables. We have done this already in the discussion of free dendritic growth by introducing the dimensionless diffusion field u; in hydrodynamic applications, it is common practice to use Reynolds and Rayleigh numbers (Chandrasekhar, 1961).

For our present problem, we will proceed in an analogous way. The first step is to express all experimental parameters (wherever possible) in length units (i.e., diffusion length, capillary length, etc.). For presenting results, we divide these lengths by the thermal length introduced below, as this is a macroscopic length which will approximately set the scale at the onset of the instability.

Directional solidification involves chemical diffusion of material together with heat diffusion. As heat diffusion usually is faster by several orders of magnitude, one may often assume constant temperature gradients to exist in the liquid and in the solid. Furthermore, we will also assume that there are equal thermal diffusivities in liquid and solid, which is often the case within a few percent, but this has to be checked for concrete applications. The diffusion field to be treated dynamically then corresponds to the chemical concentration.

It is clear from the discussion in the previous section that for a flat interface moving at constant speed there is a concentration jump $\Delta C = C_L^0 - C_S^0$ across the interface, while asymptotically in the liquid and in the solid, the term C_∞ is approached because of the condition of stationary movement together with the global conservation of matter. We therefore normalize the diffusion field in the liquid to

$$u_L = \frac{C(\text{Liquid}) - C_\infty}{\Delta C} \tag{10-103}$$

so that it varies from one to zero in the positive z-direction from the interface at $z = 0$ to $z = \infty$. If the interface is not at position $z = 0$ but at ζ, we must require $u_L = 1 - \zeta/l_T$, because at a distance

$$l_T = \frac{\Delta C}{G_T} \left| \frac{dT}{d\tilde{C}_L} \right| \tag{10-104}$$

the liquidus concentration has reached the asymptotic value. This is the thermal length which we assume to be fixed by the thermal gradient G_T, the concentration jump ΔC, and the liquidus line $\tilde{C}(T)$, which is here assumed to be a straight line in the T vs. C diagram.

The equation of motion in quasistationary approximation then becomes in analogy to Eq. (10-52) with $l = 2D_L/V$

$$\frac{1}{D_L} \partial_t u_L \approx 0 = \nabla^2 u_L + \frac{2}{l} \frac{\partial u_L}{\partial z} \tag{10-105}$$

This equation applies equivalently to the solid but with a different chemical diffusion length l' due to different chemical diffusion constants. The boundary condition in analogy to Eq. (10-84) obviously becomes

$$u_I(\zeta) = 1 - d_0 K - \zeta(x,t)/l_T - \beta V_\perp \tag{10-106}$$

where we now have $d_0 = l$ as the first term on the r.h.s., with curvature K being positive for the tip of a solid nose pointing into the liquid. The capillary length d is discussed below and interface kinetics with $\beta \neq 0$ will be discussed in Section 10.5.4. The solid boundary condition is simply

$$u_S = k(u_L - 1) \tag{10-107}$$

with segregation coefficient k (equilibrium value assumed) defined as

$$k = \left| \frac{dT}{d\tilde{C}_L} \right| \Big/ \left| \frac{dT}{d\tilde{C}_S} \right| \tag{10-108}$$

through the slopes of the liquidus and solidus line. When they intersect at $\{T_m, C = 0\}$ this is equivalent to the conventional definition $k = C_S/C_L$, but in the above formulation, $k = 1$ may also be true for a constant jump in concentrations, independent of temperature.

The conservation law at the interface $z = \zeta$ finally becomes

$$V_\perp \{1 + (1-k)(u_L - 1)\} = -D_L \hat{n} \nabla u_L + D_S \hat{n} \nabla u_S \tag{10-109}$$

where $V_\perp$ is the interface velocity in direction $\hat{n}$ normal to the interface. For $k = 1$, the brackets $\{\ldots\}$ give 1 corresponding to a constant concentration jump while for $k = 0$, they give u_L, since for a solid in Eq. (10-107), $u_S = 0$.

This standard model for directional solidification (Saito et al., 1989) therefore consists of Eqs. (10-103) to (10-109) together with an additional diffusion equation as Eq. (10-105) inside the solid phase.

The open point is finally the relation of the capillary length d (Eq. (10-106)) with experimentally measurable material parameters. As a first step, we interpret the u-field, Eq. (10-103), as a scaled form of the chemical potential μ (see Section 10.5.1) near T_0

$$u_L = \frac{\mu - \mu_\infty}{\Delta\tilde{C}(\partial\mu/\partial\tilde{C}_L)} \tag{10-110}$$

assuming that linearizing μ around its equilibrium value at the liquidus line $\tilde{C}_L(T_0)$ is sufficient to describe its dependence upon C. By the definitions in Eq. (10-97) together with Eq. (10-106), one now obtains the capillary length in the form given in Eq. (10-82) for the chemical case. Here we have generalized to anisotropic γ as derived in Eq. (10-21). It can finally be related to measurable quantities using the Clausius-Clapeyron equation for the latent heat L_m of freezing of a solution at T_m

$$L_m = -T_m \Delta C (d\mu/dT)_{\text{coex}} \tag{10-111}$$

$(d\mu/dT)_{\text{coex}}$ is the slope of the coexistence line when μ is plotted against T. Together with

$$\left(\frac{d\mu}{dT}\right)_{\text{coex}} = \left(\frac{\partial\mu}{\partial C}\right) \frac{d\tilde{C}_L}{dT} + \frac{\partial\mu}{\partial T} \tag{10-112}$$

this gives for the chemical capillary length, d, in the limit of small ΔC

$$d = [\gamma + \gamma''(\vartheta)] \frac{T_m}{\Delta C L_m |\partial T/\partial \tilde{C}_L|} \tag{10-113}$$

Certain approximations used here such as the linearization involved in Eq. (10-110) or neglecting of $\partial\mu/\partial T$ in Eq. (10-113), may not be safe for the case of a large segregation coefficient $k \approx 1$ or when ΔC is large (Langer, 1980a). In most practical applications, however, this is a small source of error in comparison with other experimental uncertainties. Furthermore, the concentration jump ΔC in Eq. (10-113) is kept fixed, while in reality it should correspond to the temperature-dependent difference in concentration between the liquidus and solidus line. Both for small and large growth rates, however, this only gives a minor correction, and we will ignore its effect in order to facilitate comparison with free dendritic growth.

In summary, with this model we now have all the ingredients to discuss some basic features of directional solidification by analytical and numerical tools. The presentation in the scaled form may not seem at first to be the most convenient means for direct comparison with experiments. Its great advantage over an explicit incorporation of all parameters is that qualitatively different behavior always corresponds to different ratios of length scales or time scales rather than some differences in absolute measures, and, consequently, this presentation allows for a more intuitive formulation of results.

10.5.3 Cellular Growth

A plane interface between the solid phase and the liquid phase of a two-component system tries to locate its position in a thermal gradient so that the chemical potentials of both components are continuous across the interface. Under stationary growth conditions, that position corresponds to a temperature, such that the concentration in the solid (solidus line of the phase diagram) is equal to the concentration in the distant liquid. This growth mode persists for velocities up to a critical velocity, above which the interface undergoes a Mullins-Sekerka instability toward cellular structures. A necessary condition for this instability to occur follows from Eq. (10-102), which can be written in chemical diffusion length $l = 2D/V$ and thermal diffusion length l_T, Eq. (10-104), as

$$l/l_T \lesssim 2 \tag{10-114}$$

The 2 comes from the specific definition of l, and the inequality for instability is only approximate because small effects of surface tension have not been considered yet here. Incorporation of surface tension reveals that the instability first occurs for a critical wavelength λ_c larger than the stability length $\lambda_c = 2\pi\sqrt{d_0 l}$. Slightly above the critical pulling speed V_c, the interface makes periodic structures of finite amplitude. This was analyzed by Wollkind and Segel (1970), and for other specific cases, by Langer and Turski (1977). A more general treatment was given by Caroli et al. (1982).

The result of these investigations is that in a diagram of pulling speed V versus wavelength λ there exists a closed curve of neutral stability, Fig. 10-20. At fixed V, a small amplitude perturbation of the interface at a wavelength on that curve neither grows nor decays. Perturbations at wavelengths outside that curve decay, inside the curve they grow to some finite amplitude. This is similar to periodic roll patterns in the Rayleigh-Benard system of a fluid heated from below (Chandrasekhar, 1961), but here a maximal speed, V_a, is present, above which a flat interface is absolutely stable. For normal alloys, this speed is very high, while for liquid crystals, it is more easily accessible in controlled experiments

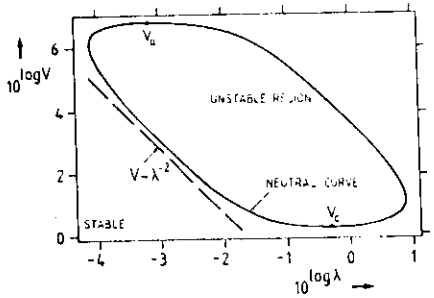

Figure 10-20. Neutral stability curve for a flat solid-liquid interface in directional solidification (schematic). The dependence of the growth rate (pulling speed) V on the wavelength λ of the interface-perturbation is approximately $V \sim \lambda^{-2}$, both for the short and long wavelength part of the neutral stability curve. V_c and V_a are the lower critical velocity and upper limit of absolute stability, respectively.

(Bechhoefer et al., 1989). The diffusion length at V_a is of the order of the capillary length.

At low speeds, but slightly above the critical velocity, V_c sinusoidal "cells" will be formed for systems with segregation coefficients k near unity. For small segregation coefficients, however, the neutral curve does not define such a normal bifurcation but rather an inverse bifurcation. This means that immediately above V_c large amplitude cells with deep grooves are formed. A time sequence of the evolution of a sinusoidal perturbation into elongated cells at 1% above V_c due to inverse bifurcation is shown in Fig. 10-21. This can be understood theoretically (Wollkind and Segel, 1970; Langer and Turski, 1977; Caroli et al., 1982) by means of an amplitude equation valid near V_c:

$$\frac{\partial A}{\partial t} = \left(\frac{V - V_c}{V_c}\right) A - a_1 |A|^2 A + \dots \tag{10-115}$$

where A is the (possibly complex) amplitude of a periodic structure $\exp(ikx)$ with $k = 2\pi/l_c$. The coefficient a_1 is called the Landau-coefficient. If it is positive, we have a normal bifurcation with $|A| \sim \sqrt{V - V_c}$, while for $a_1 < 0$, the third order term does not stabilize the pattern but allows very large amplitudes leading to elongated cells Fig. 10-21, which will be stabilized by some higher-order effects.

A second phenomenon is usually associated with this inverse bifurcation, namely, the splitting of the wavelength $\lambda_c \to \lambda_c/2$. Qualitatively, this is understandable from nonlinear corrections since the squaring of the original pattern $\sim \exp(ikx)$ produces terms $\sim \exp(i2kx)$. This effect has clearly been observed in experiments (de Cheveigne et al., 1986).

We will discuss some aspects of the very high speed region in Section 10.5.7 but devote the main part of the following discussions to the most interesting region for practical purposes, which is not too close to the upper and lower bounds of the growth rate V_a and V_c.

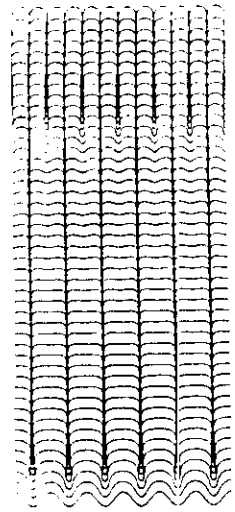

Figure 10-21. Time evolution of an interface from sinusoidal to cellular structure slightly above the critical threshold V_c for the case of inverse bifurcation. A secondary instability quickly leads to a halving of the wavelength.

Approximating by straight lines the neutral curve of the logarithmic plot Fig. 10-20 in the intermediate velocity region, one finds for both the small and the large λ-limits the relation

$$V\lambda^2 \approx \text{constant} \tag{10-116}$$

Again we have recovered the form Eq. (10-1) mentioned in the introduction as a scaling law where λ here is the cell spacing. This suggests that the cellular pattern formed in actual experiments would also follow this behavior. Unfortunately, this problem has not yet been settled to a satisfactory degree from a theoretical point of view. This is partly due to the difficulty of

finding good analytical approximations to the cellular structures, which makes numerical calculations necessary to a large degree. We will return to this point in Section 10.5.5.

For small amplitude cells obtainable under normal bifurcation, some progress has recently been made (Brattkus and Misbah, 1990). A phase-diffusion equation has been derived describing the temporal evolution of a pattern without complete periodic variation of the interface. The basic idea is to replace the periodic trial form $\exp(i k x)$ by a form $\exp(i\Theta(x,t))$ so that $q(x,t) = \partial\Theta/\partial x$ is now no longer a constant but is slowly varying in space along the interface and evolving with time. One can derive a nonlinear phase diffusion equation

$$\partial_t q = \partial_x \{\tilde{D}(q)\partial_x q\} \tag{10-117}$$

with a diffusion coefficient $\tilde{D}(q)$ depending in a complicated way on q. The procedure is well known in hydrodynamics and it is associated there with the so-called Eckhaus instability (Eckhaus, 1965). This instability eventually causes an (almost) periodic spatial structure to lose or gain one "period", thereby slightly changing the average wavelength. In directional solidification, the result (Brattkus and Misbah, 1990) is shown in Fig. 10-22, where velocity is plotted against wavenumber in a small interval above the critical velocity. The full line is the neutral curve, the full triangles mark the Eckhaus boundary of phase stability. A periodic (sinusoidal) pattern is stable against phase slips only inside the region surrounded by triangles, thereby allowing for an Eckhaus band of stationary periodic solutions with a substantially reduced spread in wave-numbers as compared to the linear stability results. Note also that the results for phase stability (dashed line) from the amplitude equation only hold in an extremely small region above V_c, while already 20% above V_c, it shows no overlap with the result from the present analysis (triangles). The short-wavelength branch has a very complicated structure, while the long-wavelength branch far from the threshold scales as

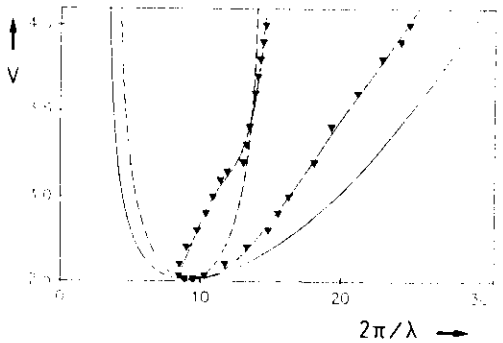

Figure 10-22. Stability diagram V vs. $2\pi/\lambda$ near the lower critical threshold for a flat moving interface in directional solidification. The solid line is the neutral stability curve Fig. 10-20, the dotted curve is the most dangerous mode, the dashed curve is the limit of the Eckhaus stability from the amplitude equation. The triangles mark the Eckhaus limit as obtained from the full nonlinear analysis (Brattkus and Misbah, 1990), with stable cellular interfaces possible only inside that region. The band width of possible wavelengths for cellular interfaces accordingly is smaller by a factor of ≈ 0.4, as compared to the band width given by the neutral (linear) stability curve.

$\lambda_{max} \propto V^{-1/2}$ again like the neutral curve. This also seems to be in agreement with experimentally observed results, as discussed later (Billia et al., 1987, 1989; Somboonsuk et al., 1984; Esaka and Kurz, 1985; Eshelman and Trivedi, 1987; Faivre et al., 1989; Kurowsky, 1990).

At higher velocities, the cells quickly become elongated Fig. 10-23 with deep grooves forming bubbles. This was first obtained through numerical calculations by Ungar and Brown (1984a, b; 1985a, b). Calculations with a dynamical code in quasistationary approximation (Saito et al., 1989) confirmed the stability of these structures with respect to local deformations and short-wavelength perturbations. The long-wavelength Eckhaus stability has not been investigated so far for these cells. All calculations were made in two dimensions which are believed to be appropriate for experiments of directional solidification in a narrow gap between glass plates.

At higher velocities and wavelengths (or cell sizes) not much smaller than the diffusion length, the grooves become very narrow, similar to Fig. 10-21 (Ungar and Brown, 1984, 1985; Karma, 1986; Kessler and Levine, 1989; Mc Fadden and Coriell, 1984; Pelce and Pumir, 1985). If the velocity is fixed and the wavelength λ is reduced significantly below the diffusion length l, one reaches the Saffman-Taylor limit (Brener et al., 1988; Dombre and Hakim, 1987; Kessler and Levine, 1986c), which is equivalent to a low-viscosity fluid being pushed into a channel of width λ filled with a high-viscosity fluid. The low-viscosity fluid forms a finger just like the solid in directional solidification. Near the tip, the width of the finger λ_f corresponds to

$$\lambda_f = \lambda/2$$

with cell spacing λ, where $\Delta < 1$ is the actual supercooling at the tip (remember that

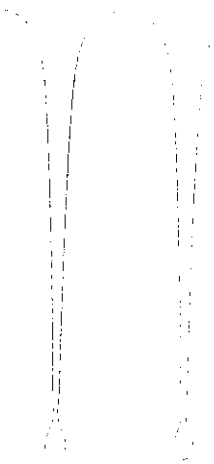

Figure 10-23. Computed example for a deep cellular interface at $V \approx 5 V_c$ with bubble formation at the bottom of the groove (Saito et al., 1990).

$\Delta = 1$ for a flat interface at $\zeta = 0$, and $\Delta = 0$ for a flat interface at $\zeta = l_T$). This serves to verify the consistency of numerical calculations (Saito et al., 1989). An even more detailed analysis was made recently by Mashaal et al. (1990).

For comparison with experiments, it is useful to draw a V vs. λ diagram (Fig. 10-24). Here the full line is again the neutral curve, the broken line is the most dangerous (or most unstable) mode, and the dotted line denotes the relation $l = \lambda$, where the diffusion length is equal to the imposed wavelength. The stars mark some detailed numerical investigations (Saito et al., 1989). The star furthest to the left is close to the above-mentioned Saffmann-Taylor limit. At slightly larger wavelengths where $\lambda < l$ still holds, one is in a scaling region, where the radius of curvature at the tips of the cells is about 1.5 of the cell spacing, as also found experimentally (Kurowsky, 1990). All these considerations give sufficient confidence that the numeri-

cal calculations may provide insight into the mechanism of directional solidification also for the most interesting case of dendritic arrays formed at higher growth rates.

A few words on numerical methods and system parameters may be in order before we discuss the dendritic region. The numerical code is equivalent to the one used for the free dendritic case with the modification that it is necessary to integrate over several cells to arrive safely outside the diffusion length. Furthermore, in principle, diffusion has to be considered in both the liquid and the solid. Since the diffusion coefficient for material in the solid is usually much lower than it is in the liquid, it is found that diffusion in the solid alloy can usually be neglected on time scales for the formation of cells. For long durations, of course, microsegregation takes place, and solid diffusion then becomes important (Kurz and Fisher, 1984).

A more serious difficulty in directional solidification is the large number of parameters defining the system. We will concentrate here on typical parameter values used in experiments performed for some transparent materials between glass plates. Several tests and specific calculations also done for alloys, however, indicate that a large part of the results can be carried over to these more relevant situations from a metallurgical point of view without qualitative changes.

10.5.4 Directional Dendritic Growth

The diagram in Fig. 10-24 showing velocity versus λ in logarithmic form indicates that qualitatively different behavior may be expected depending on whether the diffusion length is larger or smaller than the cell spacing. In the previous section, we discussed the first case. When the diffusion length becomes smaller than the cell spacing we expect that the individual cells become more and more independent of each other, until finally they may behave like individual isolated dendrites.

In order to test this hypothesis, a series of numerical experiments were performed at a fixed cell spacing and increasing pulling velocity (Saito et al., 1989). The numerical parameters of the model were representatively taken to correspond to steel with Cr-Ni ingredients (Lesoult, 1980). In dimensionless units, the critical velocity and wavelength for the plane-front instability were $V_c = 1.136$, $\lambda_c = 0.514$. The anisotropy of the capillarity length was not known and was taken as $\varepsilon = 0.1$ to allow for comparison with the previously mentioned calculations on the free dendritic case. The cellular wavelength was fixed to $\lambda = 0.36$ corresponding to the stars at increasing velocity and constant λ in Fig. 10-24.

At the lowest velocity still below the $l = \lambda$ dividing line, rounded cells were observed; the tip was not well approximated by a parabola. At higher speeds $V = 12$ the parabolic structure of the tip already became visible, Fig. 10-25, and at even higher speeds $V = 20$ the dendritic structure with side branches was fully developed, Fig. 10-26.

We can now compare the resulting tip radius with the predictions from free dendritic growth. Note that in the present case the velocity is fixed rather than the supercooling, so that the dendrite now uses a supercooling corresponding to the given velocity. This means that the tip of the dendrite is no longer at a position in the temperature-gradient field like a flat interface, but has advanced toward the warmer liquid.

Fig. 10-27 contains the ratio of the tip radius divided by the radius from scaling Eq. (10-68) (where the Peclet number P was

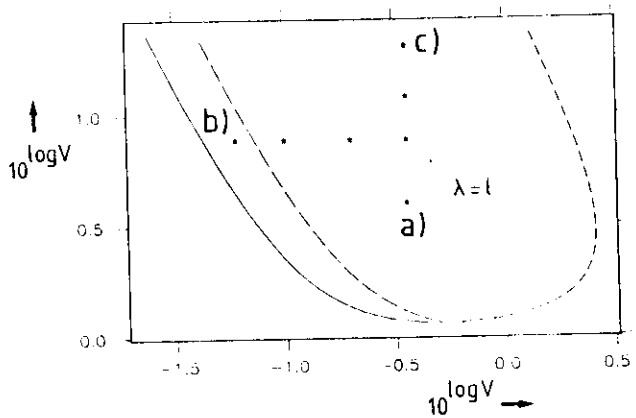

Figure 10-24. "Phase"-diagram $\log(V)$ vs. $\log(\lambda)$ for interface patterns in directional solidification. The solid and dashed curves denote the neutral stability curve, and the dash-dotted curve the most dangerous mode. Stars mark fixed parameter values discussed hereafter. The lower critical threshold here is $V_c \approx 1$, $\lambda_c \approx 0.5$ for velocity and cell spacing. For other parameters see text. At low pulling speeds and large wavelengths cellular patterns with narrow grooves are found (a). At very short wavelengths and moderate speeds cellular patterns with wide grooves are found, consistent with theories for viscous fingering. At high pulling speeds, such that the cell spacing λ is significantly wider than the diffusion length l, side-branching dendritic arrays are formed (c) (Saito et al., 1990). The speeds are still much smaller than the absolute stability limit V_c.

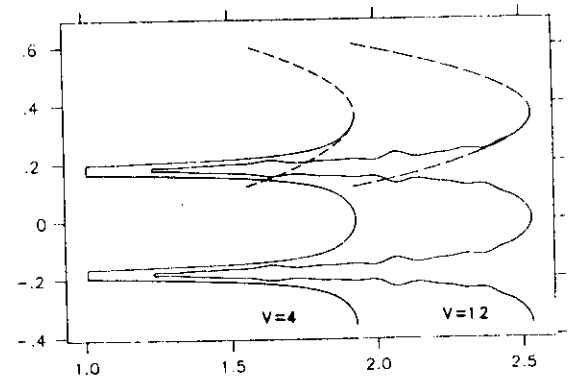

Figure 10-25. Transition from needle-shaped to dendritic cells at increasing pulling speeds. $V = 4$ is below the dotted line in Fig. 10-24, and $V = 12$, above it. Parabolas adjusted to the tip radius are not a good fit to the profiles.

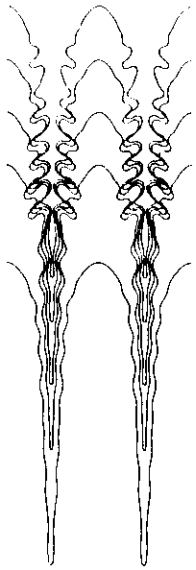

Figure 10-26. Time sequence of a dendritic array at $V = 20$, $\varepsilon = 0.1$, corresponding to point (c) in Fig. 10-24. The starting structure corresponds to $V = 12$, similar to Fig. 10-25. The cellular array quickly converges to a stationary side-branching mode of operation.

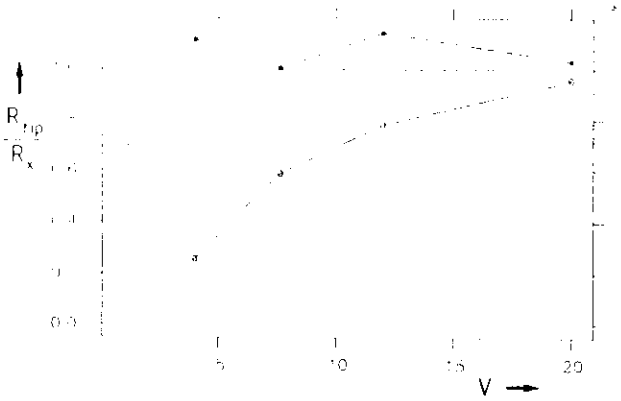

Figure 10-27. Ratios R_{tip}/R_x of tip radius computed numerically (Fig. 10-24) over two theoretical predictions, where R_x is either the Ivantsov radius (circles) or the radius from solvability theory (stars). See also Fig. 10-12. The result is in nearly perfect agreement with the solvability theory down to very small speeds used in the original form as the ratio of tip radius to diffusion length). Furthermore, this figure gives the ratio of the tip radius to the Ivantsov radius, which comes from the Peclet number through the relation for the supercooling at the tip, Eq. (10-56). The data are instantaneous measurements rather than time-averaged measurements. It is obvious from Fig. 10-27 that the scaling relation, Eq. (10-68), holds very well at rather low speeds, where neighboring cells still interact substantially through the diffusion field, while the relation from the Ivantsov formula for the Peclet number only holds at higher velocities. The obvious reason for the latter deviation at small velocities is that the Ivantsov relation represents a global conservation law for an isolated parabolic structure, which is clearly not valid when several cells are within a diffusion length.

The observation that the scaling relation, Eq. (10-68), is very robust obviously has to do with the fact that it results from a solvability condition at the tip of the dendrite, which is only very weakly influenced by deformations further down the shaft.

In the same study, it was also confirmed that the side branches fulfilled precisely the same scaling relation Fig. 10-13 as the free dendrites at relatively low speeds of $V = 12$ shown in Fig. 10-25. In this case, the side branches are just beginning to show up, while the tip is not very noticeably parabolic.

Up to this point these investigations were done at a constant anisotropy of $\varepsilon = 0.1$ of the capillarity length. In Fig. 10-28 the normalized supercooling Δ has been plotted against velocity V, where $\Delta = 1$ for a flat interface at stationary growth. Two sets of data for $\varepsilon = 0.1$ and $\varepsilon = 0.2$ are shown. If one increases the pulling speed above the critical value $V \approx 1$, the supercooling at the tip of the cellular patterns first decreases, because the forward bulges come into a range of higher temperature. At intermediate velocities, Δ goes through a minimum and finally approaches the broken lines corresponding to the scaling relation, Eq. (10-68), together with Ivantsov relation, Eq. (10-56). At intermediate velocities, the supercooling Δ is above the corresponding curve meaning that the Peclet number, and therefore the Ivantsov radius is larger than expected from the free dendritic scaling.

This is in agreement with Fig. 10-27 shown above. The minimum of the Δ versus V relation is in the range where the diffusion length is comparable to the cell spacing, as expected from the diagram Fig. 10-24.

As a final example, Fig. 10-29 shows a dendritic array at the relatively high velocity $V = 40$ at anisotropy $\varepsilon = 0.2$. As in free dendritic growth, the structure appears sharper than the structure in Fig. 10-26 at smaller anisotropy.

The opposite direction of extremely small anisotropies has not yet been analyzed in great detail, and it is rather unclear what happens both from a theoretical and an experimental point of view. Most likely, at zero anisotropy $\varepsilon = 0$, the cells will tend to split if the cell spacing becomes much

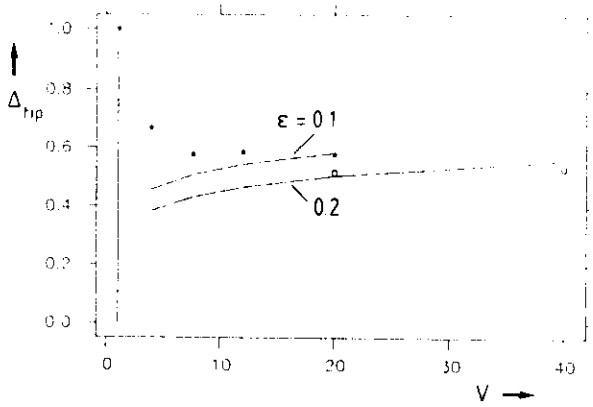

Figure 10-28. Supercooling at the tip of a cell or dendrite vs. pulling speed as obtained from numerical simulation. For a flat interface at small speeds, the global conservation law forces $\Delta = 1$, then it first decreases until $\Delta \approx 2$, and finally approaches the slowly increasing relation $\Delta(V)$ obtained for the free dendritic case (see also Fig. 10-40). The expected dependence on capillary anisotropy ε is also recovered.

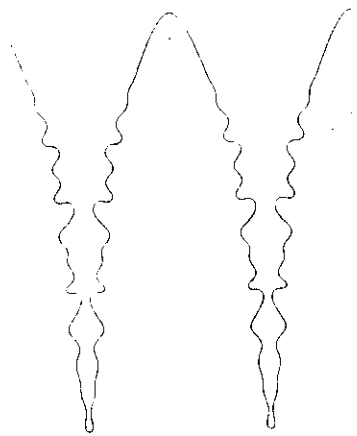

Figure 10-29. Pronounced parabolic directional dendrites at speed $V = 40$ and $\varepsilon = 0.2$, as used in Fig. 10-28. Note that the tip-radius here is about 0.03 and the short-wavelength limit of neutral stability 0.05 in units of the cellular spacing. This is qualitatively consistent with experimental observations of large interdendritic spacings in units of tip radii. Tip splitting was only observed at much lower values of capillary anisotropy.

larger than the diffusion length, which affords the possibility for chaotic dynamics at high speeds. But this is still speculative today.

Let us take a quick look at the kinetic coefficient β in Eq. (10-106). As can be concluded from its multiplication by $V_\perp$, β becomes more and more important at high growth rates. For the free dendritic case with kinetic coefficient β and 4-fold anisotropy β_4 of the kinetic coefficient, a scaling relation similar to Eq. (10-68) was derived by Brener and Melnikov (1990b):

$$\beta V = \sigma_\beta \left(\frac{2 D_L \beta}{d_0}\right)^{9/2} P^{11/2} \beta_4^{7/2} \qquad (10\text{-}118)$$

with a constant prefactor $\sigma_\beta \approx 5$ and with Peclet number P as used before in Eq. (10-68). The scaling relation, Eq. (10-118), consists of several nontrivial power laws; only the one with $P = R/l$ relating tip radius to velocity has been confirmed to date (Classen et al., 1990). With regard to the general agreement between analytical and numerical results obtained so far, however, there is little doubt that these scaling results (and others given by Brener and Melnikov, 1990a) will also hold for the dendritic region $\lambda \gtrsim l$ in directional solidification.

A last point to be kept in mind is that the tip supercooling Δ in directional solidification is not small, as required by the approximations used for the derivation of the scaling relation. On the other hand, $P = 1$ corresponds to a supercooling as large as $\Delta \approx 0.75$; 0.6 for 2-dim and 3-dim, respectively, and the scaling relations can be expected to hold over a large range of velocities, as already indicated from the other free dendritic case, Fig. 10-12.

In summary, these investigations have shown that there appears to be a smooth transition from cellular to dendritic structures. The dendritic growth laws are very well represented by the scaling relations for the free dendritic case. This scaling should hold in the region

$$d_0 < R \approx l < \lambda < l_T \qquad (10\text{-}119)$$

where λ is the primary cell-spacing. It was recently proposed (Karma and Pelce, 1989) that the transition from cells to dendrites could occur via an oscillatory instability, for which the present investigations under quasistationary approximation have shown no evidence. A fully time-dependent calculation is possible in principle with Green's function methods (Strain, 1989), and results may appear in the near future.

10.5.5 The Selection Problem of Primary Cell-Spacing

An important question from an engineering point of view appears to be the following: Suppose we know all the material parameters and the experimentally controllable parameters like thermal gradient and pulling speed for a directional solidification process: can we then predict the distance between the cells and dendrites?

A positive answer to this question is desirable because the mechanical properties of the resulting alloy are improved with a decrease in the primary cell spacing (see Kurz and Fisher (1984, 1989) and references therein).

In a rigorous sense the answer today is still negative, but at least arguments can be given for the existence of some boundaries on the wavelengths (or cell spacings) which can be estimated with the use of simplifications.

The situation here shows some similarity to the formation of hydrodynamic periodic roll patterns (Newell and Whitehead, 1969; Kramer et al., 1982; Riecke and Paap, 1986). In a laterally infinite system, a whole band of parallel rolls is present above the threshold for roll formation, the so-called Eckhaus band. This was already mentioned in Section 10.5.3 for directional solidification.

The reason for the stability of these rolls is that an infinitesimal perturbation is not sufficient to create or annihilate a roll, but a perturbation must exceed a threshold value before such an adjustment can occur.

In directional solidification, the situation is different insofar as the envelope over the tips of the cells could make a smooth deformation of very long wavelength, thereby building up enough deformation energy so that a cell could be created or annihilated at isolated points. One indication for such a process is the oscillatory instability of cells postulated recently (Karma and Pelce, 1989), but that point is still controversial (Kessler and Levine, 1990).

The only hard argument for the selection of a unique wavelength comes from a recent analysis of a spatially modulated thermal gradient acting on a cellular pattern of small amplitude (normal bifurcation) which imposes a *ramp* on the pattern (Misbah, 1989; Misbah et al., 1990a). The idea originally proposed for the hydrodynamic case (Kramer et al., 1982) is to have a periodically varying thermal gradient parallel to the interface, which keeps the interface flat in some regions and allows for the formation of cells in between (Fig. 10-30). For such a specific setup it was recently shown (Misbah et al., 1990a) that a unique wavelength must be selected in the center of the small-gradient area. The reason for this special construction is that it allows for the formation of cells at arbitrarily small amplitudes (and therefore small pinning forces) in the region of strong thermal gradient.

In general, however, the boundary conditions on the other sides of the cells, due to the container walls, are not well specified and typically will not provide such a ramp structure (see Misbah (1989), however, for growth in a rotating vessel). For the time being, one therefore can try to a

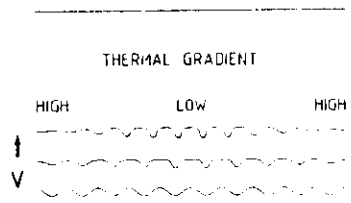

Figure 10-30. Numerical study of cellular wavelength selection at the interface by introducing a ramp in the thermal gradient field. A high thermal gradient on the sides approximately normal to the interface keeps the interface flat, the smaller gradient in the center allows for cells to develop. At fixed ramp profile a unique cell-spacing is selected in the center, starting from different initial conditions (Misbah 1990, unpublished).

least find some boundary similar to the Eckhaus-band for the limits of large and small wavelengths in the cell spacing.

It is not easy to extend the corresponding analysis of small-amplitude cells (Brattkus and Misbah, 1990) to cells with deep grooves, as these essentially infinite grooves present a kind of topological constraint on the number of longitudinal cells in a given lateral interval. The creation or annihilation of cells is therefore likely to be a discrete process.

A natural mechanism for the local reduction of cell spacings (or creation of a new cell) is either a nucleation in one of the grooves (the liquid is supercooled), or even more likely, the formation of a new cell out of a side-branch in such a groove. Alternatively, tip splitting of a cell may give the same result (Fisher and Kurz, 1978, 1980).

The opposite mechanism for the increase of cell spacing (or annihilation of an existing cell) could occur through the competition of neighboring cells for the diffusion field, such that one cell finally moves at a slightly lower speed than the neighboring cells and, consequently, will be supressed relative to the position of the moving front.

These two mechanisms have been conjectured by many authors in the past. Some progress has been made recently by the confirmation of the scaling relations in the dendritic region. It seems, therefore, worthwhile to reformulate those conjectures with the help of these scaling relations. Let us first consider the short-wavelength λ (cell spacing) argument. Assume that we are at dendritic growth speeds, Eq. (10-119), ignoring here kinetic coefficients. The solidification front then looks like an array of individual dendrites which only weakly interact with each other through the diffusion field $l < \lambda$.

The solidification front $\zeta = 0$ will be understood here as a smooth envelope touching all the dendrite tips, so that deformations of the front have a smallest wavelength λ equal to the cell spacing. There are now basically two "forces" acting on deformations $\partial\zeta(x,t)/\partial t$ of that front. If some of the tips are trailing a little behind the others, they will be screened through the diffusion field of the neighboring tips, as in the conventional Mullins-Sekerka instability, but now without a stabilizing surface tension interacting between neighboring tips. Taking this into account, the destabilizing force is $F_d \approx \tilde{\Omega}_k^{(d)} \tilde{\zeta}_k$ with $\tilde{\Omega}_k^{(d)} = V|k|$ for a sinusoidal perturbation of amplitude $\tilde{\zeta}_k$ of a plane interface without surface tension moving at velocity V and wavenumber k. The maximum lies at $k = 2\pi/\lambda$. The actual area under this perturbation $\tilde{\zeta}_k$ contained in the solid *cells* is smaller by a factor $\approx 2R/\lambda$. We thus arrive at a maximal destabilizing force of

$$F_d \approx \Omega^{(d)} \zeta_s; \quad \Omega^{(d)} \approx 4\pi V R/\lambda^2 \qquad (10\text{-}120)$$

corresponding to a depression or enhancement of every second dendrite.

On the other hand, each of these individual dendrites knows its operating point, and through the given velocity its supercooling at the tip. We approximate this by the asymptotic form of Eq. (10-56) $A \approx 1 - P$ since basically the variation of A with P enters below, even though P may not be very large compared to unity. Capillary effects seem to be not very important in this region and are thus neglected here for simplicity. By definition, $A = 1 - z_{tip}/l_T$, and the two expressions for A can be evaluated: $z_{tip} \approx l_T/R$. The stabilizing force $F_s \approx \Omega^{(s)} \zeta_s$ follows from the obvious relation $\Omega^{(s)} = dV_{tip}/dz_{tip}$ as

$$F_s \approx \Omega^{(s)} \zeta_s; \quad \Omega^{(s)} \approx -2\frac{VR}{l_T l} \qquad (10\text{-}121)$$

As expected, the sign of that "force" is opposite to the destabilizing force, Eq. (10-120). Setting the sum of the two equal to zero, we expect an instability to occur first at cell spacings

$$\lambda \lesssim \sim l_T l \qquad (10\text{-}122)$$

for segregation coefficients around one. We cannot say much about small segregation coefficients because the nonlinearity in Eq. (10-109) replacing Eq. (10-56) becomes important there. Of course, a number of rough approximations were used specifically in the treatment of the destabilizing force, but this argument should at least qualitatively capture the competition mechanism between neighboring dendrites. A recent, more detailed analysis (Warren and Langer, 1990) looks quite promising at large velocities in comparison with experiments (Somboonsuk et al., 1984) (see also Kessler and Levine, 1986c; Bechhoefer and Libchaber, 1987).

Let us now look at the large-wavelength limit λ. The initial growth conditions are assumed to be just as before Eq. (10-119), but now at possibly large cell spacings λ. In the numerical calculations, it was found (Saito et al., 1989) that for fixed cell spacings λ at increasing velocity, a *tail instability* occurs (Fig. 10-31). A side branch in the groove between two dendrites splits off a ternary branch, which then moves so fast in the strong supersaturation in the groove that it finally becomes a new primary branch. In the plot, the imposed mirror symmetry is, of course, artificial, but it even acts opposite to this effect, making the process more plausible in reality. In fact, this is also observed experimentally (Esaka and Kurz, 1985), in particular when the solid consists of slightly misaligned regions separated by grain boundaries, so that the growth direction of two neighboring dendrites is slightly divergent. Our basic assumption now is that this tail instability occurs when the intersection of parabolic

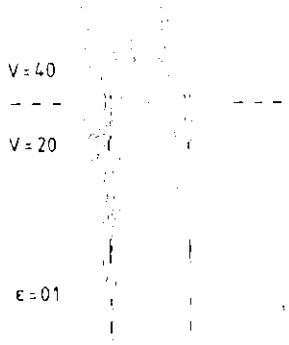

Figure 10-31. After a sudden increase of the growth rate in the dendritic region at fixed cell spacing, tail instability occurs. One of the side branches near the tip produces a protuberance in the forward direction which then becomes a new primary cell (the imposed mirror symmetry is not present in reality of course). In accordance with the stability of dendritic cells against tip splitting (compare Fig. 10-29), this tail instability appears to be an important selection mechanism for primary cell spacing. See also Fig. 10-43.

envelopes over neighboring dendrites occurs at a point $z \lesssim 0$, where, theoretically, $A > 1$. In this case, there is no need for long-range diffusion around a side branch, for its dynamics become local. Of course, this assumption ignores geometrical competition between neighboring side branches to a certain extent, but for the moment there seems to be no better argument to hand.

Taking into account the point that neighboring parabolas with tip position at $z_{tip} > 0$ cannot intersect further down to the cold side than at $z = 0$, we obtain $z_{tip} = l_T l/R$ from the two relations for l just as in the previous case of small wavelengths. But now, we must use the parabolic relation $z_{tip} = \lambda^2/8R$ for the intersection of two parabolas of radius R at $z = 0$, which are at a distance λ apart from each

other. The tail instability accordingly is expected to occur for

$$\lambda \gtrsim \sqrt{l_T l} \tag{10-123}$$

again with a prefactor roughly of the order of unity. In comparison with Eq. (10-122), it can be seen that in both cases the same scaling relation results. The scaling with the inverse growth rate l follows the neutral stability curve at velocities safely in between the two critical values and again recovers Eq. (10-1) by noting that $l \sim V^{-1}$ and therefore $V\lambda^2 \approx$ constant. The results, Eqs. (10-122) and (10-123) seem to be in agreement with experiments (Somboonsuk et al., 1984; Kurowski, 1990; Kurz and Fisher, 1981, 1989) concerning the scaling with respect to diffusion length l and thermal length l_T. The limit $k \to 0$ for the segregation coefficient as a singular point is not reliably tractable here.

The previously given relation $\lambda \sim l^{1/4}$ (Hunt, 1979; Trivedi, 1980; Kurz and Fisher, 1981) seems to be valid in an intermediate velocity region (Fig. 10-28) where λ does not vary significantly, so that $\lambda_{\text{tip}}/l_T \approx 1/2$. (See also Section 10.6.1.)

A serious point is the neglecting of surface tension and anisotropy in these derivations. In the experiments analyzed so far the relation $V\lambda^2 \approx$ const. seems to hold approximately, but what happens for the capillary anisotropy ε going to zero? Numerically, tip splitting occurs at lower velocities for smaller ε. In a system with anisotropy $\varepsilon = 0$ (and zero kinetic coefficient) the structures most likely show chaotic dynamics at velocities where the diffusion length l is smaller than the short wavelength limit of the neutral stability curve Fig. 10-24, but this is still rather speculative (Kessler and Levine, 1986c).

In considering whether the tail instability (large λ) or the competition mechanism (small λ) will dominate in casting processes, we tend to favor the former. If the solidification front consists of groups of dendrites slightly misoriented against each other due to small-angle grain boundaries, cells will disappear at points where the local growth directions are converging and new cells will appear through the tail instability at diverging points at the front.

To summarize, the most likely scaling behavior of the primary cell spacing λ, depending on pulling velocities, follows Eqs. (10-1) and (10-123) as a consequence of the arguments presented in this section. This conclusion is supported by a number of recent experiments (Billia et al., 1987; Somboonsuk et al., 1984; Kurowsky, 1990; Esaka and Kurz, 1985), but more work remains to be done.

10.5.6 Experimental Results on Directional Dendritic Growth

Since 1950, in situ experiments on directional solidification (DS) of transparent model systems have been performed (Kofler, 1950). However, it took some time until such experiments were specifically conceived to support microstructural models developed in the 1950s and early 1960s. The work of Jackson and Hunt (1966) is a milestone in this respect (Hunt et al., 1966). Their experimental approach on dendritic growth has been developed further by several groups: Esaka and Kurz (1985), Trivedi (1984), Somboonsuk et al. (1984), Somboonsuk and Trivedi, (1985), Eshelman et al. (1988), Seetharaman and Trivedi (1988), Seetharaman et al. (1988), de Cheveigne et al. (1986), and others. Substantial progress has been made during these years. This research is still producing interesting new insights into the dynamics of interface propagation during crystallization.

The specific interest of DS is that growth morphologies can be studied not only for dendritic growth but also for cellular and plane front growth. We will discuss these phenomena in the sequence of their appearance when the growth rate is increased from V_c, the limit of first formation of Mullins-Sekerka (MS) instabilities (also called limit of constitutional undercooling), to rates where plane front growth again appears at velocities above V_a, the absolute stability limit.

Morphological instabilities. The onset of plane front interface instability is observed to start at defects like grain boundaries, subgrain boundaries, and dislocations, forming a more or less pronounced depression at the intersection with the solid-liquid boundary as shown in Fig. 10-32 (Fisher and Kurz, 1978). It is inherently difficult to quantitatively observe the breakdown because the growth rates are small, and a long period of time is required to reach steady state.

The amplitude and wavelength of the perturbations as a function of V developing in systems with small distribution coefficients k (of the order of 0.1) are shown in Fig. 10-33. In CBr_4-Br_2 (de Cheveigne et al., 1986) and SCN-ACE (Eshelman and Trivedi, 1987), the bifurcation is of a subcritical type, i.e., there are two critical growth rates, one for increasing growth rate, V_c^+, and another lower value for decreasing growth rate, V_c^-. Therefore, a periodic interface shape with infinitesimally small amplitudes cannot form in these systems. As has been discussed in Section 10.5.3, only systems with k near unity will give supercritical (normal) bifurcation with a single, well-defined critical growth rate V_c. The evolution of the wavelength for two temperature gradients (70 and 120 K/cm) is shown in Fig. 10-33b. At the onset of instability the experimentally determined

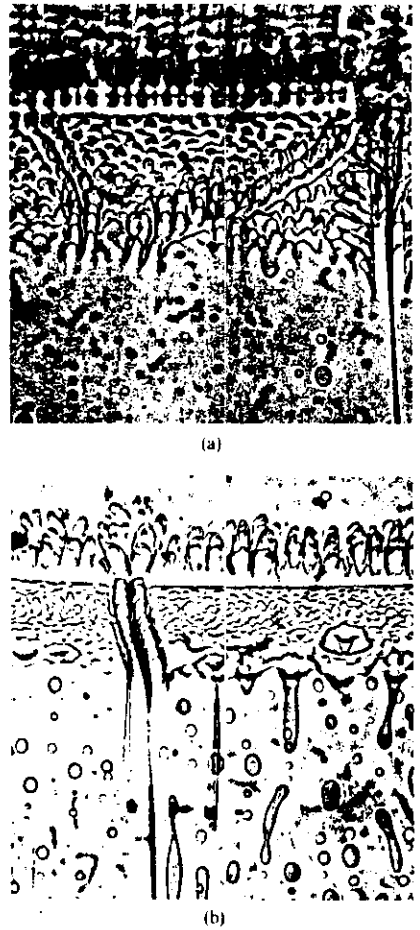

Figure 10-32. Morphological instabilities of a planar solid/liquid interface. Photograph (a) was taken at an earlier stage than (b). The beginning of the breakdown at defects such as dislocations, sub-grain boundaries, or grain boundaries intersecting with the solid/liquid interface is evident. The widths of the photographs correspond to 100 μm.

wavelength is larger than the critical wavelength by a factor 2–3 compared to linear stability analysis. Increasing the rate above the threshold leads to a decrease of the wavelength proportional to $V^{-0.4}$

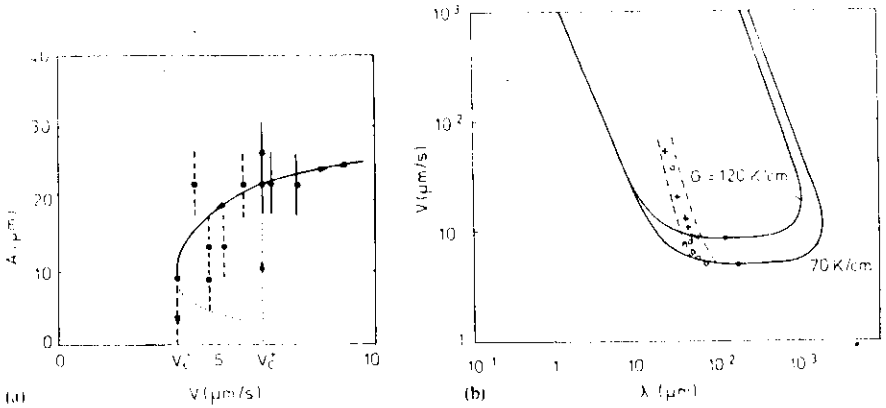

Figure 10-33. Amplitude, A, and wavelength, λ, of a periodic deformation of the solid liquid interface of CBr_4 Br_2 solution versus pulling speed (de Cheveigne et al., 1986). Diagram (a) shows the hysteresis between appearance and disappearance of perturbations (typical for an inverse bifurcation) for a temperature gradient of 12 K mm. The lines in diagram (b) represent the calculated neutral stability curves for the two gradients indicated. Open circles are experimental results for 7 K mm, and crosses, for 12 K mm. See also Fig. 10-21.

(de Cheveigne et al., 1986; Kurowsky, 1990). Once instability has started, the structure evolves to a steady state cellular or dendritic growth mode. Which one of these structures will finally prevail is a question of the growth conditions.

Cells and dendrites. Through an increase in V (or C_∞ or a decrease in G_T), a columnar dendritic structure can be formed out of a cellular array (Fig. 10-34). All three morphologies (instabilities, cells, dendrites) appear to have their own wavelength or array spacing. Owing to competition between neighboring crystals, the mean spacing of large amplitude cells seems to be always larger than that of the initial perturbations of the plane front, and the mean trunk distance (primary spacing λ) of the dendrites, larger than the spacing between smooth cells. The reason for this change in typical spacing is not clear yet. We will come back to this subject later. Before we do so, some relevant observations on tip growth need to be discussed.

The tip is the "head" of the dendrite where most of the structural features are initiated. Fig. 10-35 shows a dendrite tip of succinonitrile (SCN) with 1.3 wt.% acetone (ACE) in an imposed temperature gradient, $G_T = 16$ K/cm and a growth rate, $V = 8.3$ μm/s. The smooth tip of initially parabolic shape (Fig. 10-35 b) is clearly visible. In contrast to free thermal dendrites (Fig. 10-9), in DS of alloys the secondary instabilities start forming much closer to the tip. The imposed temperature gradient also widens the dendrite along the shaft relative to a parabola fitted to the tip. This effect increases with an increasing temperature gradient (Esaka, 1986).

The sequence of steady state growth morphologies, from well-developed large amplitude cells to well-developed dendrites, is shown in Fig. 10-36. Besides the information on the form and size of the corresponding growth morphologies, this figure also contains indications specifying the diffusion length $l = 2D/V$ and the ratio

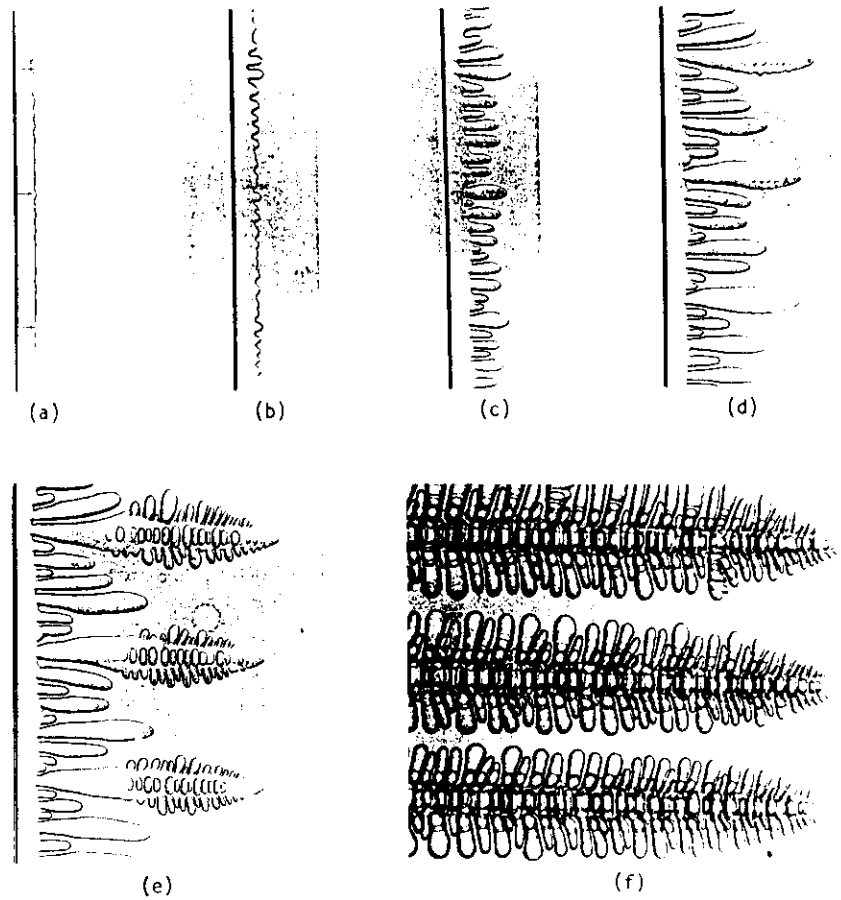

Figure 10-34. Time evolution of the solid-liquid interface morphology when accelerating the growth rate from 0 to 3.4 μm/s at a temperature gradient of 6.7 K mm. Magnification 41 ×. (a) 50 s, (b) 55 s, (c) 65 s, (d) 80 s, (e) 135 s, (f) 740 s (Trivedi and Somboonsuk, 1984).

of the half spacing over tip radius. The characteristic diffusion distance decreases more rapidly than the primary spacing of the dendrites (Fig. 10-36). When $l \gtrsim \lambda$ the ratio $\lambda/2R$ of directionally solidified SCN-1 wt.% ACE alloys is between 5.5 and 6 in agreement with numerical calculations, Section 10.5.3.

These observations are summarized in the diagram of Fig. 10-37. Three areas of growth can be differentiated for this alloy:

i) at low speeds, cells are found showing no side branches and a non-parabolic tip;

ii) at intermediate rates (over a factor 5 in V), cellular dendrites are formed with weakly developed secondary arms, and they

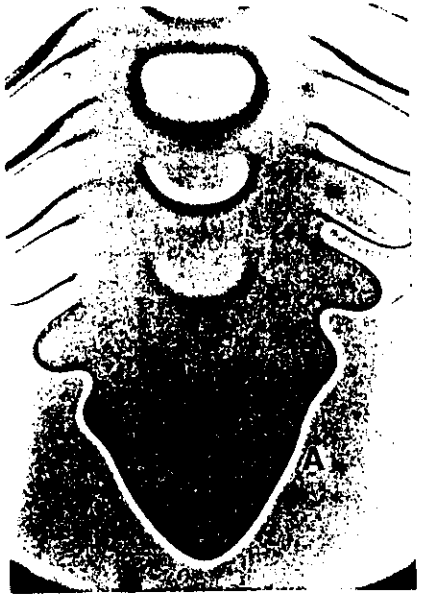

(a)

show an increasingly sharpened parabolic tip;

iii) at large rates dendritic arrays grow with well developed side branches and a tip size much smaller than the spacing.

It is difficult at present to judge the influence of the width of the gap of the experimental cell, which had approximately the same size as the diffusion distance, when $\lambda = l$. The corresponding growth rate also marks the transition from two- to three-dimensional growth of dendrites, as can be seen in Fig. 10-36. Under conditions A to C, no secondary arms are observed perpendicular to the plane of observation, while conditions D to F show well developed 3d dendrites even far behind the tip. Therefore, the gap might somewhat influence the values of the transition rates but not the qualitative behavior of the transition. As mentioned above, the theory (in quasi-stationary approximation) only indicates

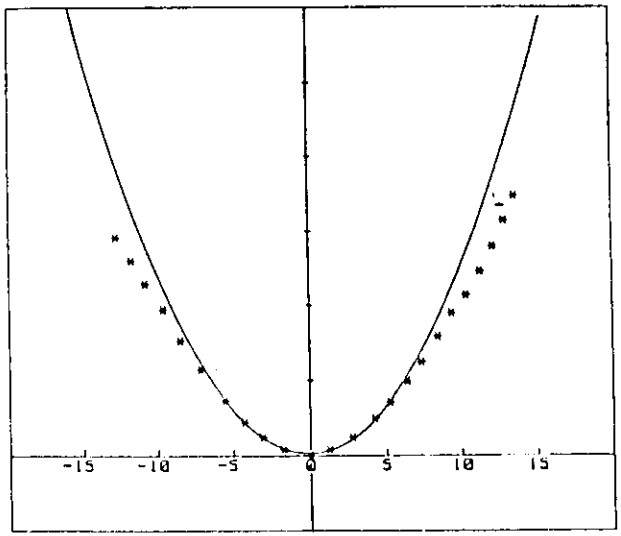

Figure 10-35. Dendrite tip of SCN 1.3 wt.% acetone solution in directional growth. (a) for $V = 8.3$ μm/s and $G = 1.6$ K/mm; (b) parabola fitting the tip growing at $V = 33$ μm/s and $G = 4.4$ K/mm (Esaka and Kurz, 1985; Esaka, 1986).

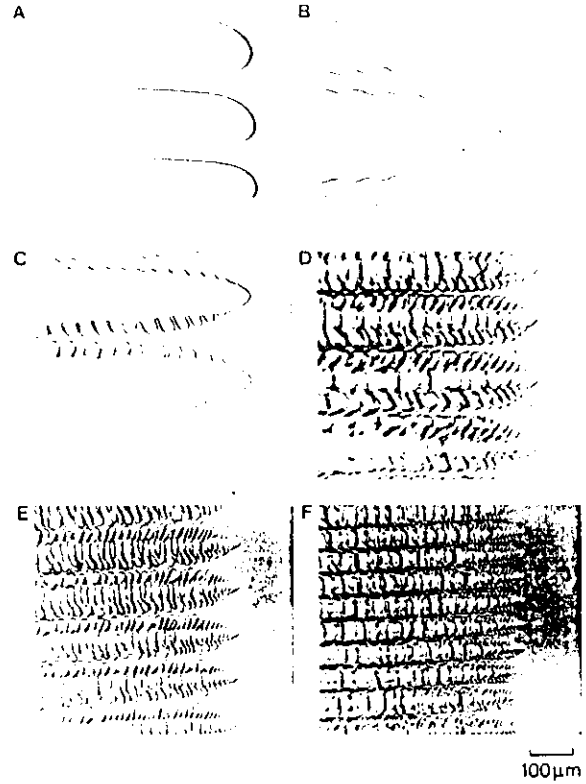

Figure 10-36. Cellular and dendritic growth morphologies in SCN 1.3 wt.% acetone; thermal gradient 8 K/mm $\leq G \leq$ 10.5 K/mm (Esaka, 1986). The growth rate, V in μm/s, the diffusion length $(2D/V)$ in mm, and the ratio of the primary trunk spacing to the tip diameter are as follows: A = 1.6, 1.6, 2.0; B = 2.5, 1.0, 2.5; C = 8.3, 0.3, 5.5; D = 16, 0.16, 6.0, E = 33, 0.08, 7.5; F = 83, 0.03, 9.0.

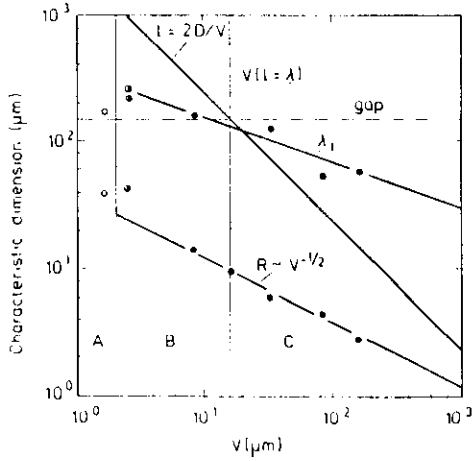

Figure 10-37. Primary trunk spacing, diffusion length, and tip radius of SCN 1.3 wt.% acetone dendrites as a function of the growth rate for a temperature gradient of 9.7 K/mm. The various points correspond to the conditions and microstructures given in Fig. 10-36 (Esaka, 1986). In region A no side arms are observed and the tips are of nonparabolic shape, in B the tip becomes parabolic and some side arms appear; in C well-developed side arms and a parabolic tip are the sign for isolated tips.

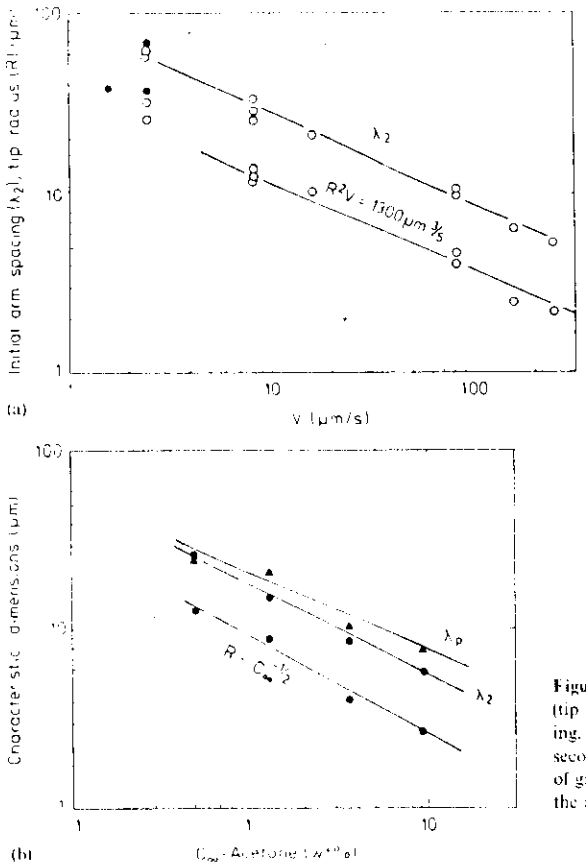

Figure 10-38. Characteristic dimensions (tip radius, R, initial secondary arm spacing, λ_2, and distance of appearance of secondary instabilities, λ_p) as a function of growth rate (a), and as a function of the alloy concentration (b) (Esaka, 1986).

a very gradual change in morphology. It is interesting to compare Fig. 10-36 with Figs. 10-25 and 10-26. It can be seen that both the theoretical and the experimental approaches show qualitatively the same behavior, even if the material constants used are not the same.

The scaling of the initial side-branch spacing λ_2 with respect to the tip radius is shown in Fig. 10-38. Both quantities scale closely with $L^2 V = \text{const.}$ or $L^2 C_\infty = \text{const.}$ (where $L \sim R$ or λ_2). Fig. 10-38 b shows also the quantity λ_p, the distance from the tip down the shaft, where the first signs of tip perturbations in the SCN-ACE system can be observed. Here λ_p is of the same order as λ_2.

The ratio λ_2/R obtained by Esaka and Kurz (1985) for SCN-1.3 wt.% ACE is independent of growth rate according to the precision of the measurements and takes a value of 2.1 ± 0.2 (see Fig. 10-39 and Table 10-1). This is in good agreement with the measurement of Somboonsuk and Trivedi (1985) who found a value of 2.0 on the same system over a wide range of growth rates.

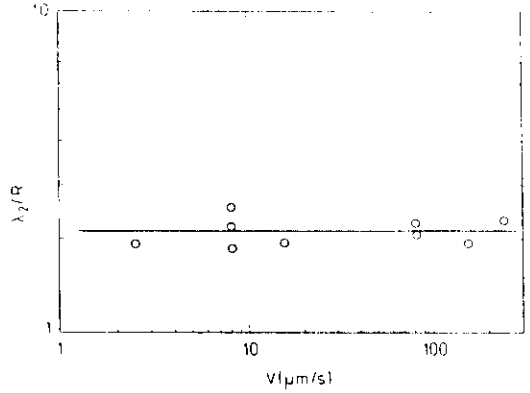

Figure 10-39. Ratio of initial arm spacing to tip radius as a function of growth rate (Esaka and Kurz, 1985).

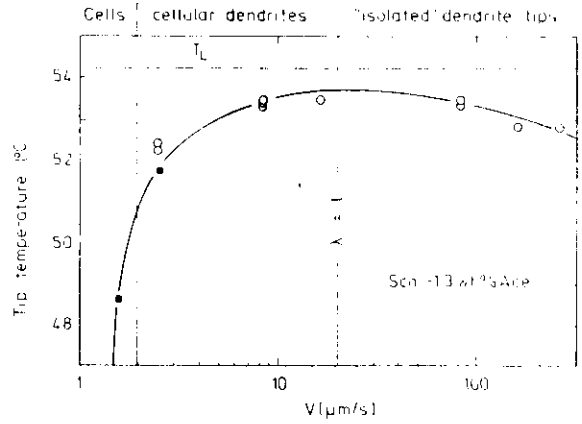

Figure 10-40. Tip temperatures of the dendrites of Fig. 10-36 as a function of growth rate (Esaka and Kurz, 1985). See also Fig. 10-28.

compositions, and temperature gradients (Trivedi and Somboonsuk, 1984). This ratio increases with crystal anisotropy in agreement with numerical calculations (Figs. 10-26, 10-29, 10-13) and decreases with increasing temperature gradient. On the other hand, its value is larger in the case of free dendritic growth (Table 10-1).

The tip undercooling of the dendrite is a measure of the driving force necessary for its growth at the imposed rate V. Fig. 10-40 shows the variation of the tip temperature with V, the undercooling being defined by the difference between T_m and the tip temperature. During an increase in growth rate, the cellular growth region is characterized by a decrease in undercooling, while toward the dendritic region, the undercooling increases again (Fig. 10-28).

One of the characteristics of directional solidification of dendrites is the formation of array structures with a primary trunk spacing λ. Its growth-rate dependence has been shown already in the log–log plot (Fig. 10-37). One can see that the slope of λ vs. V is initially smaller than the slope

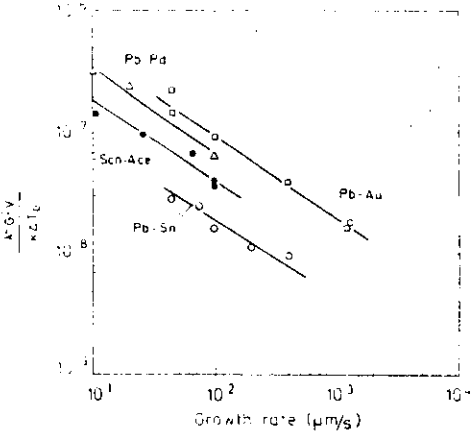

Figure 10-41. Normalized primary trunk spacing, λ, as a function of growth rate for various alloy systems (Somboonsuk et al., 1984). Note that the variation with growth rate at these high velocities is in agreement with the discussion in Section 10.5.5.

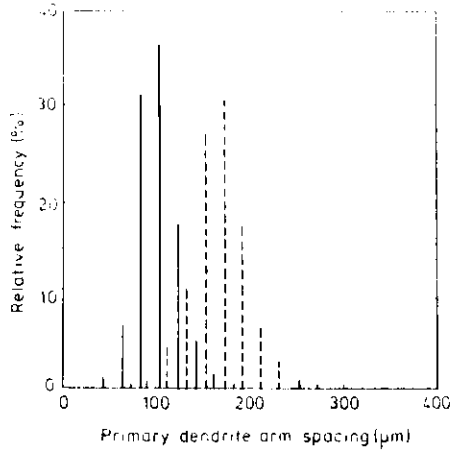

Figure 10-42. Distribution of nearest dendrite dendrite separations (primary trunk spacings) measured on a transverse section of a directionally solidified Ni-base superalloy (Quested and McLean, 1984). Solid lines for 16.7 μm/s and interrupted lines for 83.3 μm/s.

of R vs. V. If one takes the three points around $V(l = \lambda)$, where the tip temperature is approximately constant, the slope is about 0.25, while a mean slope through all measurements shown gives 0.4. This is fully consistent with recent data by Kurowsky (1990). Furthermore, it is in agreement with our arguments in Section 10.5.5.

Most of the measurements give a rate exponent somewhere between the two limiting values 0.25 - 0.5. Taking the lower value expressed by temperature gradient and concentration gives a relationship $\lambda \sim G_T^{-0.5} C_\infty^{0.25}$ (Hunt, 1979; Kurz and Fisher, 1981; Trivedi, 1984). Therefore, a normalized spacing $\lambda^4 G_T^2 V/k \Delta T_0$ is plotted vs. V in Fig. 10-41, showing that different materials behave similarly except for a constant factor (note that the solidus liquidus interval of an alloy, ΔT_0, is proportional to C_∞).

Primary spacings, however, are not uniquely defined but form a rather wide distribution. This is shown in Fig. 10-42 for one superalloy which was directionally solidified under different conditions. This behavior can be understood by examining the mechanism of wavelength (spacing) reduction through tail instability, which is a complicated process. A series of competitive processes between secondary and tertiary arms in a region behind the tip (of the order of one primary spacing) finally causes one tertiary branch to grow through and to become a new primary trunk (Esaka et al., 1988), as shown in Fig. 10-43 and Fig. 10-31.

Effects at high growth rates

As the final topic in this section, some interesting effects at very high growth rates which have been observed recently will be discussed. In laser experiments of the type shown in Fig. 10-7, the interface may be

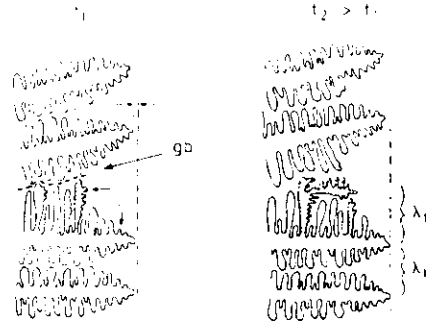

Figure 10-43. Mechanism for the formation of a new primary trunk by repeated branching of side arms at a grain boundary (gb). The increasing spacing at the gb allows a ternary branch to develop and to compete in its growth with other secondary branches (hatched arms) (Esaka et al., 1988).

driven to velocities of several m/s. Under such high rates, the structures becomes extremely fine. Primary spacings as small as 10 nm have been measured (Gremaud et al., 1990). Fig. 10-44 represents measured primary spacings (black squares), measured secondary spacings (open squares), and the calculated tip radius of the dendrites, using Ivantsov's solution and solvability-scaling criterion (Kurz et al., 1986, 1988). λ and λ_2 vary as $V^{-0.5}$, as does the tip radius when the Peclet number of the tip is not too large. At large Peclet numbers (or small diffusion distances), capillary forces become dominant, which is the reason for the limit of absolute stability, V_a.

Since the classical paper by Mullins and Sekerka (1964), it has been known that plane front growth should also be observed at interface rates where the diffusion length reaches the same order as the capillary length. This critical rate, called the limit of absolute stability, can be calculated from linear stability analysis (for temperature gradients which are not too high) approximately as

$$V_a = \Delta T_0 D k \Gamma$$

Here Γ is the ratio of solid-liquid interface energy to specific melting entropy. Typical limits are of the order of m/s. The precise value depends also on the effect of a varying solute diffusion coefficient (due to the large undercoolings), on the variations of k and ΔT_0 with the growth rate associated with the loss of local equilibrium, and, finally, on interface kinetics, which cannot be ignored. According to an extensive study of several alloy systems, it may be stated that at V_a one generally does not observe a simple plane front growth but

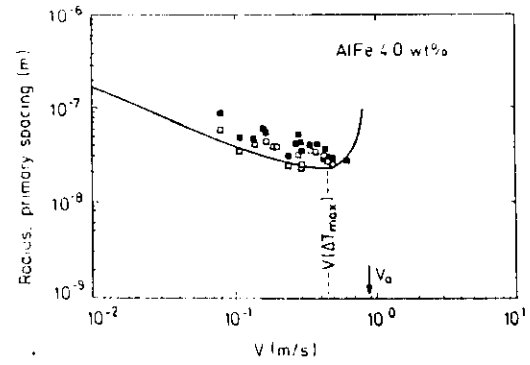

Figure 10-44. Experimentally determined primary spacings (black squares), secondary arm spacings (open squares) and calculated tip radius (line) for Al-4 wt% Fe alloy rapidly solidified by laser treatment. The minimum in tip temperature or the maximum in undercooling is due to the decreasing curvature undercooling when the dendrite approaches the limit of absolute stability, V_a (Gremaud et al., 1990).

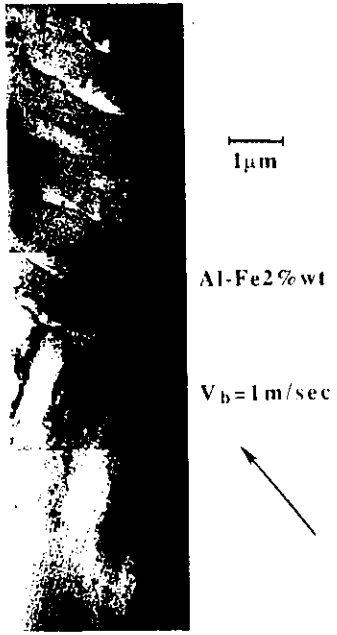

Figure 10-45. Transmission electron microscope (TEM) image, revealing the sharp transition between the dendritic structure and the banded structure in laser resolidified Al 2 wt.% Fe alloy. The laser scan direction is parallel to the narrow. The growth direction is from bottom left to top right. In the lower half of the photograph a columnar dendritic grain structure with a grain diameter of approximately 1 μm can be observed (Gremaud et al., 1990)

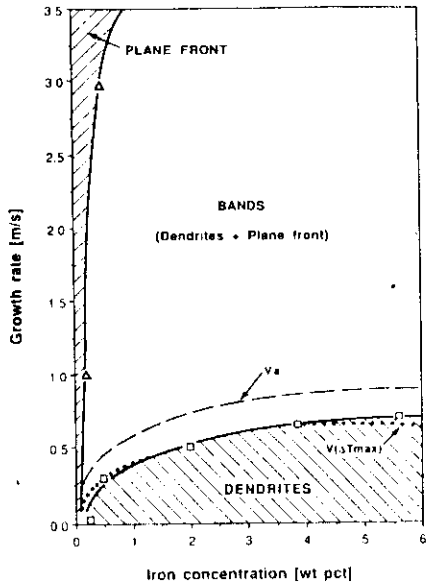

Figure 10-46. Microstructure selection diagram for Al–Fe alloys after laser resolidification (Gremaud et al., 1990). The experimentally determined transitions from dendrites to bands and from bands to precipitation free growth (plane-front growth) are indicated by squares and triangles. For a definition of calculated $V(\Delta T_{max})$ and V_a (broken lines) see Fig. 10-44.

rather an oscillating interface, which produces bands of plane front and dendritic morphology. Fig. 10-45 shows such a transition from columnar dendritic grains to bands. The possibility of chaotic interface motion was shown recently (Misbah et al., 1990b), and oscillatory motion of a plane interface with time was suggested (Corriell and Sekerka, 1983; Temkin, 1990). Growth rates much higher than V_a are needed in order to definitely produce an absolutely stable plane solid-liquid interface (Fig. 10-46).

10.5.7 Extensions

In this section, we summarize a few recent improvements of the theory of solidification regarding various effects which are important in the practical experimental situation. They are observed when experimental parameters are outside the range of the simple models considered in this article, or when additional factors influence the growth of the solid.

The models of this article are minimal in the sense that they were intended to capture the essence of a phenomenon with the smallest possible number of experimental parameters. Despite this simplification, however, the results appear to be of general importance.

The discussion of free dendritic growth has been restricted so far to small Peclet numbers or low supercoolings. In directional solidification, however, we are usually at moderate or even high Peclet numbers (Ben Amar, 1990; Brener and Melnikov, 1990a). It was shown by Brener and Melnikov (1990a) that in this case a deviation from dendritic scaling occurs if $Pe^{1/2}$ increases approximately beyond unity. At high growth rates, furthermore, kinetic coefficients can no longer be ignored at the interface. A proposed scaling relation (Brener and Melnikov, 1990b) was confirmed numerically (Classen et al., 1990), and combined anisotropy of surface tension and kinetic coefficient was treated analytically (Brener and Levine, 1990; Ben-Jacob and Garik, 1990). A general treatment of kinetic coefficients on interface stability was given by Caroli et al. (1988). For eutectic growth, this was formulated by Geilikman and Temkin (1984). For higher anisotropies than considered so far, one encounters facets on the growing crystals. This was analyzed for single dendrites (Adda Bedia and Ben Amar, 1990; Maurer et al., 1988; Raz et al., 1989; Yokoyama and Kuroda, 1988) and for directional solidification (Bowley et al., 1989). Unusual dendritic networks were observed in restricted geometries (Raz et al., 1990).

In our treatment of directional solidification, only one diffusion field was treated explicitly, namely the compositional diffusion. If a simple material grows dendritically (thermal diffusion), small amounts of impurities may become a matter of concern. This was reconsidered recently by Ben Amar and Pelce (1989), confirming the previous conclusion (Karma and Langer, 1984; Karma and Kotliar, 1985; Lipton et al., 1987) that impurities may increase the dendritic growth rate.

A subject of appreciable practical importance concerns the late stages of growth, where coarsening of the side branch structures occurs together with segregation (Kurz and Fisher, 1984). If elastic forces are not of primary importance, it is now generally accepted (see Chapter 7, Section 7.4.1) that a relation $L^* = A + Bt^{1/3}$ (Huse, 1986) is a good representation of typical length scales L^* varying with time t during diffusional coarsening processes. This confirms the classical Lifshitz-Slyozov-Wagner theory (Lifshitz and Slyozov, 1961; Wagner, 1961; Kawasaki, 1990). The result, however, is not specific concerning the geometric details, for example, in directional solidification, and it also assumes constant temperature.

We have only briefly mentioned the transition from dendritic arrays back to a plane front during directional solidification at very high speeds. The importance of kinetic coefficients was demonstrated by Brener and Temkin (1989), and recently, the possibility of chaotic dynamics in this region similar to those described in the Kuramoto-Sivashinsky equation was suggested by Misbah et al. (1990b).

A richness of dynamic phenomena was obtained in a stability analysis of eutectics (Datye et al., 1981). The possibility of *tilted lamellar arrays* in eutectics was demonstrated recently by Caroli et al. (1990) and Kassner and Misbah (1990a) and, similarly, for directional solidification at high speeds by Levine and Rappel (1990). This was observed in experiments on nematic liquid crystals (Beehhoefer et al., 1989) and in eutectics (Faivre et al., 1989).

Finally, the density difference between liquid and solid should have some marked

influence on the growth mode (Caroli et al., 1984, 1989). For dendritic growth, forced flow was treated in some detail by Ben Amar et al. (1988), Ben Amar and Pomeau (1990), Bouissou and Pelce (1989), Bouissou et al. (1989, 1990); Rabaud et al. (1988). Other sources of convective instability (Corriell et al., 1980; Vol. 15, Chap. 12) cannot be discussed here in any detail, as the literature is too extensive and not yet specific enough in the spirit of this chapter.

10.6 Eutectic Growth

10.6.1 Basic Concepts

Eutectic growth is a mode of solidification for a two-component system. Operating near a specific point in the phase diagram, it shows some unique features (Kurz and Fisher, 1984; Lesoult, 1980; Hunt and Jackson, 1966; Elliot, 1983).

The crucial point in eutectic growth is that the solidifying two-component liquid at a concentration near C_E (Fig. 10-19) can split into two different solid phases: The first phase consists of a high concentration of A atoms and a low concentration of B atoms; the second solid phase has the opposite concentrations. These two phases appear alternatively as lamellae or as fibers of one phase in a matrix of the other phase.

One condition for the appearance of a eutectic alloy is apparently a phase diagram (as sketched in Fig. 10-19) with a temperature T_E. The two-phase regions meet at (T_E, C_E), and the two liquidus lines intersect before they continue to exist as metastable liquidus lines (dash-dotted line) at temperatures somewhat below T_E. This is a material property of the alloy (Pb-Sn for example). The other condition is the experimental starting condition for the concentration in the high-temperature liquid. Assume that we are moving a container filled with liquid at concentration C_∞ in a thermal gradient field where the solid is cold, the liquid is hot, and the solidification front is proceeding towards the liquid in the positive z-direction. As a stationary solution, we find a similar condition to the simple directional solidification case; that is the concentration in the solid $\bar{C}_S$ averaged across the front must be equal to C_∞ to maintain global mass conservation together with a stationary concentration profile near the front.

Assume now that the liquid concentration at infinity, C_∞, is close to C_E and the temperature at the interface is at T_E. The solid may split into two spatially alternating phases now on the equilibrium (binodal) solidus lines $\bar{C}_S(T_I)$, one located near $C \to 0$, and one located near $C \to 1$ at $T_I < T_E$. To see what happens, let us look at the situation with the concentration in the liquid C_∞ being precisely at eutectic composition $C_\infty = C_E$. At $T_I < T_E$, there may now be alternating lamellae formed of solid concentration $\bar{C}_S^\alpha$ and $\bar{C}_S^\beta$ (Fig. 10-47), the corresponding metastable liquidus concentrations being at $\bar{C}_L^\alpha$ and $\bar{C}_L^\beta$. For both solid phases now the liquid concentration $C_\infty = C_E$ is in the metastable two-phase regions at T_I: $\bar{C}_S^\alpha < C_\infty < \bar{C}_L^\alpha$, $\bar{C}_L^\beta < C_\infty < \bar{C}_S^\beta$. In principle, one has to consider the possibility of metastable solid phases (Temkin, 1985), which we ignore here for simplicity.

Diffusion of excess material not incorporated into one of the lamellae does not have continue up to infinity but only to the neighboring lamella, which has the opposite composition relative to C_∞. Assuming again for simplicity a symmetric phase diagram, we may write this flux balance as

$$V C_L(1-k) = D \frac{\Delta \bar{C}}{(\lambda/2)} \tag{10-124}$$

where the left hand side describes the flux J of material to be carried away from each lamellar interface during growth at velocity V, which then must be equal to the diffusion current (concentration gradient) over a distance $\lambda/2$ to the neighboring lamella (across the liquid, as we ignore diffusion in the solid). $\Delta \bar{C} = \bar{C}_L^{(\alpha)} - \bar{C}_L^{(\beta)}$ is the concentration difference in the liquid at the interfaces of the lamellae, and $k < 1$ is the segregation coefficient.

With the help of the liquidus slopes $dT/d\bar{C}_L$ as material parameters, one can express the temperature depletion $\Delta T_I = T_E - T_I$ as

$$\Delta T_I = \Delta \bar{C} \cdot 2 \left| \frac{dT}{d\bar{C}_L} \right| \tag{10-125}$$

(symmetrical phase diagram assumed about C_L) and thus

$$\Delta T_I = 2 \left| \frac{dT}{d\bar{C}_L} \right| C_L(1-k) \frac{\lambda}{l} \tag{10-126}$$

Again, $l = 2D/V$ is the diffusion length.

So far we have ignored the singular points on the interface where the liquid and two lamellae α and β meet (Fig. 10-47). At this triple point in real space (or three-phase junction), the condition of mechanical equilibrium requires that the surface tension forces exerted from the three interfaces separating α, β, and the liquid cancel to zero. In the simplest version, this condition defines some angles ϑ_α, ϑ_β of the two solid-liquid interfaces relative to a flat interface. Accordingly, the growth front will become rippled, and the interfaces will have local curvature. What is worse, there is no guarantee that the α-β solid-solid interfaces are really parallel to the growth direction. Making a symmetry assumption for simplicity again, we can ignore this problem for the moment. The curvature K of the growth front at each lamella is then proportional to λ^{-1}. This curvature requires, through the Gibbs-Thomson relation, Eq. (10-97), another reduction, ΔT_K, of the interface temperature below T_I:

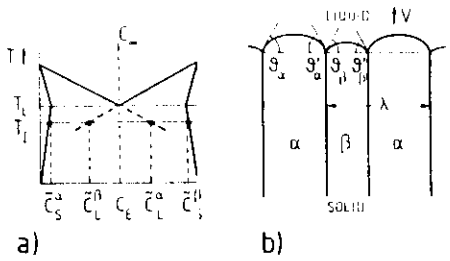

Figure 10-47. Sketch of symmetrical eutectic phase diagram (a) and eutectically growing lamellar cells (b), where α is the solid phase with concentration $\bar{C}_S^\alpha$, and β the solid phase with concentration $\bar{C}_S^\beta$. The average temperature at the interface is around T_I below the eutectic temperature T_E. The liquid at the interface is at metastable concentrations (dashed lines in (a)). The solid-liquid interfaces in (b) are curved and they meet with α-β interfaces at three-phase coexistence points.

$$\Delta T_K = T_E d K \tag{10-127}$$

where d is an effective capillary length, depending on surface tensions, with K now taken as $K \sim \lambda^{-1}$.

The total reduction of temperature below T_E during eutectic growth can thus be written as

$$\Delta T = \Delta T_I + \Delta T_K = T_E \cdot \left\{ a_I \frac{\lambda}{l} + a_K \frac{d}{\lambda} \right\} \tag{10-128}$$

with dimensionless constants a_I and a_K.

Plotting this supercooling as a function of lamellar spacing, one finds a minimal supercooling $\partial \Delta T / \partial \lambda = 0$ at

$$\lambda = \sqrt{a_K/a_I} \cdot \sqrt{l d} \tag{10-129}$$

Again, this is the fundamental scaling relation conjectured in Eq. (10-1) and encountered in various places in this chapter, where the origin is a competition between

driving force and stabilizing forces, most intuitively expressed in Eq. (10-128).

A more thorough theoretical analysis of eutectic growth was given in the seminal paper by Jackson and Hunt (1966), which is still a standard reference today. One basic approximation in this paper was to average the boundary conditions on flux and temperature over the interface. This led to Eq. (10-128), and it was argued that the minimum undercooling would serve as the operating point of the system with spacings given by Eq. (10-129).

This stationary calculation was extended by Datye and Langer (1981) to a dynamic stability analysis, where the solid–solid-liquid triple points could move parallel and perpendicular to the local direction of growth, coupled however to the normal direction of the local orientation of the front. It was found that the marginal stability coincided exactly with the point of minimum undercooling.

The basic model equations for eutectic growth in a thermal gradient field can be written in scaled form as follows (Brattkus et al., 1990; Caroli et al., 1990). Neglecting diffusion in the solid (one-sided model) and assuming a single diffusion coefficient D for solute diffusion near eutectic concentration C_E (Fig. 10-47), we assume a symmetric phase diagram about C_E for simplicity.

We define a relative (local) concentration gap as

$$\delta = \frac{\Delta C_\alpha}{\Delta C} \tag{10-130}$$

with $\Delta C_\alpha = C_E - \tilde{C}_\xi^\alpha(T)$, $\Delta C_\beta = \tilde{C}_\xi^\beta(T) - C_E$ and $\Delta C = \Delta C_\alpha + \Delta C_\beta$.

The dimensionless composition is then defined as

$$u = \frac{C - C_E}{\Delta C(T_E)} \tag{10-131}$$

and (in contrast to the previous definitions) we express lengths and times in units of a diffusion length $\bar{l}$ and time $\bar{\tau}$

$$\bar{l} = D/V, \quad \bar{\tau} = D/V^2 \tag{1-132}$$

(Note that $\bar{l}$ here differs by a factor of 2 from previous definitions.) Restricting our attention to two dimensions corresponding to lamellar structures, we now define the diffusion equation as

$$\frac{\partial u}{\partial t} = \nabla^2 u + \frac{\partial}{\partial z} u \tag{10-133}$$

The conservation law at the interface $z = \zeta(x, t)$ is

$$-\hat{n} \cdot \nabla u = \Delta(x, t)(1 + \dot{\zeta})\, n_z \tag{10-134}$$

with the unit vector $\hat{n}$ normal to the interface and

$$\Delta(x, t) = \begin{cases} \delta & \text{for } x \text{ in } \alpha/\lambda\text{-front regions} \\ \delta - 1 & \text{for } x \text{ in } \beta/\lambda\text{-front regions} \end{cases} \tag{10-135}$$

The Gibbs-Thomson relation for the boundary becomes

$$u(\zeta, t) = \begin{cases} -d_\alpha K - \dfrac{\zeta}{l_{T_\alpha}} & \text{in } \alpha/\lambda\text{-regions} \\ -d_\beta K - \dfrac{\zeta}{l_{T_\beta}} & \text{in } \beta/\lambda\text{-regions} \end{cases} \tag{10-136}$$

(Kinetic coefficients were considered by Geilikman and Temkin, 1984.) Finally, and this is a new condition in comparison with the simple directional solidification, the triple point where three interfaces meet should be in mechanical equilibrium

$$\gamma_{\alpha L} + \gamma_{\beta L} + \gamma_{\alpha\beta} = 0 \tag{10-137}$$

with the surface tension vectors γ oriented so that each vector points out of the triple point and is tangent to the corresponding interface. K is the local curvature of the interface, being positive for a solid bulging into the liquid. The dimensionless capillary

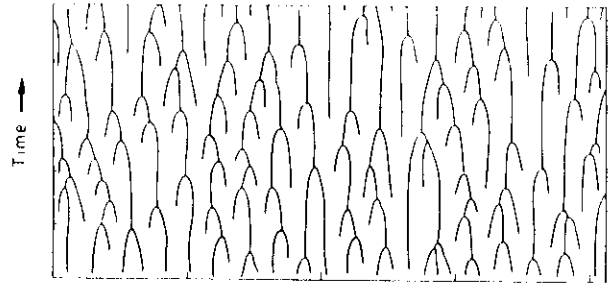

Figure 10-48. Turbulent behavior of lamellar spacings with time in a simplified model of eutectic growth (Datye et al., 1981).

and thermal lengths associated with the α-phase are

$$d_\alpha = \frac{1}{\bar{l}} \frac{\gamma_{\alpha L} T_E}{m_\alpha(\Delta C) L_\alpha} \tag{10-138}$$

$$l_{T_\alpha} = \frac{1}{\bar{l}} \frac{m_\alpha(\Delta C)}{G_T} \tag{10-139}$$

and are equivalent for the β phase, with $m_\alpha = |\mathrm{d}T/\mathrm{d}\tilde{C}_\xi^\alpha|$ as the absolute liquidus slope, G_T as the fixed thermal gradient and L_α as the specific latent heat. At infinity, $z \to \infty$, the boundary condition to Eq. (10-133) is u_∞, depending on the initial concentration in the liquid. This then forms a closed set of equations.

Ahead of the eutectic front, the diffusion field can be thought of as containing two ingredients: a diffusion layer of thickness $\bar{l}$ associated with global solute rejection and modulations due to the periodic structure of the solid of the extent $\lambda (\lambda \ll \bar{l})$. When the amplitude of the front deformations is small compared to these lengths, the averaging approximation by Jackson and Hunt (1966) (and also by Datye and Langer, 1981) seems justified.

This point was recently taken up by Caroli et al. (1990) who found that only in the limit of large thermal gradient

$$G_T \gg V m(\Delta C)/D \tag{10-140}$$

is the approximation safe. This approximation appears difficult to reach experimentally, though.

In an attempt to shed some light on wavelength selection, Datye et al. (1981), (Langer, 1980b) considered finite amplitude perturbations of the local wavelength Fig. 10-48. This type of approach was used in a somewhat refined version by Brener et al. (1987). They derived an approximate potential function for wavelengths λ and argued that under finite amplitude of noise, the wavelength selected on average is defined by a balance in the creation rates and the annihilation rates of lamellae. In other words, if lamellae disappear through suppression by neighboring lamellae and appear through nucleation, then an equal rate of these processes leads to a selection of an average spacing $\bar{\lambda}$, because both depend on λ. The operating point was found in a limited interval near the wavelength corresponding to minimal supercooling (or maximal velocity in an isothermal process) and, accordingly, is described by Eq. (10-129).

More recent extensions of the theory (Coullet et al., 1989) gave indications that the orientation of the lamellae (under isotropic material parameters) are necessarily parallel to the growth direction of the front

but may be tilted and travel sideways at some specific angles (Caroli et al., 1990; Kassner and Misbah, 1990a). Finally, it was found (Kassner and Misbah, 1990b) that the standard model of eutectic solidification has an intrinsic scaling structure

$$\lambda \sim \sqrt{l d}\, f(l/l_f) \qquad (10\text{-}141)$$

with a scaling function f depending only on l/l_f so that $\lambda \sim V^{-1/2}$ for $2l \lesssim l_f$ or for high enough velocities, while at smaller velocities the exponent should be smaller: $\lambda \sim V^{-0.3}$. This is in good agreement with the arguments given for ordinary directional solidification and also explains a large number of experimental data (Lesoult, 1980).

To summarize, the selection of lamellar spacings in eutectics again seems to follow Eq. (10-1) or (10-129), but the field is very active at the moment and some further insight into the detailed mechanisms of pattern selection in solidification may arise in the near future. (See also the remarks in Section 10.5.7.)

10.6.2 Experimental Results on Eutectic Growth

Eutectic growth was a subject of much interest to experimentalists in the late 1960s and early 1970s. Substantial research has been motivated by the possibility of developing new high-temperature materials. The in situ directional solidification of two phases of very different properties is an interesting method of producing composite materials with exceptional properties. However, since these materials could not outperform the more conventional, directional solidified dendritic superalloys in the harsh environment of a gas turbine, the interest dropped. Therefore, most of the research on eutectics was performed before 1980 (for a review, see Kurz and Sahm, 1975; Elliott, 1983). One exception is the ongoing research concerning eutectic casting of alloys such as cast iron (Fe–C or Fe–Fe_3C eutectic) and Al–Si.

Casting-alloys are generally inoculated and solidify in equiaxed form (free eutectic growth) (see Vol. 15, Chap. 1). This fact, however, does not make any substantial difference for their growth behavior because growth is solute diffusion controlled in nearly all cases due to the high concentration of the second element. The models described above therefore apply to both directional and free solidification.

The different alloys can be classified into four groups of materials (Kurz and Fisher, 1984): lamellar or fibrous systems, and non-facetted non-facetted (nf nf) or non-facetted facetted (nf f) systems.

The distinction between f and nf growth behavior can be made with the aid of the melting entropy. Small entropy differences ΔS_f between liquid and solid (typical for

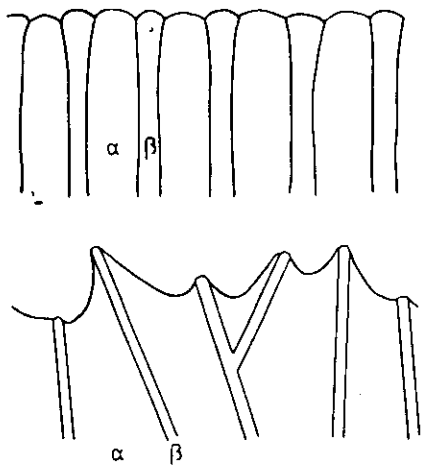

Figure 10-49. Solid liquid interface morphologies of (a) regular (nf nf) eutectics and of (b) irregular (nf f) eutectics during growth

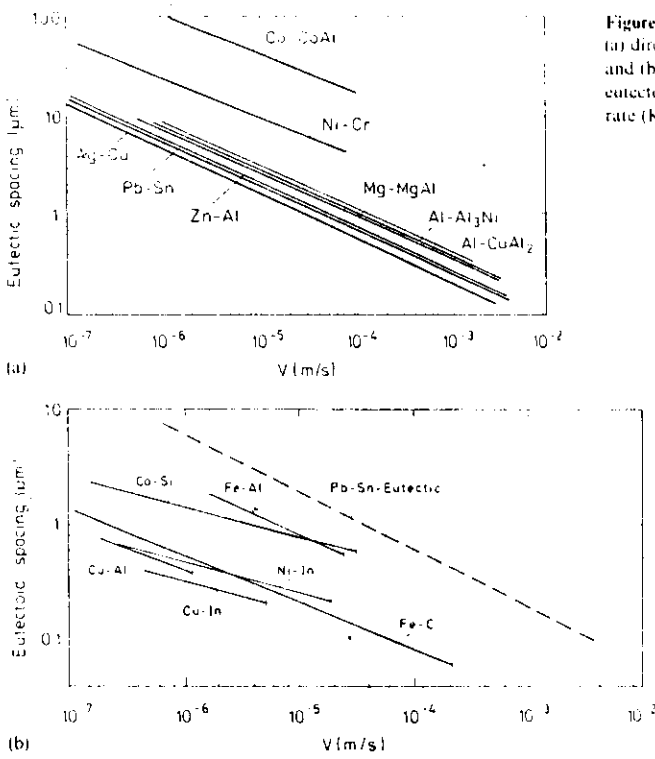

Figure 10-50. Lamellar spacings of (a) directionally solidified eutectics and (b) directionally transformed eutectoids as a function of growth rate (Kurz and Sahm, 1975).

metals and plastic crystals such as SCN, PVA etc.) lead to nf growth with atomically rough interfaces. Materials with large ΔS_f values are prone to form atomically smooth interfaces, which lead to the formation of macroscopically facetted appearence.

In the case of nf/nf eutectics, volume fractions (of one eutectic phase) of less than 0.3 lead generally to fibers, while at volume fractions between 0.3 and 0.5, lamellar structures prevail. The microstructures of nf/nf eutectics (often simple metal/metal systems) are considered regular and those of nf/f eutectics (mostly the above-mentioned casting alloys) are considered irregular. Fig. 10-49 shows schematically the morphology of the growth front in both cases. It can be easily understood that growth in nf/nf eutectics is much more of a steady state type than it is in f/nf eutectics.

Regular structures

Applying a criterion such as growth at the extremum to the solution of the capillary-corrected diffusion equations (Jackson and Hunt, 1966), Eq. (10-128), one obtains for nf/nf eutectics the well known relationships (Eq. (10-129))

$$\lambda^2 V = C$$

$$\Delta T^2 / V = 4C'$$

where C and C' are constants. Fig. 10-50 shows that this behavior has been observed globally in many eutectic systems,

some of them having been studied over five orders of magnitude in velocity. The situation is much less clear when it comes to analyzing eutectoid systems. (Eutectoids are "eutectics" with the liquid parent phase replaced by a solid.) Often a $\lambda^3 V$ relationship is found in these systems (Fig. 10-50 b) over some range of the variables. (See Eq. (10-141).)

In general, it may be said that the field of eutectic growth is underrepresented in materials research, and many more careful studies are needed before a clearer insight into their growth can be gained. Recently, Trivedi and coworkers started such research, and some of their results are presented here. Fig. 10-51 indicates that in eutectics the spacings are also not at all uniquely defined. There is a rather wide distribution around a mean value for each rate (Trivedi et al., 1990). The operating range of eutectics is determined by the permanent creation and movement of faults (see below). This process is three dimensional and cannot be realistically simulated in two-dimensional calculations.

In Fig. 10-52, the mean spacings are plotted as points, and the limits of the distribution are given by the extension of the bars. From the calculated range of stability, which has been discussed by Jackson and Hunt (1966), it can be seen that the minimum of the experimental values coincides with the theoretical prediction (see also Section 10.6.1). This, however, does not provide definitive proof for this prediction, due to the fact that several physical parameters of the system are not precisely known. On the other hand, it is clear that eutectic spacings do not explore the upper range of stability (catastrophic breakdown), at least not in nf/nf systems. Some other mechanism limits the spacing at its upper bound. The adjustment of spacings is a

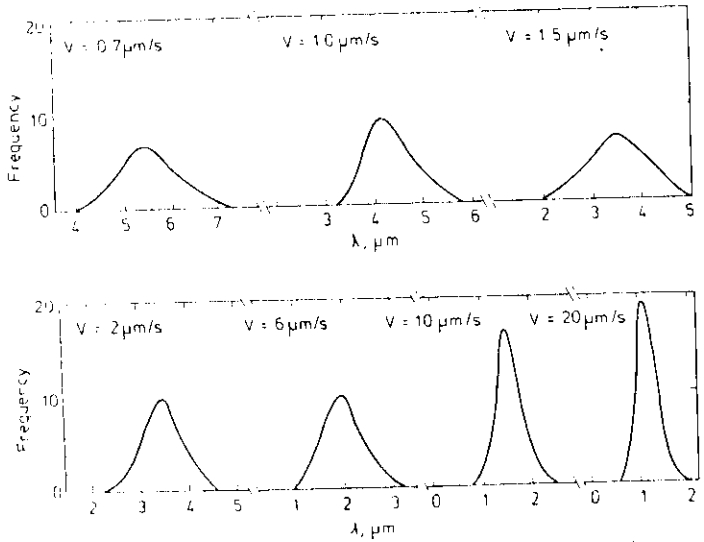

Figure 10-51. Eutectic spacing distribution curves as a function of velocity for Pb–Pd eutectic (Trivedi et al., 1990).

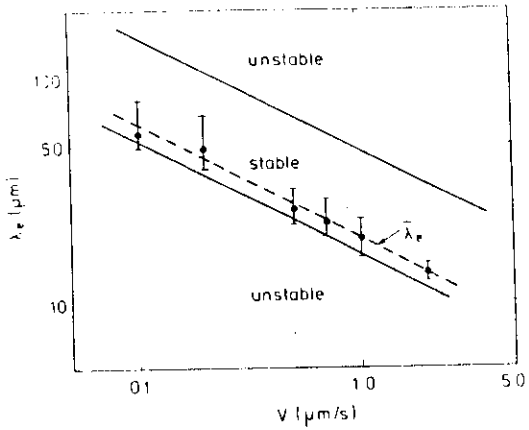

Figure 10-52. A comparison of the experimental results on the interlamellar spacing variation with velocity for CBr_4–C_2Cl_6 with the theoretical values (solid lines) for two marginally stable spacings (Seetharaman and Trivedi, 1988).

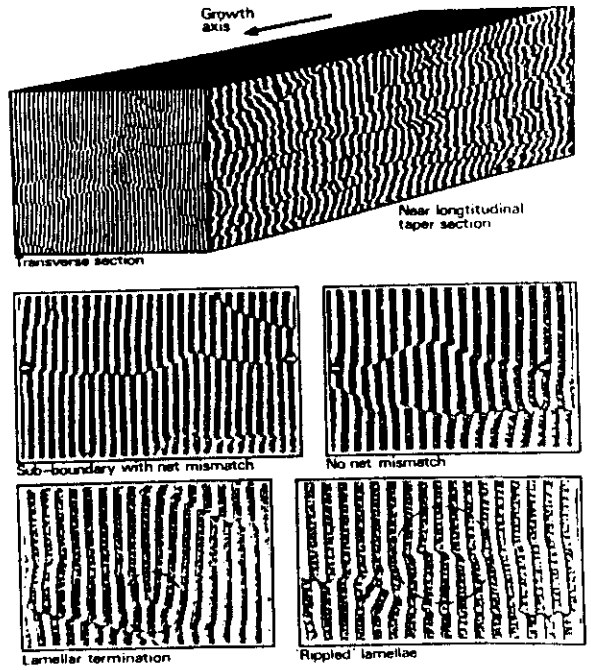

Figure 10-53. Eutectic fault structures in directionally solidified Al–$CuAl_2$ alloy (Double, 1973).

rapid process, and its rate increases when the spacing increases (Seetharaman and Trivedi, 1988).

Irregular structures

The above relationships for eutectic spacing and undercooling as a function of growth rate are also useful in the case of irregular systems such as the nodular cast alloys Fe–C or Al–Si (Fig. 10-49 b). Jones and Kurz (1981) have introduced a factor, φ, which is equal to the ratio of the mean spacing, $\langle\lambda\rangle$, of the irregular structure to the spacing at the extremum. This leads to the following relationships:

$$\langle\lambda\rangle^2 V = \varphi^2 C$$

$$\langle\Delta T\rangle^2 V = [\varphi + (1/\varphi)]^2 C'$$

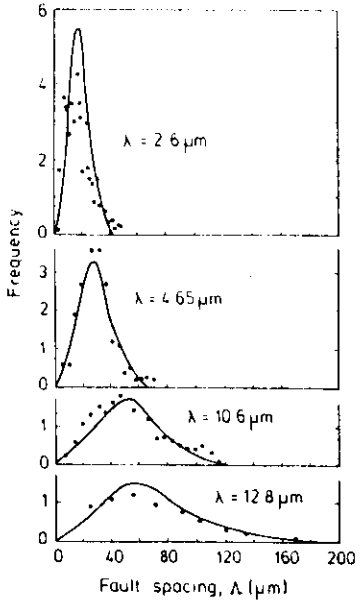

Figure 10-54. Eutectic fault spacing distribution curves for Al–$CuAl_2$ directionally solidified with different growth rates and spacing values as indicated (Riquet and Durand, 1975).

Faults

Defects in the ideal lamellar or fibrous structure are an essential ingredient for eutectic growth. They allow the two phase crystal to rotate into crystallographically (energetically) favorable orientations (Hogan et al., 1971) and to adapt its spacing to the local growth conditions. In lamellar systems, there are different types of

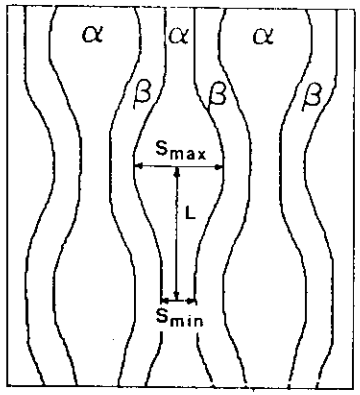

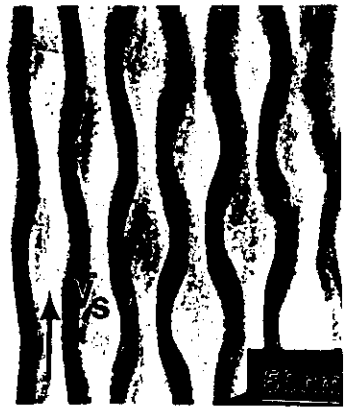

Figure 10-55. Periodic oscillations in hypoeutectic Al–$CuAl_2$ eutectic under rapid laser resolidification conditions: (a) experimental observation and (b) simulation (Zimmermann et al., 1990; Karma, 1987).

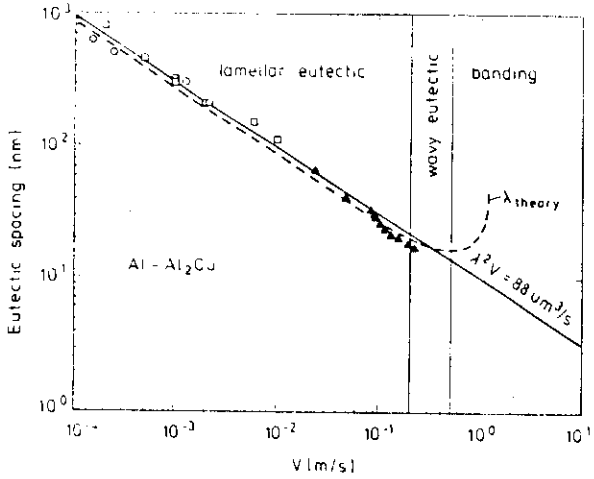

Figure 10-56. Interlamellar spacings of Al–$CuAl_2$ eutectic for low solidification rates (open symbols) and high solidification rates (black triangles) (Zimmermann et al., 1989).

faults (Double, 1973): single or extended faults, with or without net mismatch (Fig. 10-53). They mostly represent subboundaries of an eutectic grain and could develop through polygonization of dislocations which form because of the stresses created at the interphase boundaries of the composite. Fig. 10-54 shows distributions of fault spacings, Λ, for different growth rates indicated by different lamellar spacings, λ (Riquet and Durand, 1975). In the case of nonfaceted fibrous structures, the faults are formed by simple fiber branches or terminations.

Oscillations

Periodic oscillations have been observed as a morphological instability in several systems grown under various conditions (Hunt, 1987; Carpay, 1972; Zimmermann et al., 1990). These morphological instabilities form in off-eutectic alloys even at growth rates of several cm/s as is shown in Fig. 10-55. The correspondence of the observed structures with the results of theoretical modelling by Datye and Langer (1981) and by Karma (1987) is striking.

As was the case with dendrites, eutectics also form extremely fine microstructures when they are subject to rapid solidification. A distance of 10 nm (each phase is some 15 atoms wide) seems to be the minimum spacing which can be achieved. In Fig. 10-56, recent measurements of interlamellar spacings in the Al–Al_2Cu system are given. They fall fairly well on the line of all of the other measurements for that system ($\lambda^2 V = 88\ \mu m^3/s$), which have been obtained in DS experiments.

Above a certain limit corresponding to the rate of absolute stability of one of the eutectic phases (in the Al–Al_2Cu system the α-phase), bands form just as they do in dendritic alloys. The only difference is that the dark bands are not formed by dendritic structure but by eutectic structure (Fig. 10-57). For more details about rapidly solidified eutectics, the reader is referred to Zimmermann et al. (1989), Kurz and Trivedi (1991).

Figure 10-57. Details of banded structure in Al–$CuAl_2$ eutectic showing also the spots where chemical analysis in the TEM has been made (Zimmermann et al., 1989).

10.7 Summary and Outlook

During the past ten years, very substantial improvements in our understanding of the pattern-forming processes in solidification have been achieved. Although the basic model equations were already known for several decades, it was only during those recent years that the mathematical and numerical tools were pushed to allow for a reliable analysis of the complicated expressions. In addition, careful experiments have been performed largely on model substances, which have given an impressive number of precise, quantitative data. This combined effort has basically solved the problem of free dendritic growth with respect to velocity selection and side branch formation.

In the process of directional solidification, a consistent picture is now emerging, relating the growth mode to free dendritic growth and, at the same time, to viscous fingering and growth in a channel. At very high growth rates that approach the limit of absolute stability, the situation is still somewhat unclear, for nonequilibrium effects like kinetic coefficients then become of central importance. These quantities are difficult to determine experimentally. Furthermore, the selection of the primary spacings of the growing array of cells and dendrites is still subject to discussion. One such point of contention, for example, is the typically observed increase in spacing when moving from cellular to dendritic structures in model substances. It is also unclear what happens in the limit of vanishing crystalline anisotropy.

In eutectic growth, the situation is even less understood, for sufficient reasons. The three-phase junctions at the solid-liquid interface enter as additional conditions and further details of the phase diagram become important. The dynamics of the system seem to show a richer structure than ordinary directional solidification. The selection of spacings between the different solid phases in materials of practical importance occurs through three-dimensional defect formation. In addition, nucleation and facetting of the interfaces should be considered.

A number of problems common to all of these growth modes have only been touched upon so far. These problems include, for example, the redistribution of material far behind the tip regions, the treatment of elastic effects, and the interaction with hydrodynamic instabilities due to thermal and compositional gradients.

In summary, we expect the field to remain very active in the future, as it is attractive from a technological point of view. It will certainly provide some surprises and new insights for the general concepts of pattern formation in dissipative systems.

10.8 References

Adda Bedia, M., Ben Amar, M. (1990), to be published.

Baker, J.C., Cahn, J. (1971), in: *Solidification*. Hughel, T.A., Bolling, G.F. (Eds.). Metals Park, Oh: American Society of Metals.

Barber, M.N., Barbieri, A., Langer, J.S. (1987), *Phys. Rev. A 36*, 3340.

Barbieri, A., Hong, D.C., Langer, J.S. (1987), *Phys. Rev. A 35*, 1802.

Bechhoefer, J., Libchaber, A. (1987), *Phys. Rev. Lett. 35*, 1393.

Bechhoefer, J., Simon, A.J., Libchaber, A., Oswald, P. (1989), *Phys. Rev. A 40*, 3974.

Ben Amar, M. (1990), *Phys. Rev. A 41*, 2080.

Ben Amar, M., Moussallam, B. (1987), *Physica 25 D*, 155.

Ben Amar, M., Pelce, P. (1989), *Phys. Rev. A 39*, 4263.

Ben Amar, M., Pomeau, Y. (1986), *Europhys. Lett. 2*, 307.

Ben Amar, M., Pomeau, Y. (1990), to be published

Ben Amar, M., Bouissou, Ph., Pelce, P. (1988), *J. Crystal Growth 92*, 97.

Ben-Jacob, E., Garik, P. (1990), *Nature 343*, 523.

Ben Jacob, E., Goldenfeld, N., Langer, J.S., Schön, G. (1983), *Phys. Rev. Lett. 51*, 1930.

Ben Jacob, E., Goldenfeld, N., Langer, J.S., Schön, G. (1984), *Phys. Rev. A 29*, 330.

Bensimon, D., Pelce, P., Shraiman, B.I. (1987), *J. Phys. France 48*, 2081.

Bilgram, J.H., Firmann, M., Hürlimann, E. (1989), *J. Cryst. Growth 96*, 175.

Billia, B., Jamgotchian, H., Capella, L. (1987), *J. Crystal Growth 82*, 747.

Billia, B., Jamgotchian, H., Capella, L. (1989), *J. Crystal Growth 94*, 987.

Bouissou, Ph., Pelce, P. (1989), *Phys. Rev. A 40*, 6673.

Bouissou, Ph., Perrin, B., Tabeling, P. (1989), *Phys. Rev. A 40*, 509.

Bouissou, Ph., Chiffaudel, A., Perrin, B., Tabeling, P. (1990), *Europhys. Lett. 13*, 89.

Bowley, R., Caroli, B., Caroli, C., Graner, P., Nozieres, P., Roulet, B. (1989), *J. Phys. France 50*, 1377.

Brattkus, K., Misbah, C. (1990), *Phys. Rev. Lett. 64*, 1935.

Brattkus, K., Caroli, B., Caroli, C., Roulet, B. (1990), *J. Phys. France 51*, 1847.

Brener, E.A., Levine, H. (1990), to be published.

Brener, E.A., Melnikov, V.I. (1990a), *J. Phys. France 51*, 157.

Brener, E.A., Melnikov, V.I. (1990b), to be published.

Brener, E.A., Temkin, D.E. (1989), *Europhys. Lett. 10*, 171.

Brener, E.A., Geilikman, M.B., Temkin, D.E. (1987), *Sov. Phys. JETP 65*, 93.

Brener, E.A., Geilikman, M.B., Temkin, D.E. (1988), *Sov. Phys. JETP 67*, 1002.

Brazovsky, S. (1975), *Sov. Phys. JETP 41*, 85.

Burden, M.H., Hunt, J.D. (1974), *J. Cryst. Growth 22*, 99.

Burkhardt, T., Kroll, D., Müller-Krumbhaar, H. (1977), *J. Crystal Growth 38*, 13.

Callen, H.B. (1960), *Thermodynamics*. New York: Wiley.

Caroli, B., Caroli, C., Misbah, C., Roulet, B. (1986b), *J. Phys. France 47*, 1623.

Caroli, B., Caroli, C., Roulet, B. (1982), *J. Phys. France 43*, 1767.

Caroli, B., Caroli, C., Roulet, B. (1984), *J. Crystal Growth 66*, 575.

Caroli, B., Caroli, C., Roulet, B. (1987), *J. Phys. France 48*, 1423.

Caroli, B., Caroli, C., Roulet, B. (1988), in: *Solid State Phenomena*. Kubin, L.P., Martin, G. (Eds.) Aedermannsdorf, CH: Trans. Tech. Publ.

Caroli, B., Caroli, C., Roulet, B., Faivre, G. (1989), *J. Crystal Growth 94*, 253.

Caroli, B., Caroli, C., Roulet, B., Langer, J.S. (1986a), *Phys. Rev. A 33*, 442.

Caroli, B., Caroli, C., Roulet, B., Brattkus, K. (1990), *J. Phys. France 51*, 1865.

Carpay, F.M.A. (1972), in: *Handbuch der Mikroskopie in der Technik*. Vol. VI: Freund, H. (Ed.). Frankfurt: Umschau, p. 355.

Chan, S.-K., Reimer, H.-H., Kahlweit, M. (1978), *J. Cryst. Growth 43*, 229.

Chandrasekhar, C. (1961), *Hydrodynamics and Hydrodynamic Stability*. Oxford: Clarendon.

de Cheveigne, S., Guthman, C., Lebrun, M.M. (1986), *J. Physique 47*, 2095.

Chopra, M.A., Glicksman, M.E., Singh, N.B. (1988), *Metall. Trans. 19 A*, 3087.

Classen, A., Misbah, C., Müller-Krumbhaar, H. (1990), to be published.

Collins, J.B., Levine, H. (1985), *Phys. Rev. B31*, 6119.

Corriell, S., Cordes, M., Boettinger, M., Sekerka, R. (1980), *J. Crystal Growth 49*, 13.

Corriell, S., Sekerka, R.F. (1983), *J. Crystal Growth 61*, 499.

Coullet, P., Goldstein, R.E., Gunaratne, G.H. (1989), *Phys. Rev. Lett. 63*, 1954.

Datye, V., Langer, J.S. (1981), *Phys. Rev. B 24*, 4155.
Datye, V., Mathur, R., Langer, J.S. (1981), *J. Stat. Phys. 29*, 1.
Deissler, R.J. (1987), *Physica 22 D*, 233.
Dombre, T., Hakim, V. (1987), *Phys. Rev. A 36*, 2811.
Double, D.D. (1973), *Mater. Sci. Eng. 11*, 325.
Dougherty, A. (1990), to be published.
Dougherty, A., Gollub, J.P. (1988), *Phys. Rev. A 38*, 3043.
Dougherty, A., Kaplan, P.D., Gollub, J.P. (1987), *Phys. Rev. Lett. 58*, 1652.
Eckhaus, W. (1965), *Studies in Nonlinear Stability Theory; Springer Tracts in Natural Philosophy 6*. Berlin: Springer.
Elliot, R. (1983), *Eutectic Solidification Processing Crystalline and Glassy Alloys*. London: Butterworths.
Esaka, H. (1986), Sc.D. thesis, EPFL, Lausanne, CH.
Esaka, H., Kurz, W. (1985), *J. Cryst. Growth 72*, 578.
Esaka, H., Kurz, W., Trivedi, R. (1988), in: *Solidification Processing 1987*. London: The Institute of Metals, p. 198.
Eshelman, M., Seetharaman, V., Trivedi, R. (1988), *Acta Metall. 36*, 1165.
Eshelman, M.A., Trivedi, R. (1987), *Acta Metall. 35*, 2443.
Faivre, G., de Cheveigne, S., Guthmann, C., Kurowsky, P. (1989), *Europhys. Lett. 9*, 779.
Fisher, D.J., Kurz, W. (1978), unpublished.
Fisher, D.J., Kurz, W. (1980), *Acta Metall. 28*, 777.
Fujioka, T. (1978), Ph.D.-Thesis, Carnegie-Mellon Univ. Pittsburgh (unpublished).
Geilikman, M.B., Temkin, D. (1984), *J. Crystal Growth 67*, 607.
Glicksman, M., Shaefer, R.J., Ayers, J.D. (1976), *Metall. Trans. A 7*, 1747.
Glicksman, M.E., Singh, N.B. (1986), in: *Rapidly Solidified Powder Alloys*: Fine, M.E., Stark, E.A. (Eds.). Philadelphia: ASTM, p. 44.
Glicksman, M.E., Singh, N.B. (1989), *J. Cryst. Growth 98*, 277.
Glicksman, M.E., Singh, N.B., Chopra, M. (1988), *J. Cryst. Growth 92*, 543.
Gremaud, M., Carrard, M., Kurz, W. (1990), *Acta Metall.* (to be published).
Hogan, L.M., Kraft, R.W., Lemkey, F.D. (1971), "Eutectic Grains", in: *Adv. in Mater. Res. 5*, p. 83.
Honjo, H., Ohta, S., Sawada, Y. (1985), *Phys. Rev. Lett. 55*, 841.
Huang, S.C., Glicksman, M.E. (1981), *Acta Metall. 29*, 701; 717.
Hunt, J.D. (1979), in: *Solidification and Casting of Metals*. London: TMS, p. 1.
Hunt, J.D. (1987), private communication.
Hunt, J.D., Jackson, K.A. (1966), *Trans. Metall. Soc. AIME 236*, 843.
Hunt, J.D., Jackson, K.A., Brown, H. (1966), *Rev. Sci. Instr. 37*, 805.
Huse, D. (1986), *Phys. Rev. B 34*, 7845.
Ivantsov, G.P. (1947), *Dokl. Akad. Nauk SSSR 58*, 567.
Jackson, K.A. (1958), in: *Liquid Metals and Solidification*. Cleveland: ASM, p. 174.
Jackson, K.A., Hunt, J.D. (1966), *Trans. Metall. Soc. AIME 236*, 1129.
Jones, H., Kurz, W. (1981), *Z. Metallkde 72*, 792.
Kahlweit, M. (1970), *J. Cryst. Growth 6*, 125.
Karma, A. (1986), *Phys. Rev. Lett. 57*, 858.
Karma, A. (1987), *Phys. Rev. Lett. 59*, 71.
Karma, A., Langer, J.S. (1984), *Phys. Rev. A 30*, 3147.
Karma, A., Kotliar, B.G. (1985), *Phys. Rev. A 31*, 3266.
Karma, A., Pelce, P. (1989a), *Phys. Rev. A 39*, 4162.
Karma, A., Pelce, P. (1989b), *Europhys. Lett. 9*, 713.
Kashuba, A., Pokrovsky, V. (1990), *Z. Physik 78*, 289.
Kassner, K., Misbah, C. (1990a), *Phys. Rev. Lett.* in press.
Kassner, K., Misbah, C. (1990b), to be published.
Kawasaki, K. (1990), in: *Proceedings of STATPHYS, Rio de Janeiro 1989*, in press.
Kessler, D., Levine, H. (1986a), *Phys. Rev. Lett. 57*, 3069.
Kessler, D., Levine, H. (1986b), *Phys. Rev. A 33*, 3352.
Kessler, D., Levine, H. (1986c), *Phys. Rev. A 33*, 3625.
Kessler, D., Levine, H. (1986d), *Phys. Rev. A 36*, 4123.
Kessler, D., Levine, H. (1989), *Phys. Rev. A 39*, 3041.
Kessler, D., Levine, H. (1990), to be published.
Kessler, D., Koplik, J., Levine, H. (1987), in: *Pattern, Defects and Microstructures in Nonequilibrium Systems*: Walgraef, D. (Ed.). Dordrecht: Martinus Nijhoff.
Kessler, D., Koplik, J., Levine, H. (1988), *Adv. Phys. 37*, 255.
Kofler, A. (1950), *Z. Metallkde 41*, 221.
Kramer, L., Ben Jacob, E., Brand, H., Cross, M. (1982), *Phys. Rev. Lett. 49*, 1891.
Krug, J., Spohn, H. (1990), in: *Solids Far from Equilibrium: Growth, Morphology and Defects*: Godreche, C. (Ed.), in press.
Kruskal, M., Segur, H. (1985), *Asymptotics Beyond All Orders in a Model of Dendritic Crystals*, A.R.A.P. Tech. Memo, pp. 85-25.
Kurowsky, P. (1990), Thesis, GPS-Univ. Paris VII.
Kurz, W., Fisher, D.J. (1981), *Acta Metall. 29*, 11.
Kurz, W., Fisher, D.J. (1984, 1989), *Fundamentals of Solidification*. Aedermannsdorf, CH: Trans. Tech. Publ.
Kurz, W., Giovanola, B., Trivedi, R. (1986), *Acta Metall. 34*, 823.
Kurz, W., Giovanola, B., Trivedi, R. (1988), *J. Cryst. Growth 91*, 123.
Kurz, W., Sahm, P.R. (1975), *Gerichtet erstarrte eutektische Werkstoffe*. Berlin: Springer Verlag.

Kurz, W., Trivedi, R. (1990), *Acta Metall. Mater. 38*, 1.
Kurz, W., Trivedi, R. (1991), to be published.
Landau, L.D., Lifshitz, E.M. (1970), *Statistische Physik*. Berlin: Akademie-Verlag.
Langer, J.S. (1971), *Annals of Physics 65*, 53.
Langer, J.S. (1980a), *Rev. Mod. Phys. 52*, 1.
Langer, J.S. (1980b), *Phys. Rev. Lett. 44*, 1023.
Langer, J.S. (1980c), *Physico-Chem. Hydrodyn. 1*, 41.
Langer, J.S. (1987a), *Phys. Rev. A 36*, 3350.
Langer, J.S. (1987b), in: *Le hasard et la matiere / Chance and matter*: Soulette, J., Vannimenus, J., Stora, R. (Eds.). Amsterdam: Elsevier Science Publ.
Langer, J.S., Müller-Krumbhaar, H. (1977), *J. Cryst. Growth 42*, 11.
Langer, J.S., Müller-Krumbhaar, H. (1978), *Acta Metall. 26*, 1681, 1689, 1697.
Langer, J.S., Müller-Krumbhaar, H. (1980), *Acta Metall. 29*, 145.
Langer, J.S., Müller-Krumbhaar, H. (1982), *Phys. Rev. A 27*, 499.
Langer, J.S., Turski, L.A. (1977), *Acta Metall. 25*, 1113.
Lesoult, G. (1990), private communication.
Lesoult, G. (1980), *Ann. Chim. Fr. 5*, 154.
Levine, H., Rappel, W. (1990), preprint.
Lifshitz, I.M., Slyozov, V.V. (1961), *J. Phys. Chem. Solids 19*, 35.
Lipton, J., Glicksman, M.E., Kurz, W. (1987), *Metall. Trans. 18 A*, 341.
Livingston, J.D., Cline, H.E., Koch, E.F., Russel, R.R. (1970), *Acta Metall. 18*, 399.
Mashaal, M., Ben Amar, M., Hakim, V. (1990), *Phys. Rev. A 41*, 4421.
Maurer, J., Bouissou, P., Perrin, B., Tabeling, P. (1988), *Europhys. Lett. 8*, 67.
Mc Fadden, G.B., Coriell, S.R. (1984), *Physica 12 D*, 253.
Meakin, P. (1988), in: *Phase Transitions and Critical Phenomena*, Vol. 12: Domb, C., Lebowitz, J. (Eds.). London: Academic.
Meiron, D.I. (1986), *Phys. Rev. A 33*, 2704.
Misbah, C. (1987), *J. Phys. France 48*, 1265.
Misbah, C. (1989), *J. Phys. France 50*, 971.
Misbah, C., Müller-Krumbhaar, H., Saito, Y. (1990a), *J. Crystal Growth 99*, 156.
Misbah, C., Müller-Krumbhaar, H., Temkin, D.E. (1990b), to be published.
Mullins, W., Sekerka, R. (1963), *J. Appl. Phys. 34*, 323.
Mullins, W., Sekerka, R. (1964), *J. Appl. Phys. 35*, 444.
Nakaya, U. (1954), *Snow Crystals*. Cambridge: Harvard Univ. Press.
Nash, G.E., Glicksman, M. (1974), *Acta Metall. 22*, 1283.
Nelson, D. (1983), in: *Phase Transitions and Critical Phenomena*: Domb, C., Lebowitz, J. (Eds.). New York: Academic Publ.
Newell, A.C., Whitehead, J.A. (1969), *J. Fluid Mech. 38*, 279.
Ohno, K., Trinkaus, H., Muller-Krumbhaar, H. (1990), *J. Crystal Growth 99*, 68.
Papapetrou, A.Z. (1935), *Kristallograph. 92*, 89.
Pelce, P., Clavin, P. (1987), *Europhys. Lett. 3*, 907.
Pelce, P., Pomeau, Y. (1986), *Studies Appl. Math. 74*, 1283.
Pelce, P., Pumir, A. (1985), *J. Crystal Growth 73*, 357.
Perepezko, J.H., Mueller, B.A., Ohsaka, K. (1987), in: *Undercooled Alloy Phases*: Collings, E.W., Koch, C.C. (Eds.). Warrandale: TMS, p. 289.
Quested, P.N., McLean, M. (1984), *Mater. Science Eng. 65*, 171.
Rabaud, M., Couder, Y., Gerard, N. (1988), *Phys. Rev. A 37*, 935.
Raz, E., Lipson, S.G., Polturak, E. (1989), *Phys. Rev. A 40*, 1088.
Raz, E., Lipson, S.G., Ben Jacob, E. (1990), to be published.
Rieke, H., Paap, H.G. (1986), *Phys. Rev. A 33*, 547.
Riquet, J.P., Durant, F. (1975), *Mat. Res. Bull. 10*, 399.
Saffmann, P.G., Taylor, G.I. (1958), *Proc. R. Soc. London Ser. A 254*, p. 312.
Saito, Y., Goldbeck-Wood, G., Müller-Krumbhaar, H. (1987), *Phys. Rev. Lett. 58*, 1541.
Saito, Y., Goldbeck-Wood, G., Müller-Krumbhaar, H. (1988), *Phys. Rev. Lett. A 38*, 2148.
Saito, Y., Misbah, C., Müller-Krumbhaar, H. (1989), *Phys. Rev. Lett. 63*, 2577.
Seetharaman, V., Trivedi, R. (1988), *Metall. Trans. 19 A*, 2955.
Seetharaman, V., Eshelman, M., Trivedi, R. (1988), *Acta Metall. 36*, 1175.
Singh, N.B., Glicksman, M.E. (1989), *J. Cryst. Growth 98*, 534.
Somboonsuk, K., Mason, J.T., Trivedi, R. (1984), *Metall. Trans. A 15*, 967.
Somboonsuk, K., Trivedi, R. (1985), *Acta Metall. 33*, 1051.
Straun, J. (1989) (preprint).
Temkin, D.E. (1985), *Kristallografia 30*, 1055.
Temkin, D.E. (1990) (in published).
Tirmizi, S.H., Gill, W.N. (1989), *J. Cryst. Growth 96*, 277.
Trivedi, R. (1980), *J. Crystal Growth 49*, 219.
Trivedi, R. (1984), *Metall. Trans. 15 A*, 977.
Trivedi, R., Kurz, W. (1986), *Acta Metall. 34*, 1663.
Trivedi, R., Lipton, J., Kurz, W. (1987), *Acta Metall. 35*, 965.
Trivedi, R., Laorchan, V. (1988), *Acta Metall. 39*, 1941 and 1951.
Trivedi, R., Mason, J.T., Verhoeven, J.D., Kurz, W. (1990), to be published.
Trivedi, R., Somboonsuk, K. (1984), *Mater. Sci. Eng. 65*, 65.
Trivedi, R., Somboonsuk, K. (1985), *Acta Metall. 33*, 1061.

Ungar, L. H., Brown, R. A. (1984a), *Phys. Rev. B 29*, 1367.
Ungar, L. H., Brown, R. A. (1984b), *Phys. Rev. B 30*, 3993.
Ungar, L. H., Brown, R. A. (1985a), *Phys. Rev. B 31*, 5923.
Ungar, L. H., Brown, R. A. (1985b), *Phys. Rev. B 31*, 5931.
Uwaba, M., Saito, Y. (1990), *J. Crystal Growth 99*, 175.
Voronkov, V. V. (1983), in: *Modern Theory of Crystal Growth*. Chernov, A. A., Müller-Krumbhaar, H. (Eds.). Heidelberg: Springer Verlag.
Wagner, C. (1961), *Z. Elektrochem. 65*, 581.
Warren, J. A., Langer, J. S. (1990), to be published.
Willnecker, R., Herlach, D. M., Feuerbacher, B. (1989), *Phys. Rev. Lett. 62*, 2707.
Wollkind, D., Segel, L. (1970), *Philos. Trans. R. Soc. London 268*, 351.
Wu, Y., Piccone, T. J., Shiohara, Y., Flemings, M. C. (1987), *Metall. Trans. 18*, 915, 925.
Wulff, G. (1901), *Z. Kristallogr. Mineral. 34*, 449.
Xiao, R. F., Alexander, J. I. D., Rosenberger, F. (1988), *Phys. Rev. A 38*, 2447.
Yokoyama, E., Kuroda, T. (1988), in: *Dynamics of Ordering Processes in Condensed Matter*. Komura, S., Furukawa, H. (Eds.). New York: Plenum Publ.
Zettlemoyer, A. (Ed.) (1969), *Nucleation I*. New York: Dekker.
Zettlemoyer, A. (Ed.) (1976), *Nucleation II*. New York: Dekker.
Zimmermann, M., Carrard, M., Kurz, W. (1989), *Acta Metall. 37*, 3305.
Zimmermann, M., Karma, A., Carrard, M. (1990), *Phys. Rev. B 42*, 833.